PRE-INITIATION FEATURES INVESTIGATION AND HELICAL STRUCTURE FORMATION IN SOLID METAL LINER Z-PINCHES

A Dissertation

Presented to the Faculty of the Graduate School

of Cornell University

in Partial Fulfillment of the Requirements for the Degree of

Doctor of Philosophy

by

Levon Atoyan

May 2018

PRE-INITIATION FEATURES INVESTIGATION AND HELICAL STRUCTURE FORMATION IN SOLID METAL LINER Z-PINCHES

Levon Atoyan, Ph.D.

Cornell University 2018

The work in this dissertation has focused on two phenomena that occur in a solid metal liner Z-pinch. The first involves features that develop before the liner's surface ionizes and turns into plasma. The second concerns the formation of a helical structure in the liner when an external axial magnetic field is applied throughout the liner.

We experimentally investigated micrometer scale features that develop in thin metallic liners driven by the 1 MA COBRA pulsed power machine. These features are associated in the literature with possible non-ionized matter electrothermal and electrochoric instabilities [Phys. Plasmas **22**, 102701 (2015)]. To study the development of the micrometer structure, we first needed to optimize the X-pinch X-ray diagnostic for such high-resolution measurements in cylindrical liner experiments. We show images from two types of detectors, the SR image plate and the DR-50 film, demonstrating that using film is critical for the detection of the micrometer structure in thin Ti, Ni and Cu liners.

Using that X-pinch diagnostic, we first examined the 17 - 25 μm features that develop in 16 μm thick Al liners without dielectric coatings. Results of areal density variation and the dominant wavelength of these features are compared with computer simulations using an extended MHD computational model with recently implemented Al Equation-of-State and resistivity models. Experimental results obtained with Al, Ni, Cu and Ti show the average feature size of the

perturbation decreases in these materials in the order given. When applying a dielectric coating at the surface of the material, we demonstrate that expansion inhibition correlates with significantly reduced areal density variation and size of perturbations. We additionally show evidence that the insulator is predominantly heated by conduction, as opposed to radiation. Finally, we show that ingrained structure in our liner material a) influences the small scale features' structure, changing the azimuthal correlation of the features from highly to weakly correlated depending on the orientation of current flow with respect to the material's ingrained pattern and b) changes the density perturbation amplitude quantitatively.

Beyond micrometer scale features, we also investigated the formation of a 600-750 μm wavelength helical pattern in the liner when viewed with extreme ultraviolet self-emission imaging on COBRA. The magnetic field in these experiments was created using either twisted return current wires positioned close to the liner, generating a time-varying B_z, or a Helmholtz coil, generating a steady-state B_z. We show that an upward external axial magnetic field generates a left-handed twist of the helical pattern and a downward field a right-handed twist. We further show that the helix angle does not correspond to $\frac{B_{z_{applied}}}{B_\theta(t)}$, where $B_\theta(t)$ is the expected B_θ at the time of measurement, and briefly present a few proposed explanations for the behavior. We conclude that section by proposing an evidence-based explanation as to why the self-emission diagnostics detect any pattern at all, whether helical or axial.

BIOGRAPHICAL SKETCH

Levon Atoyan was born on October 1st, 1988, in Yerevan, Armenia. His family moved between Armenia and Germany during his childhood before settling in Montreal, Canada in 2000. Starting at an early age, he was fascinated by anything man-made that could fly, whether in the atmosphere or space. Over time, that developed into a strong interest in advanced technologies behind energy and propulsion systems. This interest led him to pursue a bachelors in mechanical engineering. To understand some of the advanced technologies he was more interested in, such as technically advanced plasma thrusters and fusion energy schemes, he then decided to continue his education studying plasma physics in graduate school. So, in 2012, he joined the Lab of Plasma Studies to do just that.

Leaving the lab, his initial focus will be the commercialization of energy technologies, so that they're not just sitting idly by on a shelf or in someone's computer hard drive. Beyond his so-called career, some accurate ways to describe Levon would be an avid skiier, a terribly balanced surfer, a devil's advocate, a (badly funded) whiskey enthusiast and a semi-retired artist.

To my parents, Hasmik and Armen Atoyan,
for constantly helping me pursue my passions.

ACKNOWLEDGMENTS

First and foremost, I would like to thank my adviser, Prof. David Hammer, for giving me freedom to explore topics that interested me, all the while providing advice and guidance whenever I needed it, turning me into a better scientist in the process. Of smaller but significant importance, many thanks for patiently teaching me the art of clear written communication.

I would like to thank Dr. Tania Shelkovenko and Dr. Sergei Pikuz, who were critical in my understanding of the tricky X-pinch (and key in my Russian speaking ability). I would also like to thank them, as well as Dr. John Greenly, for helping me significantly improve my knowledge of experimental techniques and my experimental skills in general.

I would like to thank Prof. Richard Lovelace, Prof. Bruce Kusse, and Prof. Charles Seyler for their overall support, whether it be through teaching me relevant subject matter, suggesting improvements to a given experiment, or providing simulation support whenever I asked for it.

Many thanks to Harry Wilhelm, Todd Blanchard, Dan Hawkes and Dr. Billy Potter for making any and all hardware issues, COBRA issues, or even coffee issues disappear. Thanks to you, I was able to use my COBRA runs as efficiently as COBRA would allow, and learn many interesting, random, invaluable golden nuggets in the process.

From the students and postdocs that I had the pleasure to work with, I would like to say special thanks to Dr. Kate Bell, for showing me the ropes when I had close to zero background knowledge in the field of the lab. To my lab mates in general, you had to deal with an impatient, argumentative and regrettably "social" person throughout the years. Maybe you did not deserve that (except for Joey Engelbrecht, infamously slandering his "friends" behind their backs), but

thank you for humoring me. It turned my years at Cornell into fond memories.

I would also like to thank Cindy VanOstrand for making any and all administrative chores disappear as well as helping keep the lab a social unit, something too often neglected. Thanks as well to Nikki VanOstrand, who, without ever asking for anything in return, constantly provided the lab with the key components to healthy mental functioning: chocolate + sugar (cakes).

Last but not least, I would like to acknowledge the funding sources and agencies that allowed me to keep my worries and focus on my research. The work in this dissertation was supported by the National Nuclear Security Administration Stewardship Sciences Academic Programs under Department of Energy Cooperative Agreement DE-NA0001836 as well as by the Department of Energy grant numbers DE-NA0001847 and DE-NA0002952.

TABLE OF CONTENTS

LIST OF TABLES

LIST OF FIGURES

CHAPTER 1

INTRODUCTION

1.1 Z-pinch

Z-pinches have been studied in the plasma physics community since the mid nineteen hundreds [7, 8, 9]. The basic idea, as implemented in the 21^{st} century, is to take a cylindrical load, whether it be by appropriately configured wires, a cylindrical foil, a cylindrical gas puff, etc., and pass a high current through it. Doing so will generate a plasma column within which current flows, thereby generating a magnetic field around the plasma column. The resulting $\mathbf{J} \times \mathbf{B}$ force is radially inward, where $\mathbf{J}$ is the axial current density and $\mathbf{B}$ is the azimuthal magnetic field that is calculated from the current density using Ampere's law. This inward force implodes the plasma column to a radius that is limited by instabilities and heats it. In practical situations of interest here, the current is produced by a pulsed power machine [10, 11, 12, 13]. As both the peak current and the pulse duration are limited, the mass per unit length and radius of the plasma column that can be imploded are also limited. This will be discussed in Chapter 3.

Any introduction to Z-pinches, however brief, should also include a reference to the Z pulsed power machine [14] in Sandia National Laboratories. This machine delivers a 27 MA current pulse with a 100 ns rise time to a low inductance load. Its pre-pulse alone reaches a current magnitude that most laboratory pulsed power machines can achieve only at peak current, including the machines at the Lab of Plasma Studies (LPS) discussed in Chapter 2. Since electric power scales as I^2, any work that is done at universities to help better under-

stand experiments on Z needs to take the difference in power delivered into account.

1.2 Magnetized Liner Inertial Fusion

A relatively new Z-pinch fusion concept called Magnetized Liner Inertial Fusion (MagLIF) [1, 15, 16] being investigated at Sandia National Laboratories has provided much of the motivation for the work presented in this thesis. It has also motivated a lot of work on Z-pinches of solid metal cylinders in general, both in the US and abroad.[17, 18, 19, 20, 21] MagLIF broadly falls under the Magneto-Inertial Fusion (MIF), alternatively called Magnetized Target Fusion (MTF), category, which is essentially a hybrid between purely magnetically confined fusion (MCF), such as Tokamak fusion, and purely inertially confined fusion (ICF), such as laser fusion as it is being pursued at the National Ignition Facility.[22] An advantage of MIF over ICF is that it does not require as high an implosion velocity because the magnetic field is designed to thermally insulate the hot plasma from cold boundaries. An advantage of MIF over MCF is that it does not require as long a confinement time to achieve net energy output due to operating at higher densities.

The MagLIF concept can be broadly divided into three stages: magnetization, fuel preheat and compression. Please refer to Fig. 1.1 for visualization.[2] In the following discussion and the remainder of this thesis, a cylindrical metal annulus will be referred to as a liner, including the liner used in MagLIF.

MagLIF begins with a solid metal liner, Be being the best option for the metal, with a wall thickness of a few hundred μm and a radius of a few mm. The

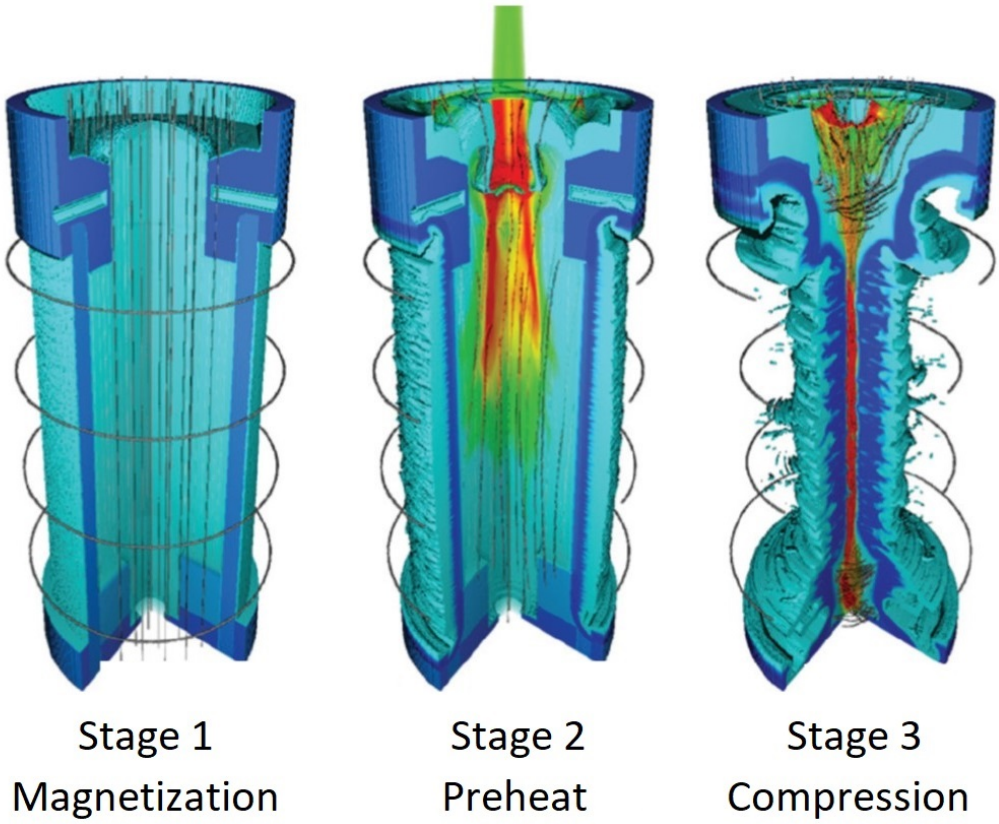

Figure 1.1: The three stages of MagLIF: fuel magnetization, preheat, and compression. [1, 2]

liner's aspect ratio is defined as $(r/\delta)_{liner}$, where r is the radius of the liner and δ is the wall thickness. A value that is too large will cause the Magneto-Rayleigh Taylor (MRT) instability to feed through to the inner surface of the liner during implosion, destabilizing the implosion that follows.[23, 24, 25, 26, 27] A value that is too small will cause the liner to be too heavy to implode or its radius to be too small for significant compression of the plasma and embedded magnetic field within the liner.[1, 22, 2] Aspect ratios being tested on Z for MagLIF so far are typically around 6.[28] In MagLIF experiments, the liner is filled with either deuterium (DD) gas or a mixture of deuterium-tritium (DT) gas.

The sequence of events in a MagLIF experiment on Z is as follows. We first

apply an axial magnetic field with a long enough rise time to diffuse uniformly into the liner. The critical function of this magnetic field is to reduce thermal losses between the fusion fuel, i.e., hot plasma produced by eventual compression of the imploding liner, and the relatively cold liner wall. During the last 5-6 years, experiments on Z have used a Helmholtz coil to generate this field. However, some of the disadvantages of this, such as inefficient magnetic energy coupling at the load, increased load inductance due to a longer feed section, and very limited diagnostic access for $B_z \geq 10T$, have pushed some alternative ideas to be considered more seriously.[29, 30] The inefficient energy coupling is due to the Helmholtz coil generating a magnetic field in a much larger volume than the liner. Quantitatively, a peak magnetic energy delivery of hundreds of kJ from the coil will result in the delivery of only about 100 J of magnetic energy within the liner, where it is needed. In the future, the axial field generation mechanism might involve some form of twisted conductor configuration or, alternatively, coils that produce axially non-uniform magnetic fields near the load. This is currently an active area of investigation at Sandia.

Once magnetized, the fuel inside the liner is preheated via a laser pulse that is directed into the fuel axially. There have been many issues associated with non-ideal spatial heating of the fuel, inefficient laser-plasma energy coupling, and material from the liner's axial "plug" mixing with the fuel. By plug, we are referring to the thin film at the axial end of the liner through which the laser comes in (see stage 2 in Fig. 1.1). This is also an active area of research and development for MagLIF.[31, 32]

The third stage consists of imploding the liner. This compresses and heats the fuel inside, ideally enabling fusion reactions to occur. The current pulse that

drives the Z-pinch compression starts before the preheating laser pulse. That is because the liner starts moving radially inward, that is, imploding, at about $60 - 70\%$ into the rising current pulse. The laser is fired within a few ns of the beginning of implosion. Once the liner starts accelerating inward, it stagnates within the next 60 ns. Experimentally, the initial neutron yields using DD fuel were $5 \times 10^{11} - 2 \times 10^{12}$, which is under the predicted yield of 6×10^{13} from simulations.[15] The main hypotheses for the discrepancy are poor laser energy coupling into the fuel, the presence of liner-fuel mixing, and other possible 3D effects. All of these issues are currently actively under investigation.

Micrometer scale density and temperature structure was shown to develop in the $\approx$ 0.01 - 1 g/cm^{-3} density region in simulations and experiments published by Peterson *et al.*[33, 34] This $\sim$ 10-20 μm structure was attributed to an "electrothermal instability", explained in detail in Chapter 3, and was proposed to act as a seed for the subsequent MRT instability in MagLIF. Moreover, the MRT instability, which leads to larger near-millimeter scale density structure, [35] was shown to develop helically, as opposed to horizontally, when an axial external magnetic field was applied.[36]

For this dissertation, we have investigated both the micrometer scale structure and the larger helical structure, why they form and what affects them. The goal is to be able to mitigate their formation, assuming that is desirable, if possible. In Chapter 2, we briefly discuss the machines and diagnostics used in our experiments. Chapter 3 presents the theory relevant to understanding the analysis of our experimental results. Chapter 4 describes how the X-pinch diagnostic was adjusted to perform micrometer scale density measurements in the high-density region of the liner. The results from that diagnostic are then

presented and analyzed in Chapter 5. The helical structure is investigated in Chapter 6 and concluding remarks are given in Chapter 7.

CHAPTER 2

MACHINES AND DIAGNOSTICS

2.1 Pulsed Power Machines

One method to deliver very high power to an experimental load is via electrical pulse compression. We charge up a system of capacitors for a prolonged period of time, making sure these capacitors are disconnected from the load. Once we charge to a desired energy level, we then deliver this energy in a very short time, typically in the $ns - \mu s$ range, via a series of additional capacitors and switches. This allows using a relatively small amount of energy for very high power delivery. For example, 100 kJ of stored energy delivered in 100 ns constitutes a 1 TW electrical pulse.

The COrnell Beam Research Accelerator (COBRA), shown in Fig. 2.1, is a 1-1.2 MA 100-250 ns rise-time pulsed power machine. It is divided into two symmetric sections that combine their pulses just before the load. In each section, there is a Marx generator that is designed to store 53 kJ and is charged in about 1 minute. A Marx generator [10] is a configuration of capacitors that are connected with "charging" resistors in parallel and with switches that connect the capacitors in series if closed, as shown in Fig. 2.2.

During the charging phase, the switches remain open and the capacitors are charged in parallel through the charging resistors. During the discharging phase, we electrically break down the insulator between the switches' electrodes, pressurized SF_6 in the case of COBRA, closing these switches. At this point, there are multiple discharge paths for the charged capacitors. How-

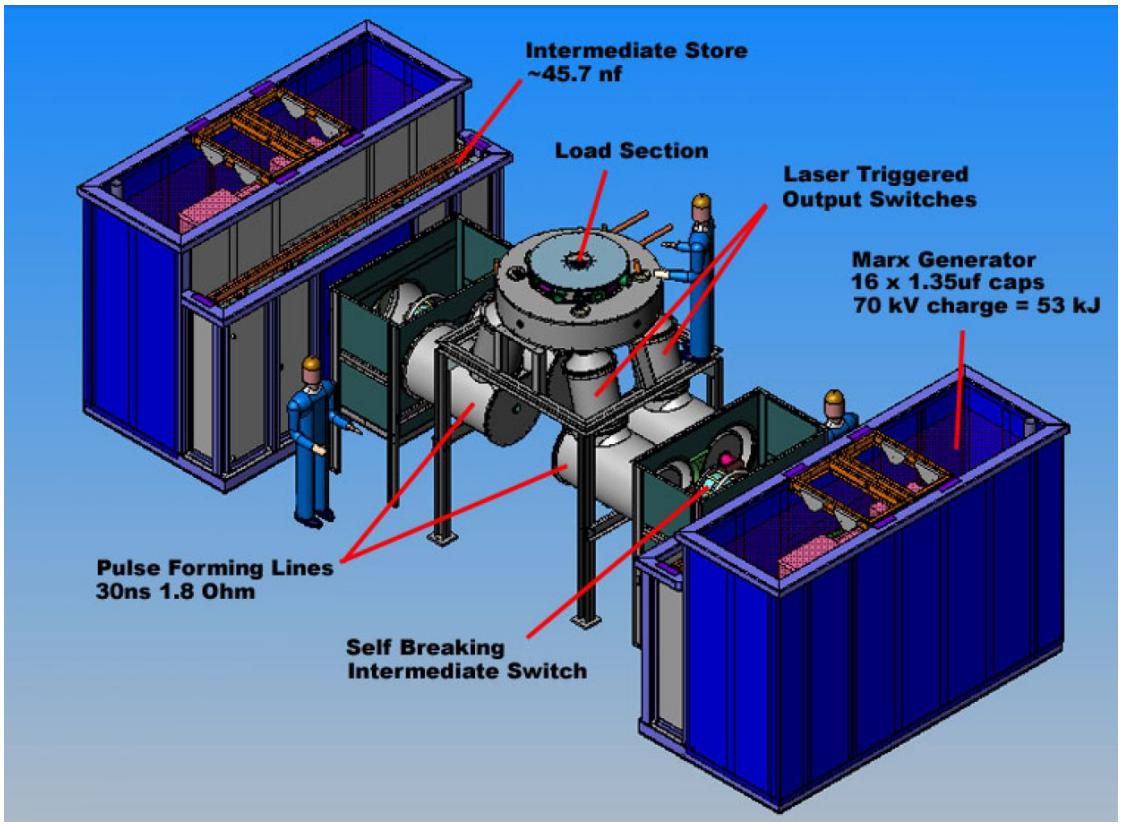

Figure 2.1: A computer-aided design rendering of COBRA with human figures for scale.

ever there is a large difference in resistance between the now-closed low resistance switches and the large resistance charging resistors. That difference will change the corresponding circuits' response time, effectively decoupling those two circuits. Consequently, the capacitors will discharge in a series configuration across the output of the Marx Bank. The electrical breakdown, or closing, of the switches can be induced either by delivering a large voltage pulse to the insulator, called "triggering," or by applying a larger voltage across the electrodes than the insulator can hold off, called "self-break".

On COBRA, each half of the machine has a small Marx bank, called a "trigger-Marx", whose output is connected to the gas switches in the main Marx. Both trigger and main Marxes are charged. Then the trigger-Marx is

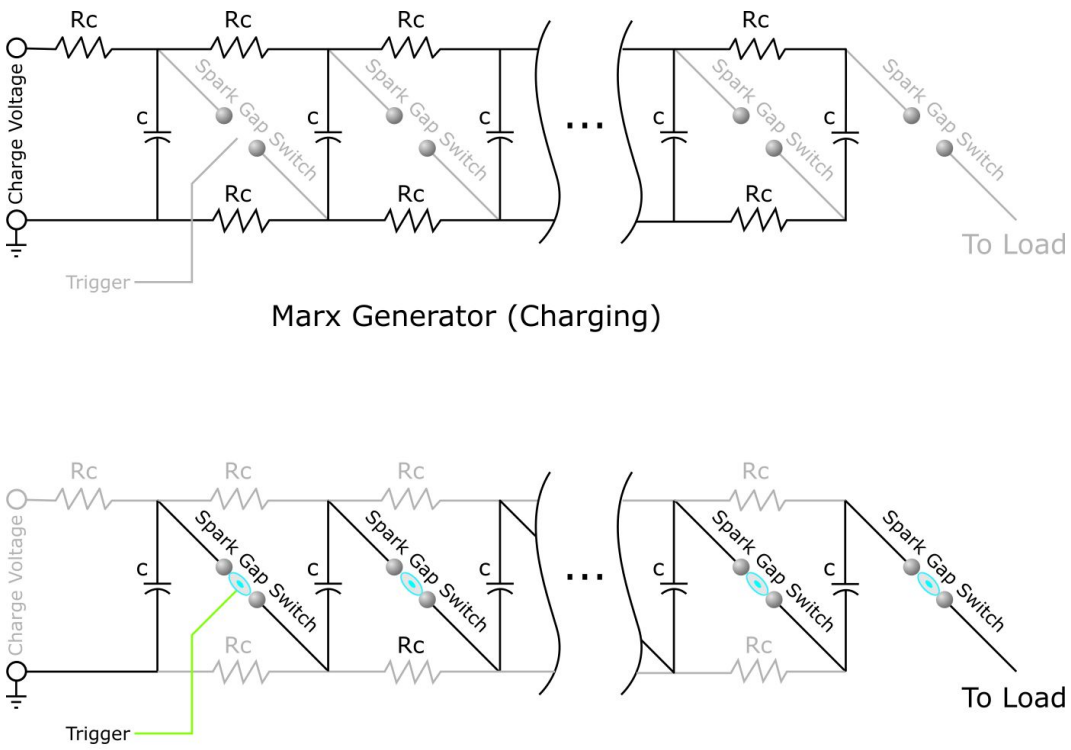

Figure 2.2: A circuit diagram of a Marx bank.

triggered via a 50 kV PT-55 pulser. The resulting voltage pulse output from the trigger-Marx leads to the triggering of the main Marx (hence the name "trigger-Marx"). The main Marx is now switched into a series configuration and a large parallel plate capacitor at its output, called Intermediate Storage Capacitor (ISC), is charged by it in less than 1 μs. This capacitor is connected to the "intermediate" gas switch, which self-breaks. When that happens, the pulse begins to charge two 0.6 m diameter and 1.1 m long cylindrical pulse forming lines (PFLs) designed to compress the pulse temporally. At the opposite end of each PFL, a final gas switch self-breaks, enabling the pulses from the two halves of COBRA, i.e., the four PFLs, to combine and travel through vacuum over a radial magnetically self-insulated transmission line toward the load. The self-generated magnetic fields from the incoming pulses quickly grow large enough to ensure

electrons don't cross the gap between the conductors. Otherwise, these electrons would create a current path across the vacuum gap, shunting the current away from the load.

In summary, COBRA compresses the Marx generator pulse to a 100-250 ns pulse delivered to a small load region in a vacuum chamber.

Switches are clearly key components in a pulsed power machine. These come with electrodes that have various shapes, sizes, and designs. The state of the material inside the switch can also vary. Most are gas switches operating at more than 1 atm pressure, but solid state switches have been becoming more popular. When the more common gas switches are used, such as on COBRA, the Paschen curve is what determines at what voltage the switches break down, given the pressure inside them and the electrode gap distance. Curves for a few gases, including SF_6, which is used in COBRA, are shown in Fig. 2.3.[3]

For self-breaking operation, setting the breakdown voltage to be $\approx 80\ \%$ of the maximum expected voltage on the switch is reasonable. In practice on COBRA, the pressures tend to be adjusted somewhat ad hoc between shots to obtain the desired pulse shape. There is a lot of variation that can occur in the switches shot to shot due to, e.g., debris, electrode surface modifications due to previous breakdowns, or a lab favorite, cosmic rays. Consequently determining switch pressures is far from an exact science.

Overall, we control the time at which the North and South side Marx generators erect relative to each other and deliver each "half-pulse". This determines the pulse profile COBRA will deliver to the load, ranging anywhere from 100 ns and 1.2 MA peak current (short pulse) to 250 ns and 1 MA peak current (long

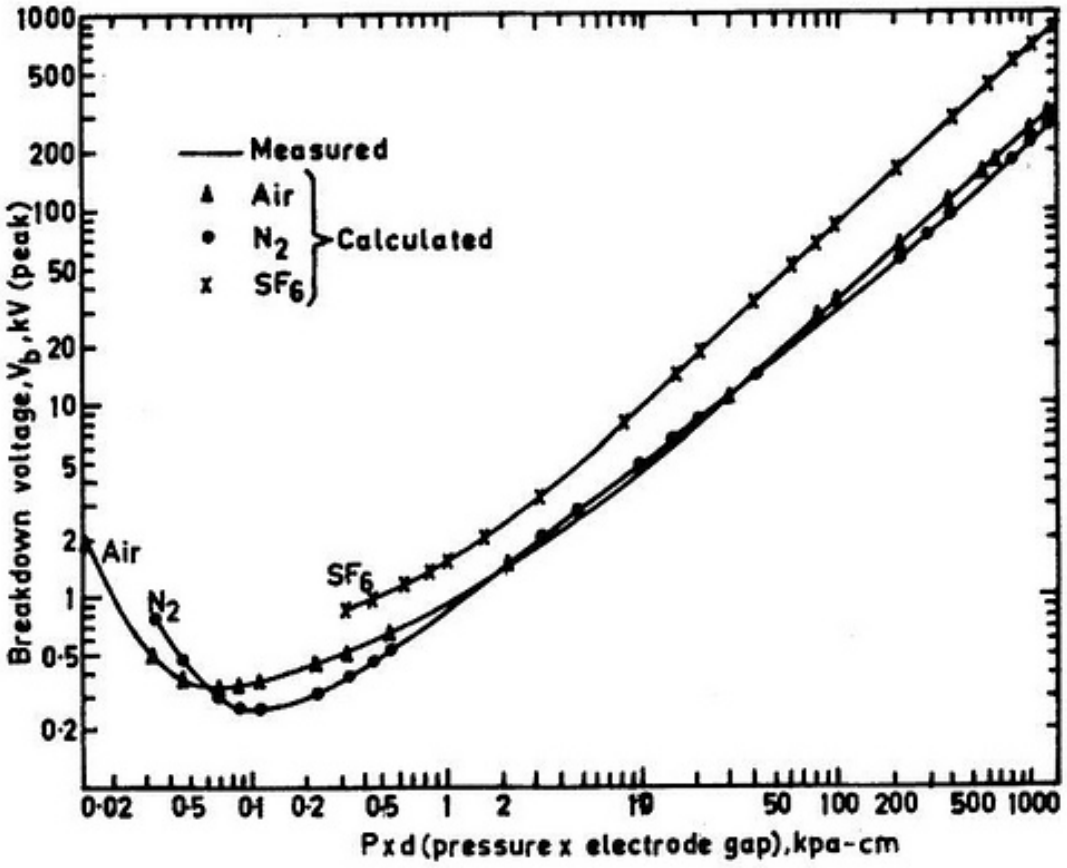

Figure 2.3: Paschen curves for Air, N_2, and SF_6. This work was done by Husain *et al.*[3].

pulse). The work in this dissertation focused on experiments with a short pulse, a typical trace of which is shown in purple in Fig. 2.4.

A smaller machine at LPS, mainly used for diagnostic development and studies of X-pinches at present, is XP. It is a 400 - 500 kA, 50-150 ns rise-time pulsed power machine. A typical current pulse is shown in Fig. 2.5. One of the main differences from COBRA is that it has one Marx generator, one ISC, and one PFL to deliver the pulse. For a detailed description of XP, please refer to Appendix A in "An Investigation Of The Aluminum K-Edge By Spatially Resolved X-Ray Absorption Spectroscopy".[4] Most of the research described

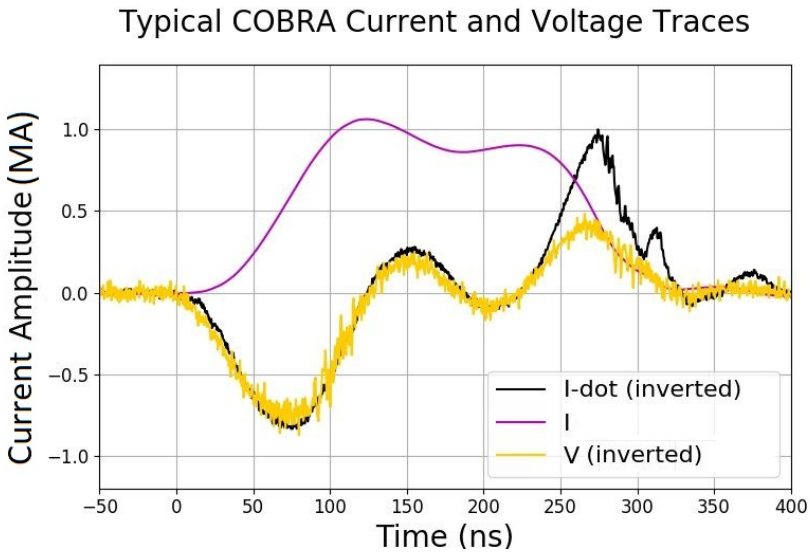

Figure 2.4: Typical current and voltage traces for a COBRA short pulse. The voltage trace follows along with $\frac{dI}{dt}$. The vertical scale is that of the current. The voltage signal shown was not calibrated.

in this Thesis was done on COBRA. XP was used only for some of the X-pinch radiography measurements discussed in Chapter 5.

2.2 Diagnostics

2.2.1 Current Monitor

The current on COBRA is measured via a Rogowski coil [37]. The coil, a schematic of which is shown in Fig. 2.6, is a wire conductor that is helically wrapped and then double-backs through the center of the coil so that the two terminals of the wire end up on the same end of the coil, as shown in Fig. 2.6. This initially straight coil is bent into a circle and positioned around the load. To do this on COBRA, the coil is placed in a circular groove that was cut into the

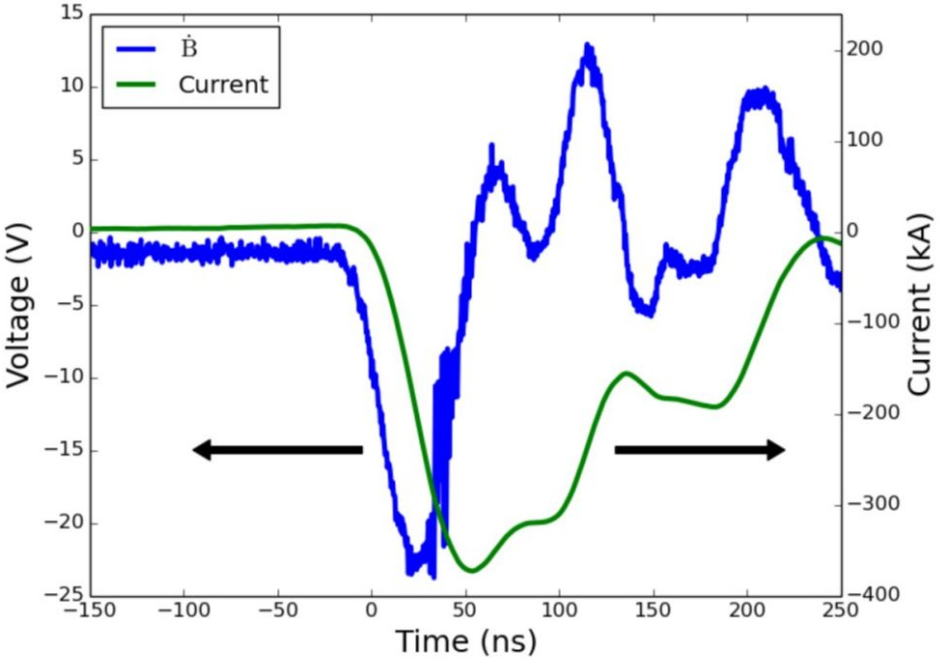

Figure 2.5: Typical current pulse on XP. The blue trace is the signal from a $\dot{B}$ probe (see section 2.2.6) that is measuring the time-derivative of the magnetic field generated by the XP current near the load. The green trace is the load current found by time-integrating and calibrating the signal from the $\dot{B}$ probe trace. Figure is taken from Cahill (2016).[4]

metal surrounding the load. The voltage between the two wire ends is given by:

$$V(t) = -\frac{AN\mu}{2\pi r}\frac{dI}{dt} \tag{2.1}$$

where A is the area of one of the small loops, N is number of turns, μ is the magnetic permeability, r is the radius of the coil, and $\frac{dI}{dt}$ is the rate of change of current with respect to time.

All signals, whether from current monitors, voltage monitors, magnetic probes, etc., were routed to a screen room via double shielded coaxial cables.

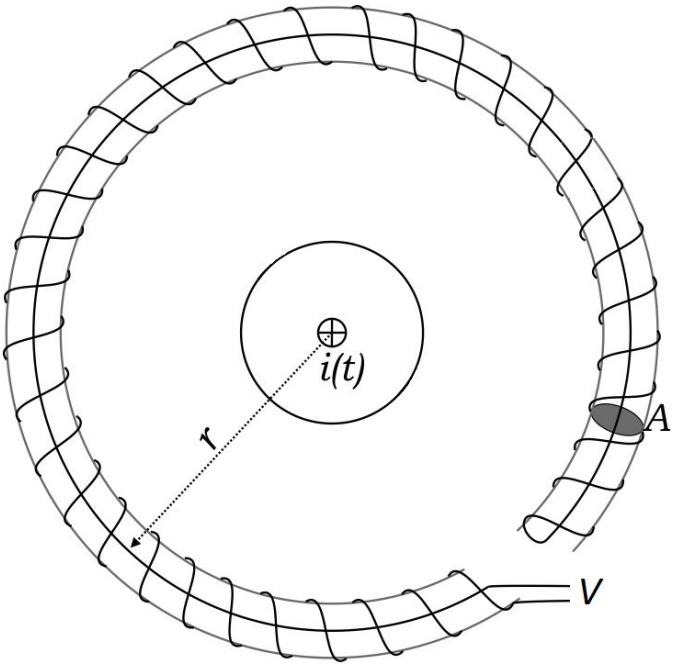

Figure 2.6: Schematic of a Rogowski coil.

2.2.2 Voltage Monitor

On COBRA, the voltage at the load is measured via a long copper wire that connects the center of the power feed to ground. This transmission line is in parallel with the line connecting the power feed to the load region. Consequently the copper wire shunts current away from the load, albeit a very small fraction of the total current ($\lesssim 1\%$). That small amount is due to the much larger total impedance of the copper wire path compared to the main load's path: the inductive component, which is generally the dominant term determining the impedance of the load on COBRA, is roughly 2 orders of magnitude larger for the copper wire (order of magnitude: $L_{load} \sim 10$ nH; $L_{wire} \sim 1$ μH).

Near the ground end of the copper wire, there is a $\dot{B}$ probe, a diagnostic described in section 2.2.6, which measures the time-varying azimuthal magnetic field generated from the current in the wire. Putting everything together, the

voltage measured by this probe relates to the voltage at the power feed as follows:

$$V_{probe} \propto \frac{dB_{\theta wire}}{dt} = \frac{\mu_0}{2\pi r}\frac{dI_{wire}}{dt} \propto V_{load} \approx \frac{d(L_{load}I_{load})}{dt} \tag{2.2}$$

where r is the radial position of the probe with respect to the copper wire's axis, μ_0 is the magnetic permeability of free space, and L_{load} is the inductance of the load. Typical current and voltage signals on COBRA are shown in Fig. 2.4.

We could determine the theoretical calibration value between V_{probe} and V_{load}. In practice, it is easier to determine the calibration value empirically. We can deliver a COBRA pulse to a load that will not move throughout the pulse, has a known inductance value, and is made using a low resistivity material. With the given design parameters, the RI and the $I\frac{dL}{dt}$ voltage components will be negligible compared to the $L\frac{dI}{dt}$ component and so $V_{load} = L\frac{dI}{dt}$. We can use the $\frac{dI}{dt}$ measured by the Rogowski coil to determine V_{load} and calibrate the measured probe voltage accordingly.

2.2.3 Laser Shadowgraphy

In laser shadowgraphy, we direct a laser beam across the load region of COBRA and then capture an image of the distorted beam on a detector such as a visible light CCD camera. The detector records a "shadow" of the experimental load. There are two reasons for the appearance of the shadow. The first is a simple blocking of the laser light, such as by an opaque solid. For laser frequencies below the plasma frequency, the laser, an electromagnetic wave, will not propagate through the plasma. Hence, the plasma frequency corresponding to the

laser frequency is called the *cutoff frequency*. This result can be obtained from a linearized unmagnetized plasma wave analysis [38, 37]. The plasma cutoff frequency is given by:

$$\omega_p = \sqrt{\frac{n_e e^2}{\epsilon_0 m_e}} \tag{2.3}$$

where ω_p is the plasma frequency, e is the electric charge of an electron, ϵ_0 is the permittivity of free space, and m_e is the mass of an electron. For the 532 nm green laser used on COBRA, the cutoff frequency gives a cutoff electron density n_e of $3.9 \times 10^{21} cm^{-3}$.

The second reason for the appearance of a shadow is refraction of the laser beam as it passes through the plasma. The index of refraction in a non-magnetized plasma can be shown to depend on the plasma density as:

$$n = \frac{c}{v_{ph}} = \sqrt{1 - \frac{\omega_p^2}{\omega^2}} \tag{2.4}$$

where n is the index of refraction and ω is the traveling wave's frequency.

As mentioned, waves traveling at frequencies below the plasma frequency are cut off (n is imaginary). For $\omega > \omega_p$, Eq. 2.4 shows that the index of refraction of a plasma is between 0 and 1. As the index of refraction in a plasma is different from that in vacuum and changes within the plasma depending on the plasma density, there are multiple ways for an incident beam to be refracted. First, plasma geometry can lead to converging or diverging of the rays. For example, if the plasma's cross-section has a circular or oval shape, we have an analogous but opposite situation to a converging optical lens (due to n < 1 for plasma vs n > 1 for glass) .

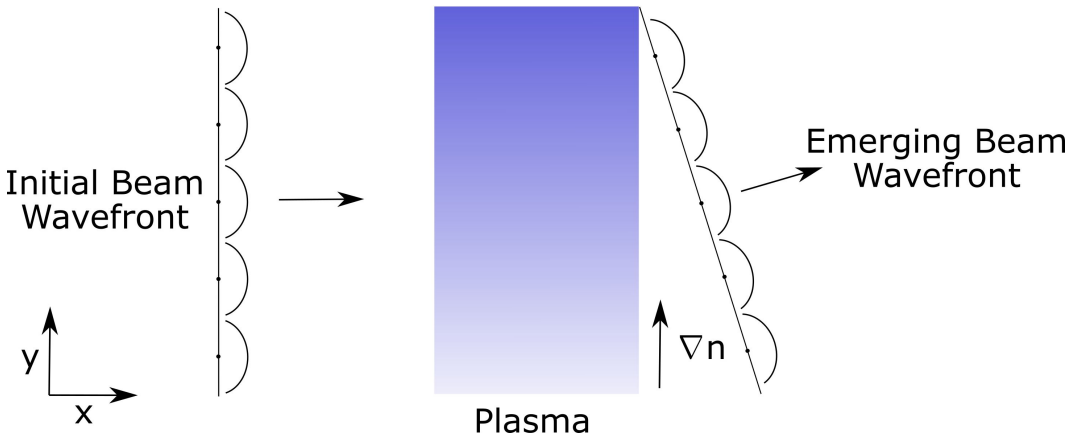

Figure 2.7: Schematic representation of beam refraction due to a uniform plasma density gradient. The wavefronts are shown as a superposition of propagating wavelets to facilitate conceptualization of the effect of a changing wave phase speed along the y axis in the plasma.

Second, even if the incident beam's wavefront is perfectly parallel to the surface of the plasma, the changing index of refraction as a result of a plasma density gradient perpendicular to the beam propagation direction can cause refraction. If a plane wave incident on the plasma has a wavefront parallel to, e.g., the y-plane, and the plasma has a density gradient in that same orientation, the changing phase speed of the beam along the y-direction will cause the wavefront to tilt. In Fig. 2.7, which displays such a scenario schematically, the wavefronts are divided into a superposition of wavelets to highlight that each of these travel through the plasma at a different phase speed, emerging from the plasma at a different time. If the density gradient is constant, the refraction will cause a linear rotation of the wavefront, as shown, and hence shifting of the beam location on the detector. But if there is a second-order density gradient, $\frac{d^2n}{dy^2} \neq 0$, which is a more realistic scenario, the refraction will result in a curved emerging wavefront that will lead to shifting as well as (de)focusing of the beam on the detector.[37] Sample laser shadowgraphs are shown in Fig. 2.8 (b) - (d).

In both laser shadowgraphy and interferometry setups on COBRA, a 150 ps

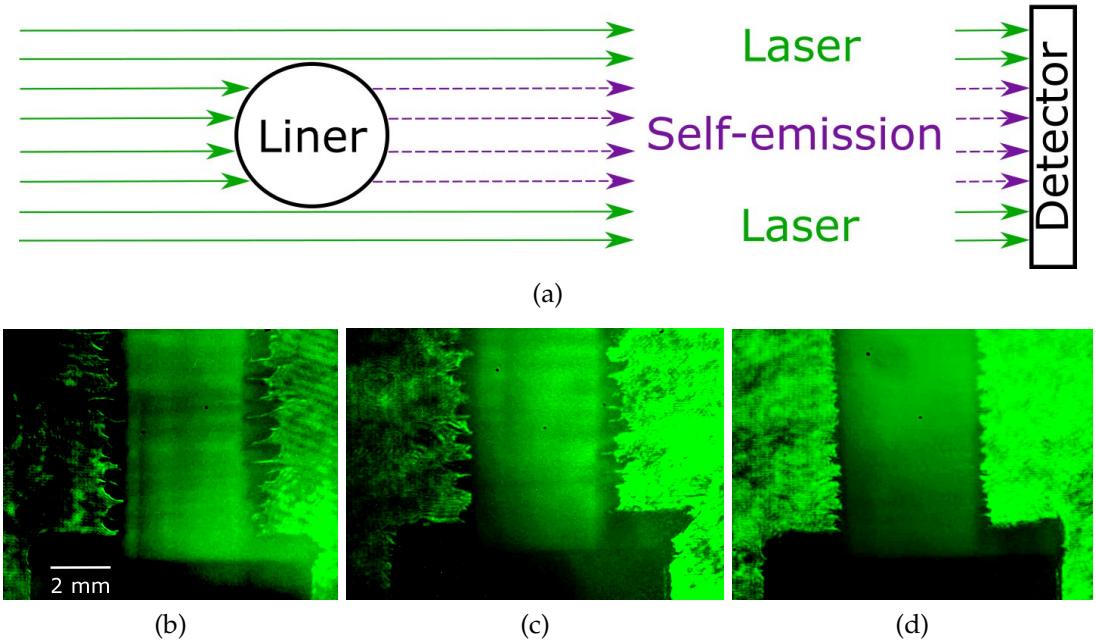

Figure 2.8: (a) Schematic representation from an axial viewpoint of a liner's shadowgraph and self-emission captured on a detector. (b) - (d) Shadowgraphy images simultaneously displaying time-gated shadowgraphs and time-integrated optical self-emission, as described in Sections 2.2.3 and 2.2.5. In each, the cathode, near the bottom of the image, is supporting a 4.2 mm diameter cylindrical metal liner. These images will be discussed in detail in Chapter 6

.

150 mJ laser was used with off-the-shelf digital single-lens reflex (SLR) cameras. The detector's exposure was not time gated in the experiments. Therefore, if the cameras were left with open shutters without any filtering, the optical self-emission light from the plasma would dominate and saturate the camera. To counter this, first a green filter was used to single out the laser's wavelength in the optical spectrum. This was followed by two polarizers. The first polarizer's function was to maximize light in the laser's polarization orientation and cut out the plasma light not in the corresponding polarization. The second polarizer's function was to reduce the laser's and the remaining plasma light's intensity equally by rotating that polarizer's orientation away from maximum transmission. If the light intensity was still too high, neutral density (ND) filters

could be added to the system as well. Two advantages of working with a second polarizer, as opposed to an ND filter, were the speed at which the filtering could be adjusted and the continuous, as opposed to discrete, intensity reduction the polarizer enabled.

2.2.4 Laser Interferometry

Laser interferometry is a diagnostic used to measure electron density. It is very widely used in plasma physics [9, 39] and merits at least a brief overview even though it was not a primary diagnostic in our experiments. The diagnostic requires using two laser beams that are coherent, commonly produced by splitting a beam. One passes through the plasma, the other does not. In our configuration, the "shearing" configuration is used. The beams overlap at the detector at a slight angle relative to each other. This will result in the two beams constructively and destructively interfering with each other, causing bright and dark fringes. A first picture, called a "preshot", is taken to see these fringes when both beams are traveling only through air and vacuum. This will be the reference image. Then, during the experiment, or the "shot", plasma is created in the path of one of those beams. As the rays making up this beam cross the plasma, each will experience a phase shift $\Delta\phi$ according to Eq. 2.5:

$$\Delta\phi = -\frac{e^2}{2\omega c m_e \epsilon_0} \int_0^L n_e(x) dx \tag{2.5}$$

where e is an electron's electric charge, ω is the laser's angular frequency, c is the speed of light, m_e is the electron mass, ϵ_0 is the permittivity of free space, L is the length of the plasma through which the laser beam is passing and n_e is

the plasma's electron density. The derivation of this equation can be found in standard plasma physics textbooks.[38]

As the phase of the beam changes, so does the interference pattern and the fringes. Because the phase shift is a function of the plasma electron density, so are the fringe shifts and one can determine the electron density from the fringe shift between preshot and shot. To understand the electron density orders of magnitude that can be measured on COBRA, let us assume that the 532 nm diagnostic laser beam travels through a 1 mm long plasma in which $n_e(x)$ = constant. One fringe shift, i.e. $\Delta\phi = 2\pi$, then corresponds to an electron density of $4.2 \times 10^{18} cm^{-3}$.

2.2.5 Self-emission Diagnostics

A multitude of visible light, extreme ultraviolet (XUV) and X-ray self-emission diagnostics are available to observe the experiments on COBRA. In the visible regime, a 12-frame camera that can take pictures as short as 5 ns with variable time intervals between frames, a streak camera, typically at a 200-500 ns sweep speed, and time-integrated digital SLR cameras were used. The first two are very useful diagnostics for observing plasma initiation and development, as shown in Fig. 2.9 for the 12-frame camera.

The digital cameras are typically used for laser imaging. However, using the right combination of polarizers and neutral density filters, these cameras can be simultaneously used for time-integrated self-emission imaging and time-gated laser imaging, a useful combination. A schematic representation and experimental data using this combination is shown in Fig. 2.8. The self-emission can

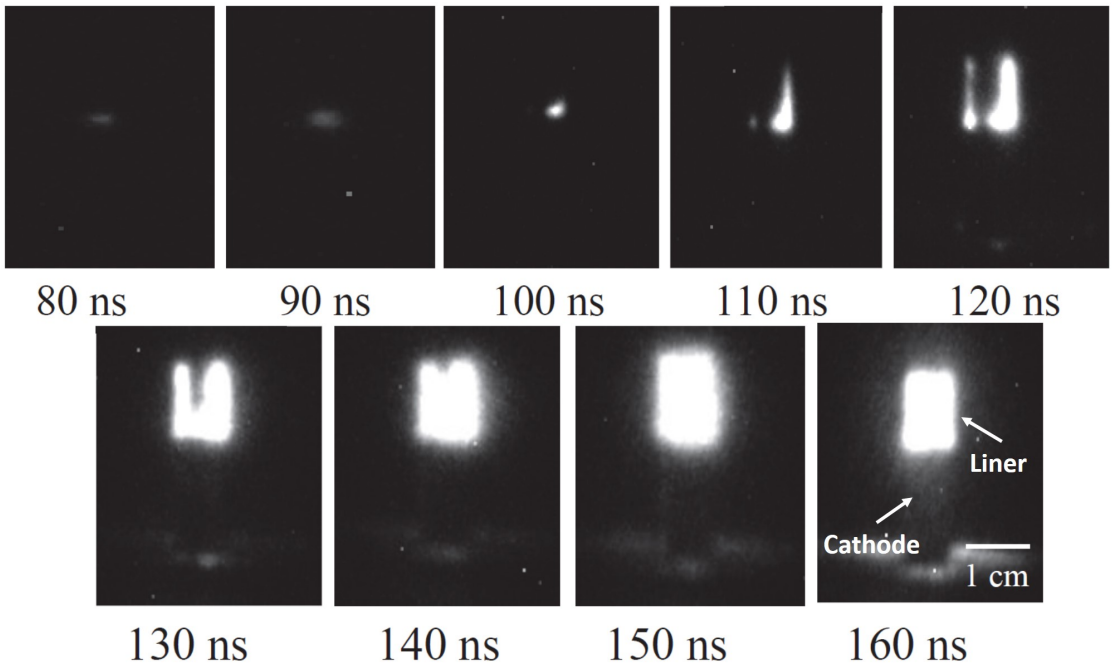

Figure 2.9: Self-emission images from the 12-frame camera using a 50 μm thick 4 mm diameter Al liner. The cathode is at its bottom, the anode at the top. 11 frames had visible features in the experiment shown. The manner in which the liner initiates over time, in this case azimuthally non-uniformly, can be clearly seen.

be seen coming from the liner, whereas the liner's edges are detected from the shadowgraph. We also had access to optical spectrometers on COBRA. However, the phenomena investigated in this thesis were typically not in the right regime for meaningful optical spectroscopy measurements. A number of attempts were made.

In the XUV range, time-gated 4-frame (quad-cam) self-emission pinhole cameras were used. The magnification from pinhole imaging was generally kept around 1. Pinhole sizes were 50 μm, 100 μm, and 200 μm, though 100 μm was most often used. Figure 2.10 shows quad-cam data of an Al liner covered by a half-axial dielectric with an X-pinch in the background using a 100 μm pinhole.

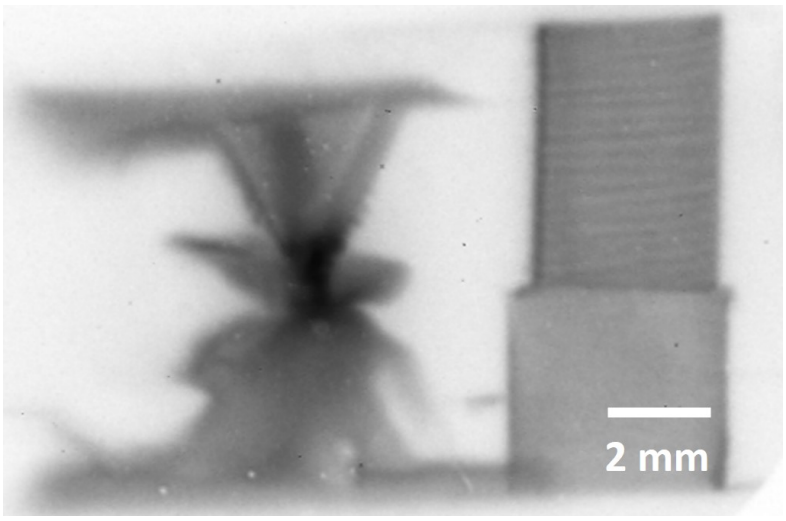

Figure 2.10: XUV self-emission image of an Al liner partly covered by a dielectric on its outer surface. A 4-wire X-pinch is visible in the back. All quad-cam images throughout this thesis are inverted, meaning that darker pixels correspond to stronger self-emission and vice-versa. This appeared to produce more contrast in the images.

In the X-ray range, a streak camera that sweeps from a few to a few hundred ns range and time-integrated self-emission pinhole cameras sensitive up to the X-ray range were used. A sample image from such a pinhole camera is shown for an experiment with 2 X-pinches and a liner, where simultaneous XUV and X-ray imaging is visible. As our liners were typically too massive to implode and remained rather cold, X-ray self-emission diagnostics were not very useful to investigate the liners.

2.2.6 $\dot{B}$ Probe

If we bend a wire into a circle with a small gap at the two ends of the wire, these ends will measure a voltage between them when a time-varying magnetic field is present in the loop. This phenomenon can be understood by applying Faraday's law to the loop, which gives:[37]

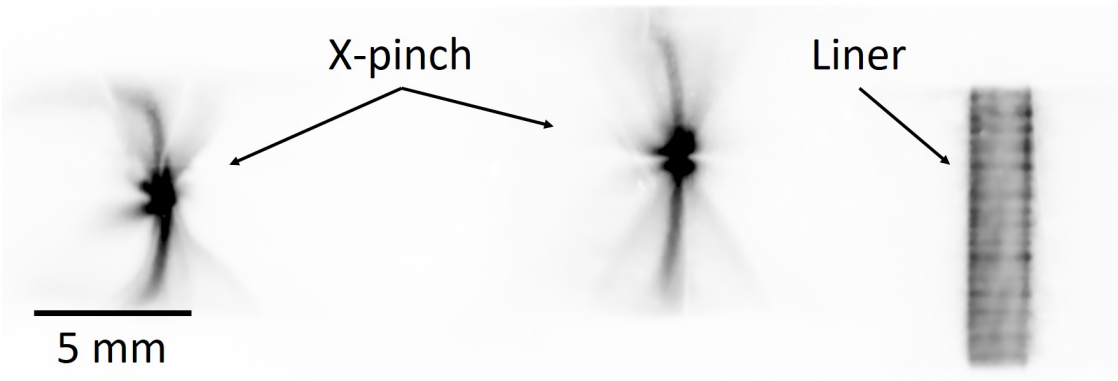

Figure 2.11: Time-integrated X-ray and XUV self-emission imaging from two X-pinches and XUV self-emission imaging from an Al liner using a 50 μm pinhole detector. The image pixel intensity is inverted.

$$V = -A_n \frac{\partial B}{\partial t} \tag{2.6}$$

where V is the voltage generated, A_n is the area of the loop normal to the time-varying magnetic field, and B is the magnetic field. Once a calibrated probe is made, all subsequent probes can be calibrated by comparison with this probe without having to know their area. While Eq. 2.6 is straightforward, the following points need to be considered.

If a certain component of magnetic field is to be measured, for example B_z or B_θ in cylindrical geometry, the other components must be discriminated against. No matter how perfect the probe was made, the orientation of the probes in an experiment was not perfectly aligned in the intended direction as they were typically positioned by eye only, not via a mechanically precise alignment system. The normal of the loop's area could reasonably be expected to have a deviation of up to 10° from the desired magnetic field orientation.

Other points of concern are probe failure due to contact with high energy density plasma and the probe's physical effect on the experiment. Often times

we wish to measure the magnetic field close to the plasma. However, the closer the probe is positioned to the plasma, the more likely that it will fail because of interaction with the plasma, invalidating both the measurement and the experiment. To protect the probe, insulating layers are typically applied over the metallic wire. To see if the probe failed, indicators, such as ensuring the voltage trace returns to zero after the current pulse, must be checked. The probe may interact with the experiment, invalidating the measurement, even if it does not fail. Determining that is very case dependent and can be done by correlating probe results with results from other diagnostics.

Two alternatives for measuring magnetic fields without a physical probe consist of taking adantage of a) Faraday rotation via a probing laser beam or b) the Zeeman effect via plasma spectroscopy.[37, 40] With these methods, there is no disturbance of the plasma and spatially and temporally accurate measurements can be made. One drawback for the Faraday rotation diagnostic is that one can only measure the magnetic field along the rays of the diagnosing laser beam. The caveat for the spectroscopy diagnostic is that one needs the right plasma conditions to be able to use it.

2.2.7 X-pinch Radiography

X-pinch radiography is a simple and effective method for high spatial resolution areal density measurements. Both multi-wire and hybrid X-pinches can be used, each with their own characteristics. Both produce very small source sizes, as small as $\sim 1\mu$m over specific X-ray spectral ranges, and intense X-ray bursts. A comprehensive review of X-pinches is given by Pikuz *et al.*[41, 42]

and Shelkovenko *et al.*[43] The micrometer sized source can be used for point-projection radiography. We position the X-pinch on one side of the object to be imaged and the detector film on the opposite side, as illustrated in Fig. 2.12. The magnification of the image on the detector is determined by the relative distances between detector, load and X-pinch. Moreover, the images shown in Fig. 2.12, taken from Shelkovenko *et al.*,[5] highlight the importance of the distance from the object to the film. Given sufficient distance, refraction enables enhancement of the edges in the image. This is called "phase-contrast imaging".

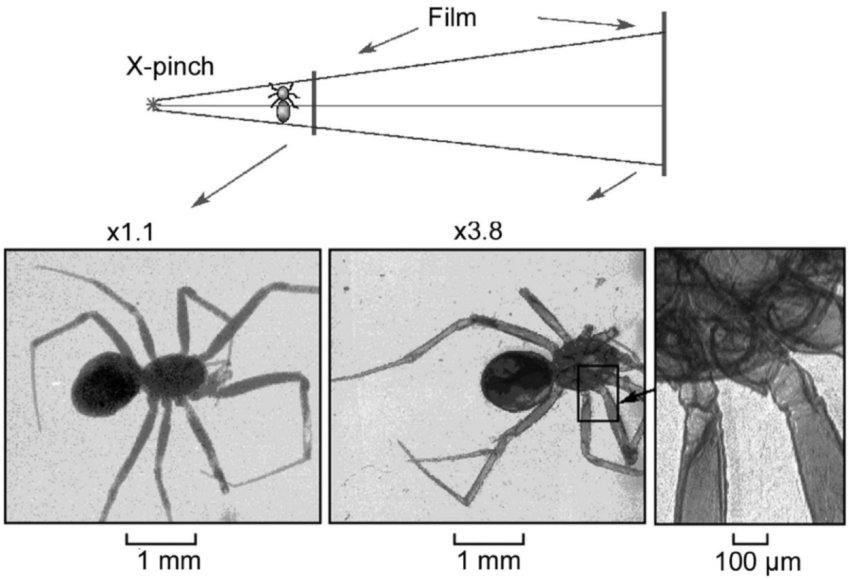

Figure 2.12: X-pinch radiography of a spider, highlighting how the distance between X-pinch, film, and detector can affect the image. Given sufficient distance between object and film, refraction enables enhancement of the edges in the image, which results in "phase-contrast imaging". This effect is not visible in the image with a 1.1 magnification factor, but is clearly demonstrated in the image with a 3.8 magnification factor. Image obtained from Shelkovenko *et al.*[5], licensed under CC BY 4.0.

There are a lot of lower energy photons generated in the X-pinch source for which the source size is $\gtrsim 10$ μm. Consequently, we need to employ a filter in front of the detector made of an appropriate material and thickness to cut out

these photons. The choice of filter will be specific to the X-pinch used.

One can determine the areal density of the foil or plasma load being radiographed via step wedges. To explain, let us assume our experimental load is made of Al. The absorption characteristics for Al in the 1 - 5 keV range, a range typical for many X-pinch sources, is similar for solid room temperature Al and ionized, but relatively cold, Al (e.g., up to 100 eV). At high enough temperatures the Aluminum's opacity curve will deviate significantly, but that is not a concern for our relatively low plasma temperature experiments. We can position a step wedge made of solid Al in front of the detector, as shown in Fig. 2.13. This is just a number of increasing layers (steps) of foil, in our case made of Al, positioned on top of each other. The thickness of the steps should be small and will determine the areal density resolution of the diagnostic. When we position the detector for the step wedge measurement, we need to ensure that the step wedge will not be exposed to the X-ray source through the load but directly through vacuum. The X-pinch is an isotropic radiation source and we want to radiograph the load and the step wedge separately, but using the same X-pinch source. We can then match pixel intensity values of step wedge radiography with load radiography. Matching values corresponds to equivalent amounts of X-ray absorption by the Al, hence an equal mass of Al being present in the rays' path. If the absorption length through the load is known, this will give a density value. If it is not, this will give an areal density value. The example was given for Al but can be done with many materials. The key criterion is for the absorption characteristic in the spectral range of interest to be similar through the solid step wedge material and the generated plasma.

On COBRA, a significant source of error in step wedge measurements can

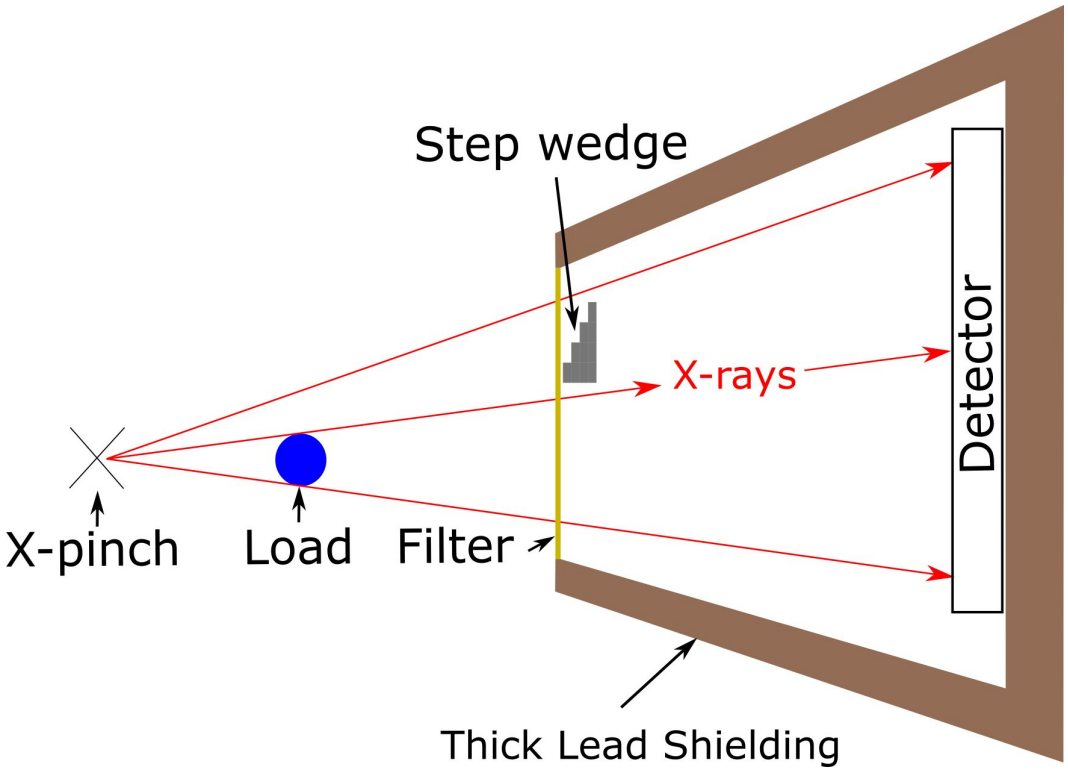

Figure 2.13: X-pinch radiography setup that includes a step wedge for areal density measurements as well as shielding against stray radiation. The filter and step wedge being placed some distance away from the detector, as shown, produced the best results in our experiments.

come from high energy photons that are present in the experimental chamber. They can have many sources, such as the X-pinch, bremsstrahlung radiation created from electrical breakdown near the load, etc.[44] If the detector is not properly shielded, the high energy photons can pass through the material that is housing it. To block the rays from entering the sides or the back of the detector, it is practical to use thick lead shielding, as shown in Fig. 2.13. The front of the detector, where the imaging X-rays are intended to pass, cannot be shielded against the higher energy photons in such a manner as the lower energy imaging X-rays would be attenuated along with the harder radiation.

Empirically, placing the filter and step wedge some distance away from the

detector, of the order of 30 cm, produced the most trustworthy step wedge results in our experiments (the average areal density measured through a 16 μm Al foil matched the expected average within 5%).

2.2.8 Photoconductive Diode

To measure X-ray radiation, photodiodes were used with filters attached at the front. The filters were chosen to block lower energy photons. The two types of photodiodes used were Si-diodes and diamond photoconducting diodes. Si-diodes are semiconductors with a p-n junction, where photons incident to the diode create electron-hole pairs that generate current. The Si-diodes were used in a reverse biased configuration, where the p-type junction is attached to the cathode and the n-type junction is attached to the anode, at -40 V. In diamond photoconductors, the photocurrent generation mechanism is different. The diamond is placed between two electrodes that are biased to a certain voltage, -300 V in our experiments. The incident radiation on the diamond crystal will create mobile charges that will generate a current due to the applied voltage. We can relate that current to the amount of radiation via calibration.

These detectors were not used to measure the absolute flux of X-rays. They were used as discussed in Chapter 5 to determine when X-rays were produced from the X-pinch.

CHAPTER 3

THEORY

3.1 Z-pinch

In this Chapter, a brief theoretical background discussing relevant aspects of the Z-pinch to the work in this Thesis will be presented. First, the stages of the Z-pinch will be discussed briefly and the action, or current, integral will be introduced and explained. Then, both "electrothermal" and "electrochoric" instabilities will be derived. These instabilities will be compared with experimental data in Chapter 5.

3.1.1 Stages

In a wire array or liner Z-pinch, the dynamics can be divided into four stages: initiation, ablation, implosion, and stagnation. In the case of a liner, initiation includes everything from the start of the current pulse up to plasma formation on the surface of the liner. During the initiation stage, the surface layer of an ideally clean liner material will melt, vaporize, and ionize to form a plasma.

An important parameter to keep in mind is the electromagnetic skin depth

$$\delta_{skin} = \sqrt{\frac{2\eta}{\omega\mu}} \tag{3.1}$$

where η is the electrical resistivity, ω is the current pulse angular frequency and μ is the magnetic permeability of the liner material. This parameter will determine how quickly a current pulse diffuses into and through a metal conductor.

With this parameter in mind, there are two categories of metal liners: thick and thin. If the liner thickness, δ_{liner}, is larger than δ_{skin}, the current will not diffuse throughout the whole conductor. If $\delta_{liner} < \delta_{skin}$, the current will eventually flow through the entire liner. This difference will have varying consequences, such as the presence or absence of plasma radially inside the cylindrical liner before liner implosion. It is also important to note that δ_{skin} is only an estimate as it does not account for liner heating and possible nonlinear diffusion, and so it must be considered as a lower limit only. Specifically, the resistivity of most metals increases as the material is heated, but the resistivity value used in the estimate usually corresponds to the room temperature condition.

In wire-array Z-pinches, the ionization step in the initiation can be clearly seen in the load voltage trace. In a Z-pinch, the terms contributing to the voltage are:

$$V = RI + L\frac{dI}{dt} + \frac{dL}{dt}I \tag{3.2}$$

where V is the voltage, R is the load resistance, I is the current and L is the load inductance. If the load does not implode, the last term can be dropped. Once plasma forms on the surface of the wire(s), it quickly heats and drops in resistivity, at which point the first term can be dropped. There is a corresponding drop in the voltage waveform. [9, 44]

In the case of a cylindrical metal liner, such a drop is not as visible. This is due to a few factors that cause plasma heating, and hence voltage collapse, to be more gradual. First, the inductive voltage difference between current flowing through the outer surface plasma and the inner condensed matter can be very small. The radius of the liner, i.e., where condensed matter exists, is of the order

of millimeters. Initial surface plasma will extend this radius by just a few hundred μm. This causes little inductive voltage difference between the paths. For wires, the corresponding relative voltage difference is larger, which will lead the current to preferentially flow in the plasma. Second, there is more total mass to heat up in a liner, causing the current to heat the surface plasma and drop its resistivity at a slower rate.

After initiation is the ablation phase. At this stage, plasma has formed on the surface of the condensed matter region. The plasma carries an increasing amount of current over time as it is heated. Since the plasma is in contact with the liner, it will drive ablation on the surface of the liner. If the conductor is thick, plasma will exist only on the outer surface and hence the inward $J \times B$ force will cause the plasma mass to accumulate on the outer surface of the liner. This mass will not be able to move further inward at this stage. If the conductor is thin enough, the current will diffuse very quickly through the metal and cause bulk heating of the liner. In this case, plasma will exist on both the inner and outer sides of the condensed matter region. The inner plasma will move radially inward [44], somewhat similar to the dynamics in wire-arrays [9]. For liners in general, the situation is further complicated by the possible presence of shock waves inside the metal propagating radially inward. [45, 46, 21]

If the current pulse being delivered has enough energy and a long enough rise-time, the liner will radially implode. The larger the cross-sectional mass of the liner, the larger the above pulse parameters need to be. An implosion reaching the axis will result in stagnation, the last stage of the Z-pinch. At this point, all of the kinetic energy from the inward moving mass is thermalized due to collisional stagnation of the imploding liner material on the liner axis. Strong

bursts of X-rays are emitted at this moment from hot spots that develop along the axis due to the classical Z-pinch sausage instability.[9]

A useful dimensionless parameter that can be used to optimize the liner thickness and radius for a given pulsed power machine is the Π parameter [8]. Let's assume we have a thin annular shell that is being driven by a current I. In the simplest case, the equation for radial motion is given by

$$\frac{m}{2\pi r}\frac{d^2r}{dt^2} = -\frac{B^2}{2\mu} = -\frac{\mu I^2}{8\pi^2 r^2} \tag{3.3}$$

where μ is the material's magnetic permeability, I is the current delivered, B is the corresponding magnetic field using Ampere's law, m is the mass per unit length of the pinch, and r is the radius of the annulus at the given time t.

Non-dimensionalizing via $\widetilde{r} = r/r_0, \widetilde{t} = t/\tau$, and $\widetilde{I} = I/I_{max}$, this leads to:

$$\widetilde{r}\frac{d^2\widetilde{r}}{d\widetilde{t}^2} = -\Pi\widetilde{I}^2; \Pi = \frac{\mu I_{max}^2 \tau^2}{4\pi m r_0^2} \tag{3.4}$$

where I_{max} is the maximum current delivered, τ is the current pulse rise-time to I_{max}, and r_0 is the initial radius of the liner. One can show that the kinetic energy of the liner in the implosion is maximized when Π is approximately 4 for a current that rises as $sin^2(\frac{\pi t}{2\tau})$.[8] For a 1 MA, 100 ns rise time pulse using a 4 mm diameter Al liner, this optimization leads to a liner thickness of $\approx$ 2 μm. While we have never used such thin liners in our experiments, we have consistently observed implosion occurring when a 4 μm thick liner was used with the other parameters mentioned.

The research discussed in this Thesis has involved investigating effects occurring during the initiation and ablation phases of a Z-pinch. As such, our

liner parameters were, for the most part, specifically chosen to be too heavy to implode during the COBRA power pulse, regardless of whether the pulse rise-time was the 100 ns short pulse or the 250 ns long pulse.

3.1.2 Action, or Current, Integral

While the focus at LPS is naturally the study of plasmas, actual experiments start from a cold state, typically either solid or gas. The initial conditions of the plasma generated from the solid or gas will depend on the processes occurring when current starts to flow in the early cold stage. Section 3.2 presents theory proposed in literature for the cold condensed matter stage before initial generation of plasma. A lot of what will be described strongly depends on the phase of the material, be it solid, liquid, vapor or some phase transition between them. However, no diagnostics were fielded to determine the state of the non-ionized material during our experiments. To counter this problem somewhat, an approximate calculation can be used to determine the state of the bulk of the material at a given time in a pulsed power experiment.

That approximation is the current, or action, integral. Consider only Ohmic heating in the energy balance of a solid material driven by a current pulse:

$$\rho c_v \frac{\partial T}{\partial t} = \eta J^2 \tag{3.5}$$

where ρ is the mass density, c_v is the heat capacity, T is the temperature, η is the resistivity, and J is the current density. Rearranging terms and integrating over time, we write:

$$\int \rho c_v \frac{1}{\eta} \frac{1}{\frac{d\eta}{dT}} d\eta = \int J^2 dt \tag{3.6}$$

The term on the right is called the action, or current, integral (typically confusingly denoted as J). In a solid or liquid state, the terms on the left other than η do not vary rapidly with temperature based on tabulated data [47, 48, 49]. Pulling them out of the integral and integrating to the time it takes to reach the melting point, we obtain:

$$\frac{\rho c_v}{\frac{d\eta}{dT}} [ln(\eta_{melt}) - ln(\eta_{initial})] \approx \int_0^{t_{melt}} J^2 dt \tag{3.7}$$

We can first compute the left side of the equation from the tabulated thermodynamic and electrical values and can then find t_{melt} given our current profile.

Using the current integral to estimate melt and vaporization times assumes the current density is uniform and no non-linear effects, such as propagating shocks, are present. Conductors whose thickness, δ_{wall}, is $\gtrsim \delta_{skin}$ would create non-uniform current density profiles. That's not an issue in our experiments as the integral was calculated only for liners with $\delta_{wall} \ll \delta_{skin}$. Deviations from the estimate may occur due to bad electrode contacts with the experimental load, creating arcs and plasma near those regions, leading to part of the current not flowing in the liner there. Further deviations will exist due to the changing heat capacity with temperature, which is material dependent.[47] For example, Al's heat capacity changes by 25 $\%$ between room temperature and the melting point. Other deviations will occur due to the presence of unaccounted for adsorbed gases that will affect the initial plasma formation. Once plasma, vapor, liquid, and possibly solids exist simultaneously, complicated behavior may

occur due to the different thermodynamic and electromagnetic properties. An example of such behaviour is described in Section 3.2.

3.2 Current Driven Low Temperature Instabilities

One of the main topics of investigation in this Thesis, as will be described in Chapter 5, is micrometer scale density features that are present in the liner. A potential explanation provided in literature for such features is the combination of the condensed matter "electrothermal instability" (ETI) together with the"electrochoric instability" (ECI). [50, 6, 8] For these instabilities, an analytic derivation will be provided along with a qualitative explanation. Even though providing the references and the final equations might be sufficient, the derivations are provided because they are are not found in plasma physics textbooks and these instabilities are a central theme in my work.

3.2.1 Electrothermal Instability (ETI)

In order to derive the linear growth rate of the ETI, assume a planar infinitesimally thin conductor with its surface's normal in the x direction. A representation of this initial setup is given in Fig. 3.1. Assume there exists a non-zero E_z, J_z and B_y. From Ohm's law

$$\eta \boldsymbol{J} = \boldsymbol{E} \tag{3.8}$$

Applying linear perturbation theory, we assume $\boldsymbol{E} = \boldsymbol{E}_0 + \boldsymbol{E}_1$, $\boldsymbol{J} = \boldsymbol{J}_0 + \boldsymbol{J}_1$,

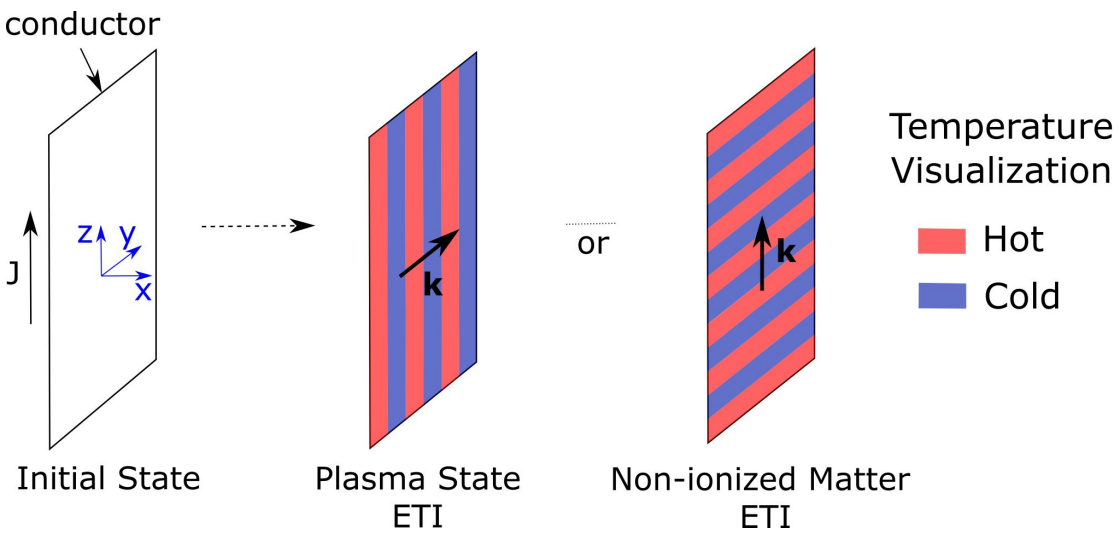

Figure 3.1: Schematic diagram depicting the physical configuration used in the derivation of the ETI and the resulting instabilities. These pictures are explained in Section 3.2.

and $\boldsymbol{B} = \boldsymbol{B}_0 + \boldsymbol{B}_1$, where $E_{z0}, J_{z0}, and B_{y0}$ are the only non-zero zeroth order quantities. Let us assume the perturbation to be $\sim e^{\Gamma t + ik_y y + ik_z z}$, meaning it is in the direction parallel to the surface. Furthermore, let us express the electrical resistivity as $\eta = \eta_0 + \delta\eta(T)$. Linearizing Ohm's law, we find

$$\begin{aligned} E_{z1} &= \eta_0 J_{z1} + J_{z0}\delta\eta \\ E_{y1} &= \eta_0 J_{y1} \end{aligned} \tag{3.9}$$

Let us assume no current flows outside the conductor so that the magnetic field there well be curl free and hence can be represented by the gradient of a scalar $\boldsymbol{B}_1 = -\nabla\psi$. Setting the divergence of the magnetic field to zero leads to Laplace's equation $\nabla^2\psi = 0$. Placing the conductor at the origin leads to a solution of the form

$$\psi_\pm = A_\pm e^{\mp kx} \tag{3.10}$$

where $\pm$ represents the $x > 0$ and $x < 0$ regions, $k = \sqrt{k_y^2 + k_z^2}$, $A_\pm = C_\pm e^{\Gamma t + ik_y y + ik_z z}$ and C is a constant. Using the boundary conditions at $x = 0$

$$\begin{aligned} B_{x1+} = B_{x1-} &\Rightarrow A_+ = -A_- \\ B_{y1+} - B_{y1-} &= -ik_y A_+(e^{-kx} + e^{kx}) = \mu J_{z1} \\ B_{z1+} - B_{z1-} &= -ik_z A_+(e^{-kx} + e^{kx}) = -\mu J_{y1} \\ &\Rightarrow J_{y1} = -\frac{k_z}{k_y} J_{z1} \end{aligned} \tag{3.11}$$

where μ is the magnetic permeability.

Furthermore, at $x = 0$

$$B_{x1} = \frac{B_{x1+} + B_{x1-}}{2} = \frac{kA_+(e^{-kx} + e^{kx})}{2} = \frac{-k\mu J_{z1}}{2ik_y} \tag{3.12}$$

Taking the x-component of Faraday's law in the x = 0 plane

$$ik_y E_{z1} - ik_z E_{y1} = -\Gamma B_{x1} \tag{3.13}$$

Plugging in Eq. 3.9 and Eq. 3.12 in Eq. 3.13, using Eq. 3.11 to replace J_{y1} and rearranging terms, we get

$$J_{z1} = -J_{z0} \frac{cos^2\alpha}{1 + \frac{\Gamma}{\Gamma_0}} \frac{\delta\eta}{\eta_0} \tag{3.14}$$

We can use that equation to obtain

$$\delta(\eta J_z^2) = \delta\eta J_z^2 + 2J_z \delta J_z \eta = J_z^2 (1 - \frac{2cos^2\alpha}{1 + \frac{\Gamma}{\Gamma_0}})\delta\eta \tag{3.15}$$

where $\Gamma_0 = \frac{2k\eta}{\mu}$, α is defined as the angle between the y and k directions, and the subscript notation is changed to have the same notation as found in literature [8, 50], the $_0$ subscript being dropped and the $_1$ subscript being replaced by a δ.

Next, let us consider the energy balance in the absence of motion, considering only ohmic heating and thermal heat conduction for a current driven solid conductor. Using $\epsilon = c_v T$ where we approximate the heat capacity, c_v, to be constant in time, we find

$$\rho c_v \frac{\partial T}{\partial t} = \eta J_z^2 + \nabla \cdot (\kappa \nabla T) \tag{3.16}$$

where ρ is the mass density and κ is the thermal conductivity.

Taylor expanding the resistive heating term around T_0 gives $\eta J_z^2 = \eta J_z^2|_{T_0} + T_1 \frac{\partial(\eta J_z^2)}{\partial T}|_{T_0}$. Assuming the thermal conductivity is uniform in space and applying the same perturbation $\sim e^{\Gamma t + ik_y y + ik_z z}$ as before, we obtain

$$\rho c_v \Gamma T_1 = J_z^2 \frac{\partial \eta}{\partial T}(1 - \frac{2cos^2\alpha}{1 + \frac{\Gamma}{\Gamma_0}})T_1 - k^2 \kappa T_1 \tag{3.17}$$

Therefore, we have

$$\Gamma = \frac{J_z^2 \frac{\partial \eta}{\partial T}(1 - \frac{2cos^2\alpha}{1+\frac{\Gamma}{\Gamma_0}}) - k^2\kappa}{\rho c_v} \tag{3.18}$$

Equation 3.18 is dependent on the angle α. If the resistivity decreases with increasing temperature, such as in a plasma described by Spitzer resistivity, then to maximize the growth rate we will want to maximize $cos(\alpha)$. This happens at $\alpha = 0°$, meaning the instability wavevector will be parallel to the self-generated

magnetic field and the hot and cold filaments will be aligned with the orientation of the current, as shown in Fig. 3.1. If the resistivity increases with temperature, such as is typically the case for condensed matter states, then we will want to minimize $cos(\alpha)$. This corresponds to an angle of 90°, or in other words a wavevector parallel to the driving current, as shown again in Fig. 3.1. In this case, the instability growth rate simplifies to:

$$\Gamma = \frac{J_z^2 \frac{\partial \eta}{\partial T} - k_z^2 \kappa}{\rho c_v} \tag{3.19}$$

Figure 3.2 shows plots of Eq. 3.19 for four materials, Al, Cu, Ti and Ni. Their thermodynamic parameters are taken near the melt phase transition approaching from the solid region [47], hence the label λ_{sm} in Fig. 3.2. To determine a value for the current density, we assumed the same 1.1 MA 120 ns current pulse for all materials and computed the melt time and corresponding current density from action integral estimates.

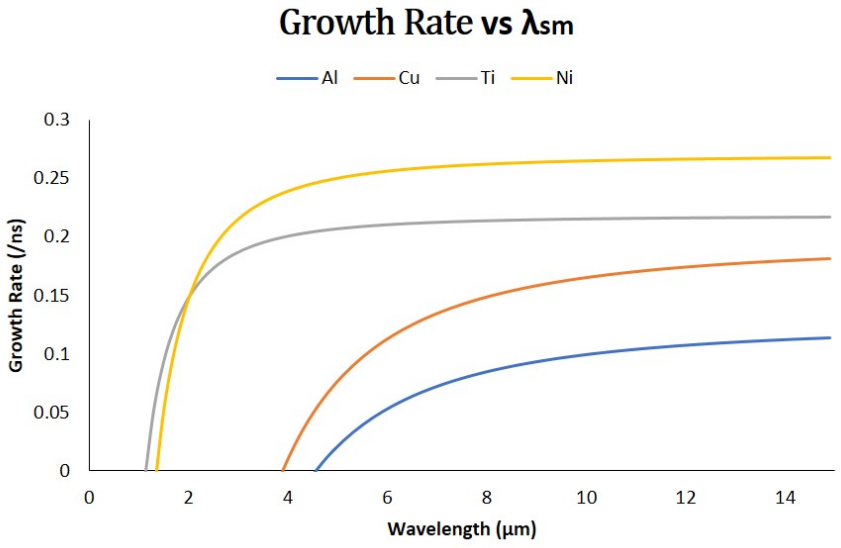

Figure 3.2: Instability growth rate for Al, Cu, Ti and Ni using thermodynamic values in the melt transition phase approaching from the solid region.

A value that will be used later on is the wavelength below which there is no instability growth. Equating the growth rate to zero in Eq. 3.19 and solving for the wavelength, we find:

$$\lambda_{min} = \frac{2\pi}{J_z}\sqrt{\frac{\kappa}{\frac{\partial \eta}{\partial T}}} \tag{3.20}$$

Any wavelength below this is stabilized by the thermal conduction term, hence the label λ_{min}. But while λ_{min} gives the minimum threshold, it gives no indication as to the maximum threshold. To understand where an upper wavelength limit comes from for the instability, we need to account for density and motion perturbations in the equations. This will lead to the term responsible for the electrochoric instability and will be discussed in the next section.

Qualitatively, the plasma ETI matches the current filamentation instability. Assume there is initially small variation in current magnitude in adjacent current channels between anode and cathode. This assumption can hold in experiments due to non-uniform contact gaps between the electrodes and the experimental load, spatially non-uniform current pulse delivery, etc. The channel with higher current will heat its plasma faster, causing the latter to be less resistive than the plasma beside it. This will lead to lowering that channel's resistive voltage and hence drawing more current into the channel, heating that channel at a faster rate. Overall, that creates an unstable cycle where initially small differences in current magnitude between adjacent current channels will amplify, forming an increasing temperature and current differential between these channels.

The non-ionized matter electrothermal instability, where $\frac{d\eta}{dt} > 0$, is a little

more difficult to understand. However, some simulation results [6] suggest the following interpretation. Assume a cylindrical metal load, as illustrated in Fig. 3.3. Further assume that there are localized hot spots in the material, perhaps due to material impurities, geometric non-uniformities in the load, etc., leading to non-uniform ohmic heating. The current will shift away azimuthally from these hotter, hence more resistive, spots toward adjacent colder regions with less resistance. In turn, this adjacent material will experience a higher current density which will cause it to heat at a faster rate and become more resistive than the material beside it. This creates an unstable cycle and leads to growth of the features in the azimuthal direction. One qualitative argument that we propose can limit azimuthal growth is the following. The more the instability expands azimuthally, the larger the voltage of the current channel due to the bent and longer current path. This leads to a smaller current magnitude through that channel, mitigating growth.

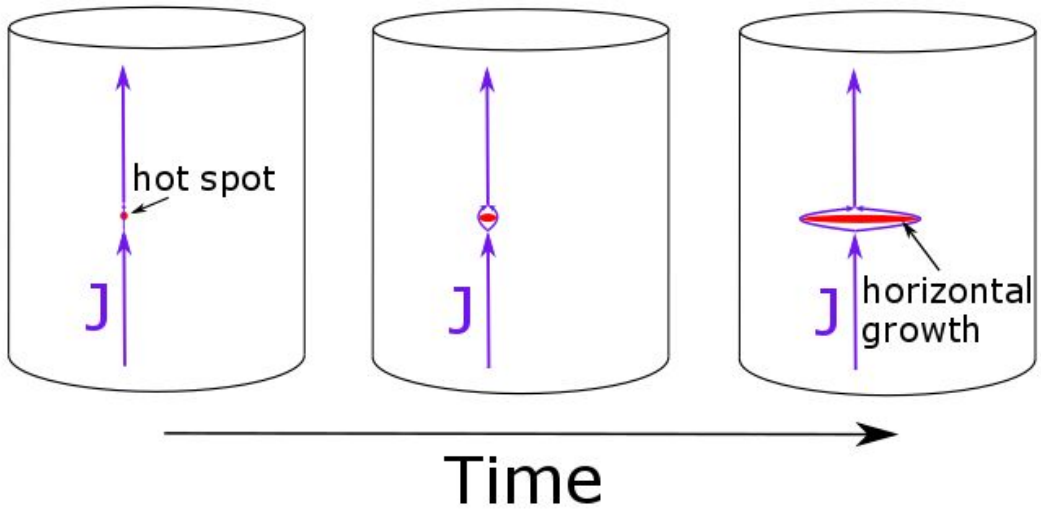

Figure 3.3: Schematic diagram showing the growth of non-ionized matter electrothermal instability with time.

3.2.2 Electrochoric Instability (ECI)

We will now allow for motion and density variation of liner material. The variation will be assumed to be only in the axial, or z, direction. Conservation of mass, momentum and energy will be used. For the thermodynamic parameters, we will not only allow for variation in temperature as before, but also for density, i.e., have both T_1 and ρ_1. Furthermore, we will assume that the $\mathbf{J} \times \mathbf{B}$ term is negligible. The linearized mass, momentum and energy equations are

$$\begin{aligned} \frac{\partial \rho_1}{\partial t} + \rho \nabla \cdot \boldsymbol{v}_1 &= 0 \\ \rho \frac{\partial \boldsymbol{v}_1}{\partial t} &= -\frac{\partial p}{\partial \rho} \nabla \rho_1 - \frac{\partial p}{\partial T} \nabla T_1 \\ \rho c_v \frac{\partial T_1}{\partial t} + \rho_1 c_v \frac{\partial T}{\partial t} &= J_z^2 \left(\frac{\partial \eta}{\partial T} T_1 + \frac{\delta \eta}{\delta \rho} \rho_1\right) - p \nabla \boldsymbol{v}_1 + \kappa \nabla^2 T_1 \end{aligned} \tag{3.21}$$

To approximate a relationship for the pressure during liquid, vapor, and "biphase" (liquid+vapor) states, the following approximate form may be used:

$$p = C \rho^a T^b \tag{3.22}$$

where C, a, and b are constants determined empirically using Equation-of-State (EOS) tables. Oreshkin argues that this empirical approximation is justified because it is the qualitative behavior that is of interest here and that the constants a and b can be determined up to an accuracy of 30 $\%$, resulting in an acceptable error bar for that purpose. Note that the constants are different for the different phases.

Using the perturbation form $\sim e^{\Gamma t + i k_z z}$, the conservation equations become

$$\begin{aligned}
\rho_1\Gamma + ik_z\rho v_1 &= 0 \\
\rho v_1\Gamma &= -ik_z p(a\frac{\rho_1}{\rho} + b\frac{T_1}{T}) \\
\rho c_\upsilon T_1\Gamma + \rho_1 c_\upsilon\frac{\partial T}{\partial t} &= J_z^2(\frac{\partial\eta}{\partial T}T_1 + \frac{\delta\eta}{\delta\rho}\rho_1) - ik_z p v_1 - k_z^2\kappa T_1
\end{aligned} \tag{3.23}$$

Combining the equations and solving for Γ, we find

$$\Gamma = \frac{J_z^2\frac{\partial\eta}{\partial T} + \frac{\rho}{T^*}(c_\upsilon\frac{\partial T}{\partial t} - J_z^2\frac{\partial\eta}{\partial\rho}) - k_z^2\kappa}{\rho c_\upsilon + \frac{p}{T^*}} \tag{3.24}$$

where $T^* = T \times (\frac{a}{b} + \frac{\Gamma^2\rho}{k_z^2 bp})$.

Equation 3.24 displays some interesting qualitative behavior. Compared to the ETI, the growth rate is now additionally dependent on the temperature change with time as well as resistivity change with density for the given material. To solve this equation, note that it is actually a third order equation in Γ due to the Γ^2 term in T^*. However, in the range of interest for the variables, this equation turns out to have two imaginary solutions, which describe damped oscillations, and one real root, that is the solution of interest.

Oreshkin, using EOS tables compiled from Sandia National Labs, shows instability growth results for Al in the liquid state at T = 0.4 eV, $\rho \approx 1.57$ g/cm^3 and J = 10^8 A/cm^2.[50] The largest change from the ETI theory without motion occurs when $\frac{\partial\eta}{\partial\rho}$ is included. This is the term that would lead one to expect a dominant wavelength for the instability, or at least a dominant range that is near λ_{min}. This is currently the only addition to the ETI that gives a range for the instability, as opposed to just a λ_{min}.

At this point, a clarification needs to be made in the nomenclature of the instabilities. ECI, which depends on $\frac{\delta\eta}{\delta\rho}$ as will be described below, only oc-

curs at the onset of vaporization. [6] The instability behavior in the liquid state described above also depends on $\frac{\delta\eta}{\delta\rho}$. To clearly label what instability is being discussed in the following discussion, we will use the terms "ETI", "ETI_{liquid}", and "ECI" for the instability corresponding to Eq. 3.19, the instability in the liquid phase, and the instability at the onset of vaporization respectively.

A qualitative explanation for the importance of the ECI was given by Pecover *et al.* [6] and is as follows. Assume, again in a cylindrical geometry, you have slightly hotter and colder azimuthal bands in your material. Such temperature bands will cause the hotter regions to vaporize at a slightly earlier time. When a material vaporizes, its pressure jumps by orders of magnitude during the phase change. This in turn leads to the vapor from the hot bands quickly diffusing out into the vacuum region. However, as the vapor diffuses and its density drops, its resistivity increases by orders of magnitude.[6]

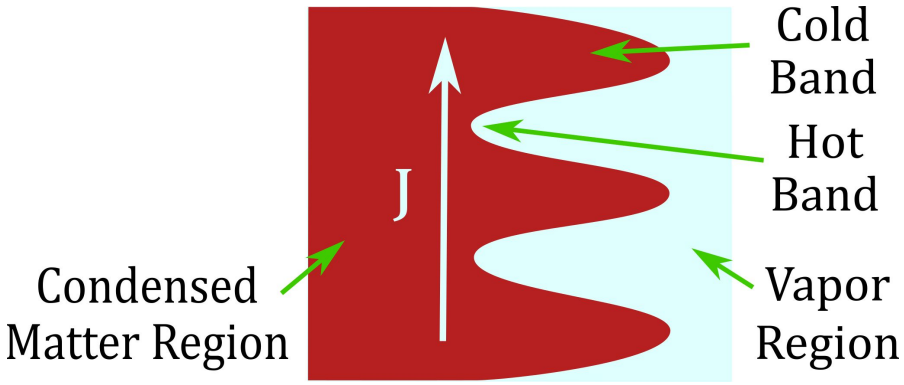

Figure 3.4: Schematic helping visualize the increased lifetime of the ripple shaped contour due to the ECI. [6]

Hence the current will quickly resistively diffuse into the inner non-vaporized dense regions. The argument now, based on GORGON simulation results,[6] is that to lower the resistive voltage, the current will diffuse inward even in the outer spiked regions so that it can flow axially straight instead of following a ripple shaped contour. A schematic depicting this visually is shown in

Fig. 3.4. As the spikes are now getting heated at a much slower rate, their lifetime increases significantly, creating a large amplitude instability. Hence, ECI may be thought of as an amplification mechanism to an original axial temperature perturbation.

To end this section, let us discuss the validity of the seeding assumptions for the ECI and the ETI_{liquid}. In the former, we assumed the existence of azimuthal temperature bands. Such bands can be produced by the ETI_{liquid}, which, as discussed, results in an axial temperature perturbation with a certain dominant wavelength range. In thin liner experiments that use metal foils with an ingrained axial mass variation, temperature differences can also be expected due to varying heating rates within different axial cross-sections (same total current heating varying amounts of mass). Such experiments will be discussed in detail in Chapter 5. For ETI_{liquid}, we assumed in Eq. 3.23 that the perturbation is only in the axial direction. Both in experimental work found in literature [51, 52, 20] and our work presented in Chapter 5, the visible features' structure is approximately perpendicular to the current flow direction, agreeing with the approximation. The question then is why. The assumption arguably holds because the ETI_{liquid} is seeded by the ETI. ETI is a temperature perturbation that grows without any required motion. Hence it would start to grow right from the beginning of the current pulse while the material is still in the solid phase. For a typical COBRA short pulse using Al for example, melt should occur roughly 50 ns into the pulse based on an action integral approximation. This is considerable time for the ETI to grow. Hence, the ETI in the liquid state will have a preseeded temperature perturbation with the wavevector in the z direction. Such seeding, even though lacking a dominant wavelength, would lead to the largest ETI_{liquid} growth occurring in that same z direction.

CHAPTER 4

X-PINCH RADIOGRAPHY APPLIED TO A CYLINDRICAL METAL LINER

4.1 Motivation

X-ray radiography is a common diagnostic in a wide array of applications such as medical imaging, product inspection for material integrity, airport security, etc. In the field of plasma physics, it is very useful for probing high density regions of a plasma, including plasmas within a solid "container", such as a cylindrical hohlraum or liner. For example, it was used in the Magnetized Liner Inertial Fusion (MagLIF) experiments that showed the existence of a helical structure in the liner when an axial magnetic field was applied [36]. In those experiments, monochromatic X-rays were produced using a laser source. Another source of X-rays that can be used for dense plasma radiography in the $\leq$ 5 keV range is the X-pinch [41, 42, 43], a very small and broadband source that can lead to high resolution imaging described briefly in Chapter 2. If the experiment uses a pulsed power machine designed to drive sufficiently high current, then a benefit is the ability to put an X-pinch in series or in parallel with the main experimental load so that a separate X-ray driver is not needed. This is especially useful when a high-power laser is not available to produce X-rays.

In this Chapter, we will describe a means to use radiography to directly observe the development of μm scale structure in the dense regions of a metal liner, both with and without dielectric coatings. We will also make use of a method that allows looking though only one layer of liner, as opposed to the default of two layers, by employing a slit. We will then compare images from two types of detectors, image plate and film, showing the difference in results from simi-

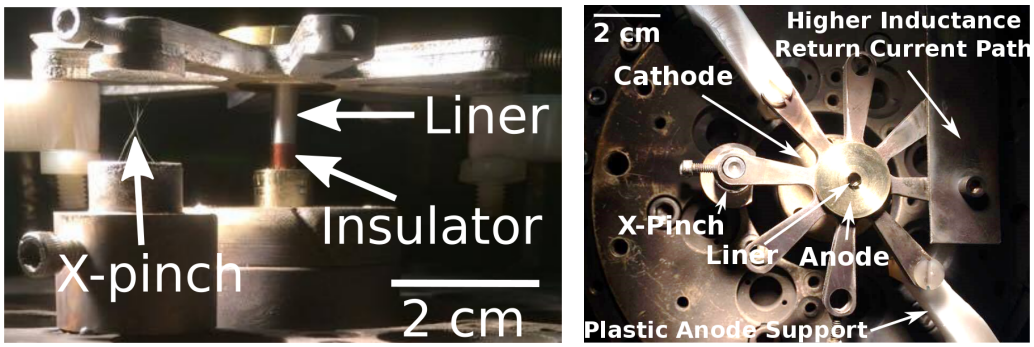

(a) (b)

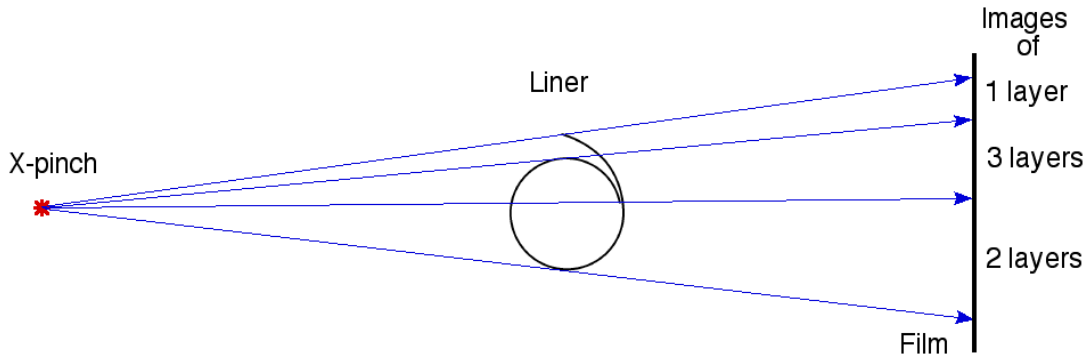

(c)

Figure 4.1: (a) Side view and (b) top view of a half-insulated Al liner setup. The 11 mm long, 16 μm thick liner in the center is surrounded by a 4 mm long 50 μm thick solid insulator. There is a 4-wire 25 μm Mo X-pinch positioned in place of one of the return current posts. The second return current post is positioned radially farther out than the X-pinch in order to increase its relative current path inductance. The anode is held in place by the white plastic supports. (c) Top view schematic representation of a liner showing X-ray paths through different layers of foil. The diagram is not to scale.

lar experiments. Finally, we will discuss extra diagnostic protection needed in experiments with solid dielectrics due to the presence of destructive debris.

4.2 Experimental Arrangement and Diagnostics

4.2.1 Liner and X-pinch Setup

A sample experimental configuration is shown in Fig. 4.1. There is a 4.2 mm diameter, 11 mm long, and 16 μm thick cylindrical Al foil liner located in the center of Fig. 4.1 (a), serving as the load of COBRA. It is made by taking flat Al foil, wrapping it once around a rod, positioning it between anode and cathode holders, letting the foil's elasticity expand it against the inner wall of the holders (e.g., the hole in the brass anode in Fig. 4.1 (b)), and finally removing the rod. Similar wrapping methods have been used in previous experiments; another group used foils as thin as 400 nm [53]. Such methods allow using sufficiently thin liners to enable radiography through the solid regions of the liner. A schematic diagram of what the X-ray radiography detector sees in such foil setups is shown in Fig. 4.1 (c). Using the Center for X-ray Optics' (CXRO) free online database, we show in Fig. 4.2 that there is very little transmission through 50 μm Al, but there is significant transmission for 10 μm Al over a portion of the $\approx$ 1 - 4 keV X-ray emission region of a Mo wire X-pinch [42]. As foils generally enable liner thicknesses and tolerances that are much smaller than is practical to machine, they are an attractive means to make liner loads for 1 MA pulsed power generators.

A clear disadvantage of using foils in the manner described above is the lack of symmetry this will induce near the overlap region in the wrapped foil. Complete azimuthal symmetry must be not of vital importance to the experiment if this configuration is to be valid. Furthermore, if symmetry is not critical, a narrow axial slit can be made, as shown in Fig. 4.3 (a), for radiography pur-

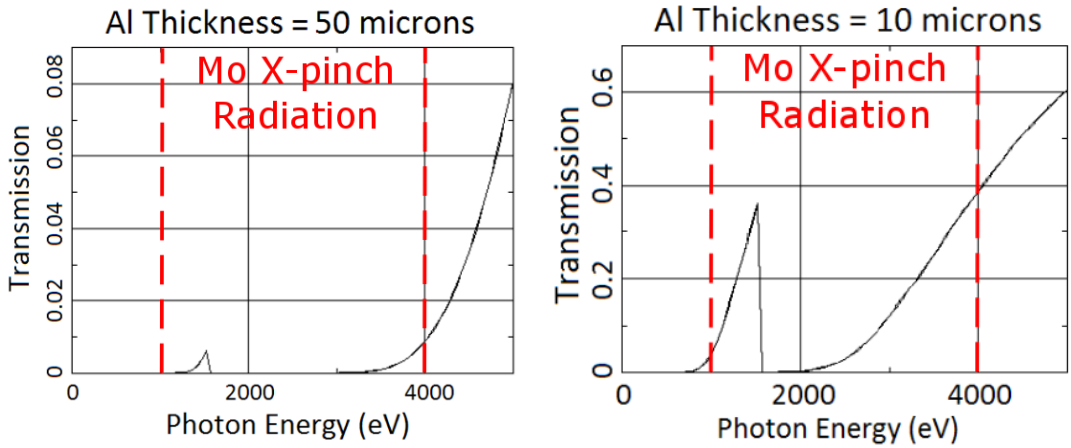

(a) (b)

Figure 4.2: X-ray transmission percentage through solid Al as a function of photon energy, data obtained from CXRO's online X-ray database. The increased transmission with decreased Al thickness from (a) 50 μm to (b) 10 μm is evident. The X-ray emission range of Mo-wire X-pinches is highlighted.

poses. The assumption then is that the resulting physical and magnetic field perturbations from side B in Fig. 4.3 (b) do not affect the development of the observed structure on side A at the time of the radiograph. The advantage of this compromise is that one can now use thicker foils for the liner and still obtain high-resolution radiography of side A as the X-rays are transmitted through only one layer. Comparing data with and without slits, we find similar small scale structure sizes for both, between 17 and 25 μm, meaning that the approximation concerning the impact of the slit evidently holds for our radiography measurements.

The hybrid X-pinches that were used, shown in Fig. 4.3 (a), consisted of two conical stainless steel electrodes with a 2 mm long wire connecting them. Both hybrid X-pinches and 4-wire X-pinches were used successfully in our experiments when positioned in return current posts on COBRA.

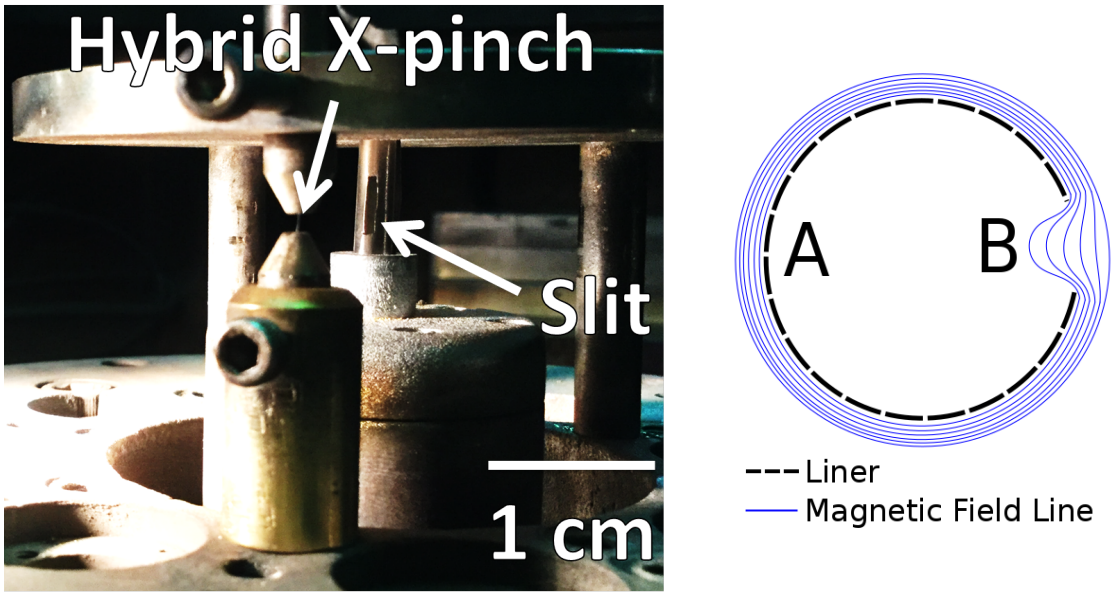

(a) Photo (b) Cross-section

Figure 4.3: (a) Photograph showing the liner with a slit cut in it and a hybrid X-pinch on the return current post. (b) Cross-sectional view of the liner illustrating the magnetic field line bending.

An important aspect of the radiography method described here is the combination of the Mo X-pinch with the specific filters. The X-pinch produces an intense 1-2 μm X-ray source over the $\approx$ 2.8 - 4.8 keV energy range only. Anything significantly below or above that range has a larger source size, reaching 10 - 100 μm.[43] With a 12.5 μm Ti filter, the transmission below 6 keV is substantial in the 2.8 - 4.8 keV window, matching the spectral region where the Mo X-pinch source size is smallest and very bright. Note that, if needed, one can change the source spectrum by changing the X-pinch wire material [41, 42].

In that same 2.8 - 4.8 keV energy range, the Ti filter also has a transmission-vs-wavelength curve that matches well with our Al foil transmission characteristics. If a different liner material is used, such as Cu, different filters must be used to better match the transmission wavelength range of the foil.

In our experiments, we have used 1, 2 and 3 X-pinches in parallel in the COBRA return current circuit using Mo wires that were 17-40 μm in diameter, depending on the experiment. The magnification factor, determined by the relative distances between detector, liner, and X-ray source for point-projection radiography, was 12-13 and was limited by the size of the experimental vacuum chamber rather than by X-pinch intensity or detector sensitivity.

4.2.2 Insulator Considerations

One possibility for adding a dielectric coating on a metal liner is a liquid dielectric that will flow over the whole liner, effectively covering the entire surface. This can also be used in conjunction with solid dielectrics placed outside the liquid as a solid insulator may provide better expansion inhibition compared to a liquid one, with the combination providing indirect physical contact between liner and solid insulator. Note that solid dielectrics can be designed to be in direct physical contact with the liner through, e.g., deposition. However, the solid dielectric tubes used here should not be expected to fully contact the liner, without any vacuum gaps, if one relies only on the liner's elasticity to expand against the insulator using the method described in Section 4.2.1. We have experimented with both liquid+solid and solid only insulators. However the focus of this Chapter, when discussing insulated liners, will be on solid only insulators. We used 50 and 75 μm thick Kapton tubes, obtained from Precision Products Group, and 100 μm thick Mylar tubes, obtained from Euclid Spiral Paper Tube Corp.

Another method to reduce the problem of gaps between liner and insulator

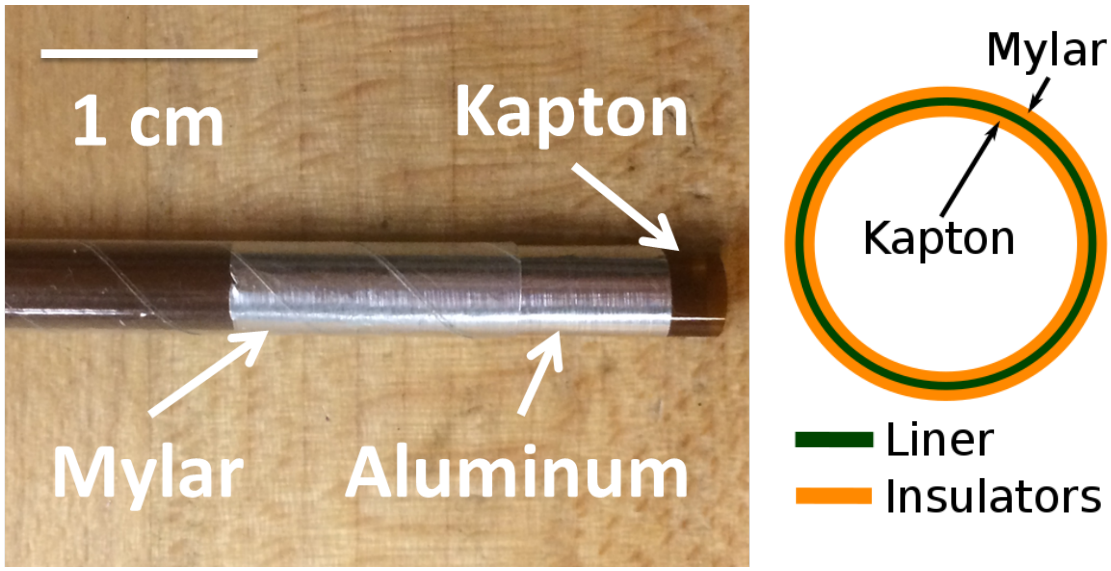

(a) Photo (b) Cross-section

Figure 4.4: (a) A photo of a liner "sandwiched" between two insulators. Here, the Kapton acts as the inner insulator and the Mylar as the outer insulator. In the picture, the Al foil has been axially extended from underneath the Mylar, and the Kapton from underneath the Al, to clearly show all three layers. (b) An axial cross-sectional schematic of the setup.

is by "sandwiching" the liner between two layers of solid insulators, as shown in Figure 4.4. To do this, we can take two flexible insulators whose gap between outer surface of the inner insulator and inner surface of the outer insulator is less than the thickness of the liner. As the insulators are plastic, they have some flexibility to stretch/compress to allow room for the foil. This sandwiching technique along with using thin liners is a simple, inexpensive method that enables radiography through the liner in experiments in which we inhibit expansion of the metal from both sides. Note that this method is effective to reduce gaps down to the μm scale. Foils may have inherent structure below that scale that creates gaps, such as ripples, that sandwiching would not eliminate.

Furthermore, we radiographed insulated liners using an insulator that only partially covered the liner axially. We could then simultaneously radiograph

insulated and non-insulated portions of the Al liner to make a direct comparison on the same shot, while also observing the processes taking place at the boundary between the two regions.

4.3 Results and Analysis

Choosing the right detector was critical to being able to observe the small scale features of interest here. We tried using both Carestream's DR50 film, which is advertised by the company as "an ultra-fine grain, very high contrast film", and Fujifilm's BAS-SR 2040 image plates, which are detectors commonly used in the medical field. The scanner used for the image plates was the Typhoon FLA 7000, scanning at 25 μm pixel size, a 650 nm wavelength and a photomultiplier tube (PMT) voltage setting of 500. The time between an experiment and scanning the image plate was no more than 10 minutes and exposure of the image plate to light in that period was practically nil. A result is shown in Fig. 4.5 for a 16 μm Al liner with a slit cut into it, as shown in Fig. 4.3 (a). The experiment had an image plate positioned immediately behind the film. We can see a region where the X-rays are absorbed by a single layer (lighter) and regions where they are absorbed by two layers (darker) in both detectors. The image plate shows the small-scale structure through a single liner thickness but, in spite of substantial effort with software contrast enhancement tools to show the structure, not through two. On the other hand, the DR50 film clearly shows features in both regions. Similar behavior was observed with the image plate in numerous experiments, both behind film and without any film in front of it. Placing no film in front is important as the film otherwise absorbs a significant amount of the 3 - 5 keV X-ray radiation that is responsible for the high resolution achieved with

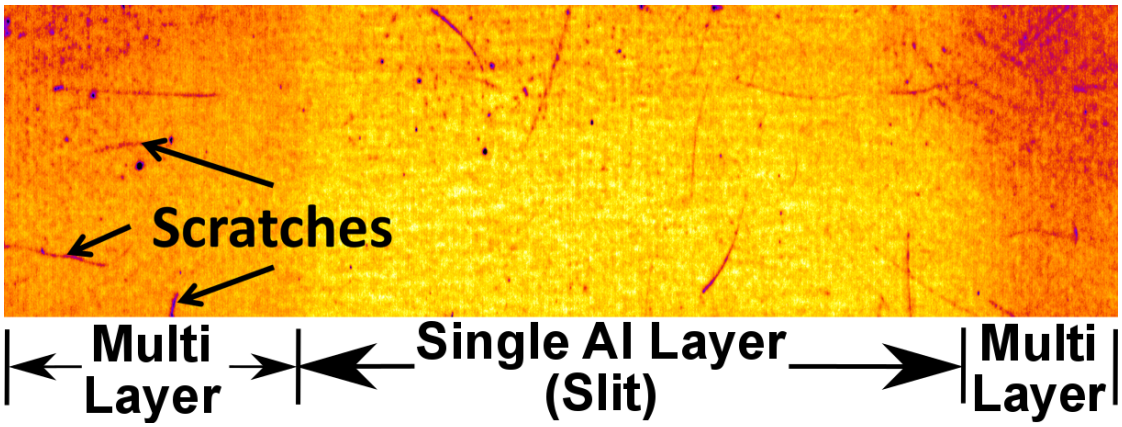

(a) Image Plate

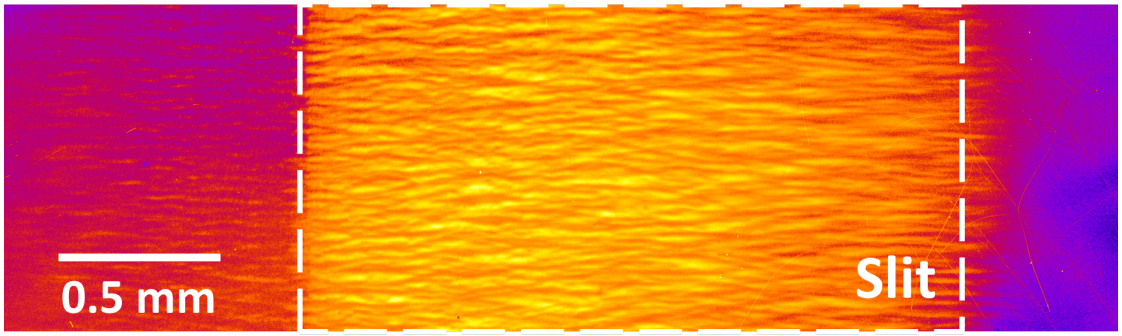

(b) Film

Figure 4.5: X-pinch radiographs of an Al liner with a slit cut into it, as described in Section 4.2.1, on (a) an image plate and (b) a DR50 film. The radiographs were taken at 105 ns in a 140 ns rise-time 1.1 MA peak current pulse. At that time the current was 0.85 MA. The white dashed lines in (b) are delimiting the area of the slit.

the X-pinch. For Cu, Ni, and Ti liners, out of 16 experiments, none showed any visible features using image plates with no film in front of them. Out of a similar number of experiments using film, roughly half the experiments displayed features. Cu, Ni, and Ti tended to have smaller feature sizes and/or smaller contrast compared to Al, which we believe accounts for the reduced fraction of experiments with visible features.

Comparing detectors, these results show that using film produces results with better resolution and contrast than using SR image plates. A summary

Table 4.1: Detector Comparison

Material	Film - Visible Features	Image Plate - Visible Features
Al (1 layer)	Yes	Yes
Al (2 layers)	Yes	No
Cu, Ni, Ti	Yes at 50% Occurrence	No

of this comparison is shown in Table 4.1. The smallest features observed on film were roughly 5 μm at the object. Hence, we estimate the resolution from using film with the magnification of 12-13 to be around 5 μm. We believe that the better results with film in our experiments is due to the image plates' being more sensitive to harder X-rays than the film. That matters because the source size of the X-pinch, as previously mentioned, increases for X-rays $>$ 5 keV to 10-100 μm. As the features of interest are 10-25 μm in size, the larger source size will cause a blurring of the structure on the image plates.

There is an important benefit of using the image plate positioned behind the film. In combination with signals from photoconducting diodes monitoring the soft X-ray intensity, the image plate exposure gives a good indication of the intensity of the X-pinch(es) on a particular shot, thereby providing guidance on how long to develop the film in order not to cause overexposure or underexposure. In our experiments, we have changed development time by up to 50% based upon this cueing.

For experiments with insulators, we found it necessary to protect the detectors and other diagnostics in the experiment from debris. Figure 4.6 (a) shows the typical damage from debris incurred by a protective window placed approximately 45 cm away from the load region. In one experiment out of about ten,

(a)

(b)

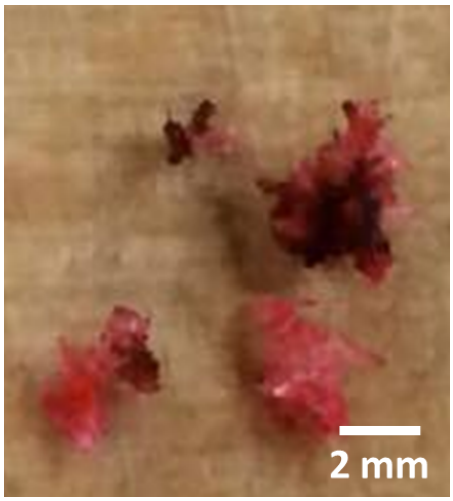

(c)

Figure 4.6: (a) A post-experiment picture of a protective window placed roughly 45 cm away from an insulated liner. (b) A piece of foam that was used to capture the debris to prevent the latter's vaporization upon impact. (c) A zoomed in picture of the debris extracted from a few locations in the foam catcher shown in (b) - curled solid black thin filaments enveloped by the red foam.

the window shattered. To learn the state of matter of the debris, we used foam to catch it. Note that foam is critical here as a harder surface, e.g. glass, can cause a high-velocity solid to vaporize upon impact, not to mention shattering the glass. We caught solid black thin filaments, as shown in Figs. 4.6 (b) and (c). Hence, at least a portion of the debris appears to be bits of solid insulator. Evidently not all of the insulator vaporized. Instead, it was turned into a solid

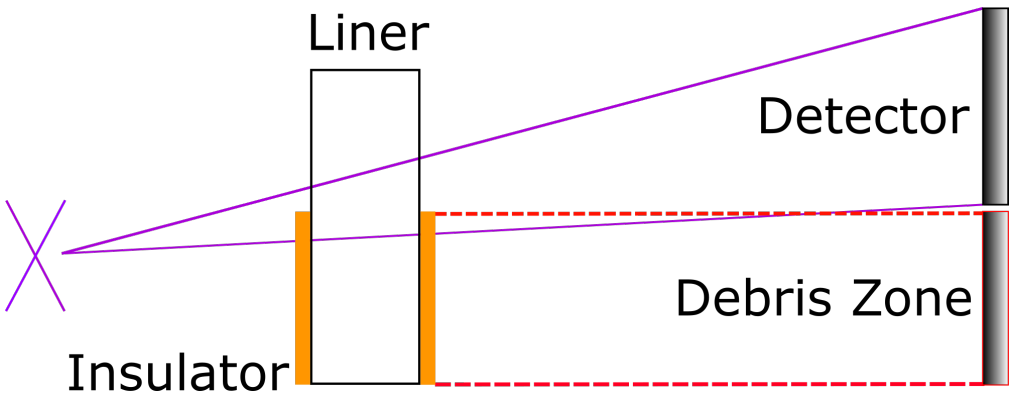

(a)

Figure 4.7: Sketch depicting a method that prevents damage caused to the radiography detector from the liner debris.

projectile by the foil explosion pressures propelling the insulator radially outward. We estimate delivering about three orders of magnitude more energy to the load than would be needed to vaporize the insulator. While only a small fraction of the energy at the load will go into heating the insulator, the presence of solid insulator at the end of an experiment might not be expected from this energy estimate comparison.

To protect the X-ray sensitive detectors from the debris, we found that using a 250 μm thick mylar protector was not sufficient. The debris pierced straight through the protector and the Ti filter and lodged itself in the DR50 film. Finding that the debris moves nearly perpendicular to the axis, detector integrity in future experiments can be assured with reasonable confidence by angling the line-of-sight, as shown in Fig. 4.7.

Figure 4.8 shows results from an experiment with two outer solid insulator layers only partially covering the liner axially. We can clearly see the two layers of insulator and their edges. There are vacuum gaps visible between insulators and between insulator and liner. This shows that the liner's expansion is not

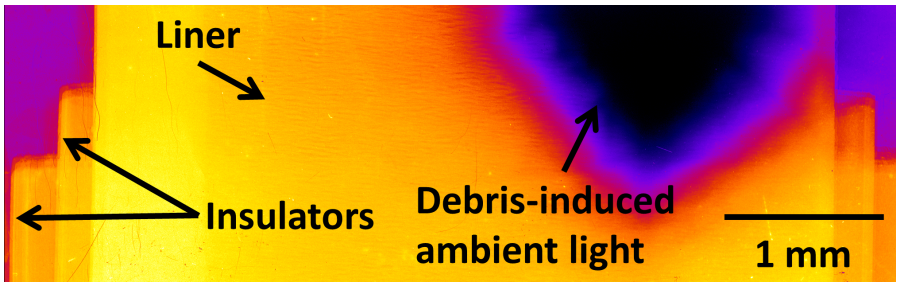

(a)

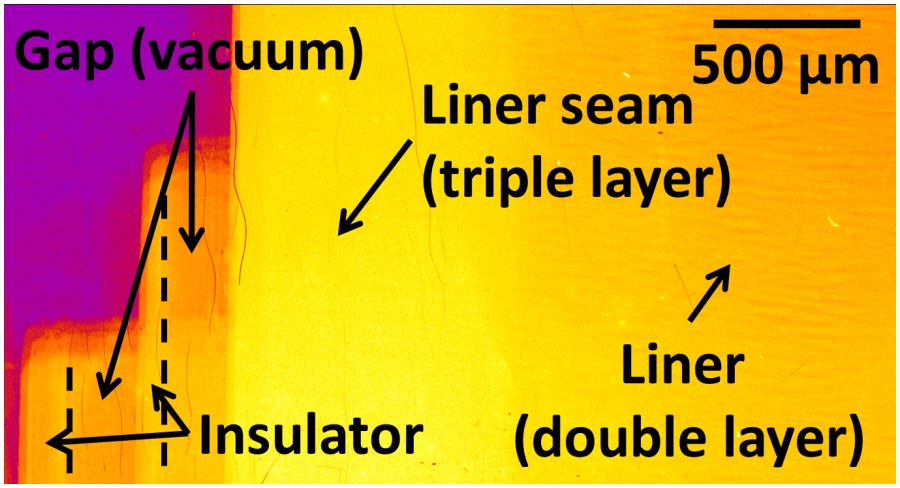

(b)

Figure 4.8: (a) Radiograph of an Al liner with 2 layers of solid insulator surrounding it. The insulators are only partly covering the liner axially. (b) A zoomed-in view of the insulators. In the case shown, the vacuum gaps between solid insulators and between the inner insulator and the liner, which can easily be filled with a liquid dielectric, if desired, is pointed out. The blurry edges are due to multiple X-pinch soft X-ray bursts, all within 20 ns of each other in a 110 ns rise-time pulse, that create multiple images overlaying one another.

inhibited by the insulator until $\approx$ 200 - 300 μm expansion occurs in this setup. However, the gap(s) can be filled by a liquid dielectric to inhibit expansion. Note that the blurry features at the edges of the insulator are a result of multiple bursts of the X-pinch in this experiment. The dark spot covering a large portion of the image is a consequence of the debris tearing through the mylar and Ti filter, as explained above, and exposing a portion of the film to the ambient light.

This Chapter presented a method to effectively radiograph thin metallic liners with and without expansion inhibition using the X-pinch as the X-ray source. X-pinch radiation enables radiography through both insulated and non-insulated liners, and may be very useful for better understanding the physics involved in the early stages of liner experiments. Experiments using this diagnostic to investigate the development of μm scale features in metal liners will be discussed in the following Chapter.

CHAPTER 5

INVESTIGATION OF MICROMETER SCALE FEATURES

5.1 Motivation

Peterson *et al.* observed μm scale features appearing on the surface of the liner in the MagLIF experiments and attributed these to the non-ionized matter electrothermal instability [33, 34]. On the basis of simulations, applying a thick dielectric coating over the liner was proposed to mitigate the instability[54]. Awe *et al.* then used 6.151 keV monochromatic radiography on subsequent MagLIF experiments to observe a stabilizing effect when applying such a coating in metallic liner implosions [55].

In the above liner experiments on Z, the research focused more on mitigating the structure and less on testing the validity of the proposed mechanisms. Some experimental work has also been done with the main objective being the investigation of μm scale structures in both flat foils[56] and solid rods[51]. For example, Awe *et al.* used high-resolution optical self-emission to observe the development of μm scale features on the surface of solid Al rods subject to the Zebra 1 MA pulsed power driver [51] and compared these with the electrothermal instability hypothesis.

The work presented in this Chapter was motivated by a desire to better understand the μm scale features that develop as described above by examining the liner's mass distribution in cylindrical metal foil liner experiments. The Chapter is organized as follows. Section 5.2 briefly discusses experimental arrangements. Section 5.3.1 shows results of areal density measurements for Al

foil liners and compares these with computational model predictions using the PERSEUS code [57, 58]. Section 5.3.2 discusses measurements of the density perturbations' spatial size for Al, Ni, Cu, and Ti and compares these with analytic estimates based on the electrothermal instability [50]. Section 5.3.3 delves into experiments with dielectric coatings and the influence of expansion inhibition on feature size. Section 5.3.4 analyzes the expansion of the solid dielectrics in those expansion inhibited experiments. Section 5.3.5 examines experimental results regarding the effect of ingrained structure in Al foil on these μm scale features and offers possible explanations.

5.2 Experimental Configuration

In this section, we briefly present the experimental configurations used for our investigations of the electrothermal and electrochoric instabilities via high-resolution X-pinch X-ray radiography, details of which were described in Chapter 4 and have been published.[59]

The liners used were wrapped from initially flat foil and were 4.2 mm in diameter and 11 mm in height. We used four different materials with the following thicknesses: 16 μm Al, 7.5 μm Ni, 7 μm Cu, and 10 μm Ti. The liners were mass-matched to within about 30 $\%$ altogether (Al and Ti matched to within 5 $\%$; Cu and Ni matched to about 5$\%$) and were sufficiently thin that the current penetrated their thickness within the first 25 $\%$ of the current pulse rise time.

To inhibit the liner's radial expansion, we used 50 - 100 μm solid dielectric tubes that were typically 4 - 5 mm long and only partly covering the liner axially so that we could observe simultaneously regions of expanded and non-

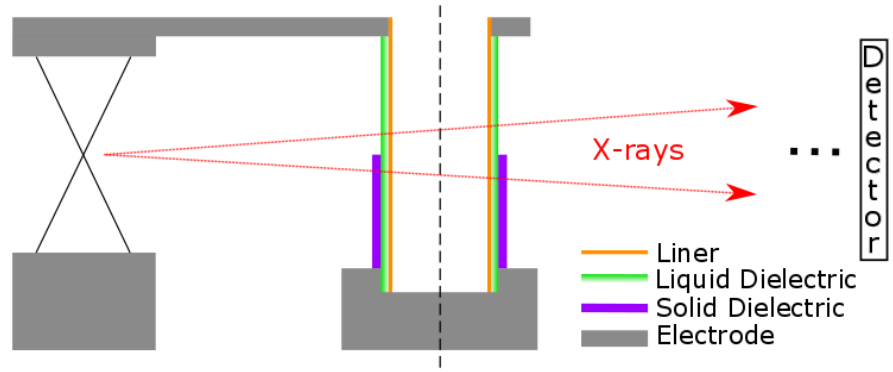

(a)

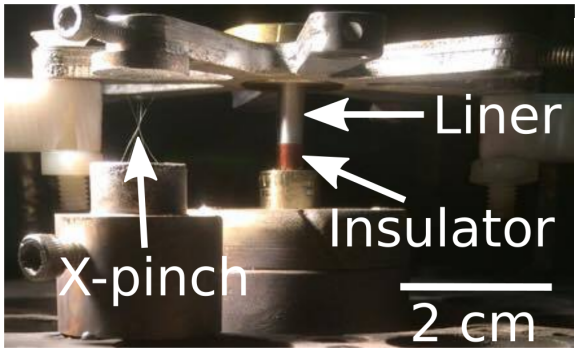

(b)

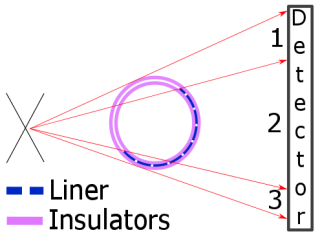

(c)

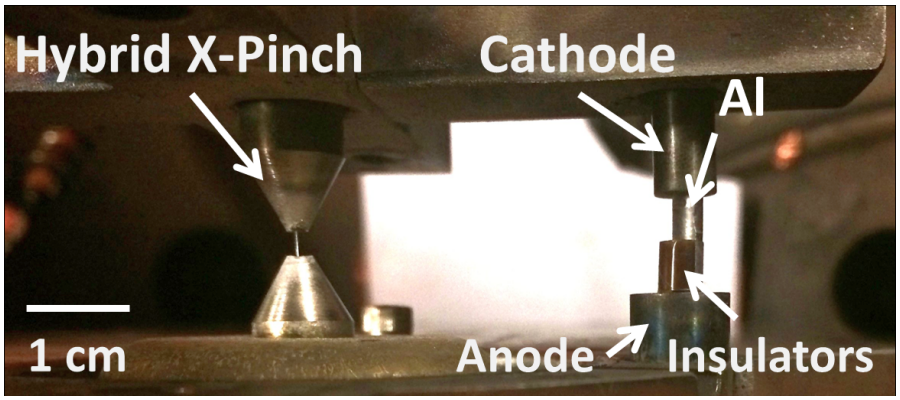

(d)

Figure 5.1: (a) Schematic and (b) side view of setup #1. The load in the center is made of a metallic liner covered axially with a combination of solid and liquid dielectrics on the liner's outer surface. There is a 4-wire 25 μm Mo X-pinch positioned in place of one of the return current posts to act as the radiography X-ray source. The second return current post is positioned radially farther out than the X-pinch in order to increase its relative current path inductance. The image magnification factor is ~ 12. (c) An axial cross-sectional schematic and (d) a photo of setup #2 are shown. It is similar except that the foil here does not extend azimuthally more than 180° and solid insulators are on both sides of the foil, Kapton on the inside and Mylar on the outside.

expanded liner, as described in the previous Chapter. In setup #1, shown in Fig. 5.1 (a), we applied a liquid dielectric coating, Invoil 704 diffusion pump oil, over the entire outer surface of the liner and let the wrapped foil expand against the solid dielectric tube made of Mylar or Kapton. This inhibited the outward expansion of the liner during the current pulse. In setup #2, shown in Figs. 5.1 (b) and (c), we "sandwiched" a foil that spanned no more than 180° azimuthally between two dielectric tubes. The fit was such that there were no gaps between liner and dielectric layers larger than about 10 μm, ensuring that expansion beyond that scale was inhibited from both sides of the liner.

5.3 Experimental Results and Analysis

5.3.1 Areal Density Measurements

We started by performing radiographic areal density measurements of the 16 μm thick Al liners that had no dielectric on them. Results of one such experiment are shown in Fig. 5.2 (a). The color scheme in the image is artificial and has been chosen to enhance the region relevant to the single layer results. The density values are determined using a step wedge with 1 μm thick overlaying Al foil steps spanning 1 μm to 16 μm. Using the solid Al density of 2700 mg/cm^3, these steps are then converted into units of mg/cm^2 (the 16 μm thick initial foil equaling 4.32 mg/cm^2) to facilitate comparison with other materials in later work. A zoomed-in picture of box A in the non-overlapping region is shown in Fig. 5.2 (b). A setup sketch for the data presented is shown in Fig. 5.2 (c).

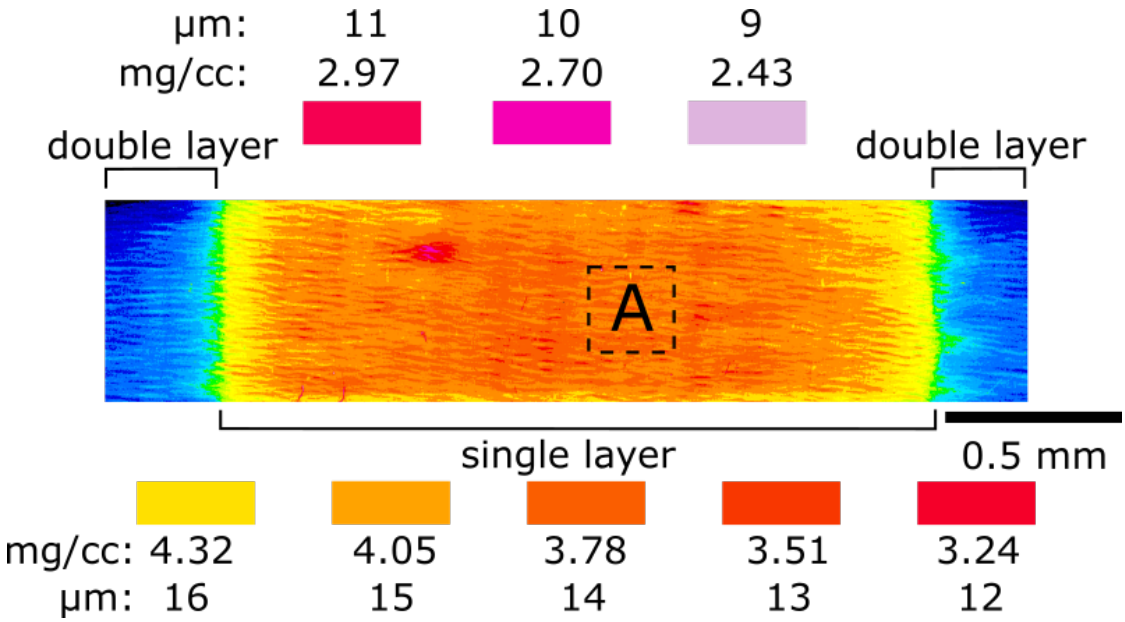

(a)

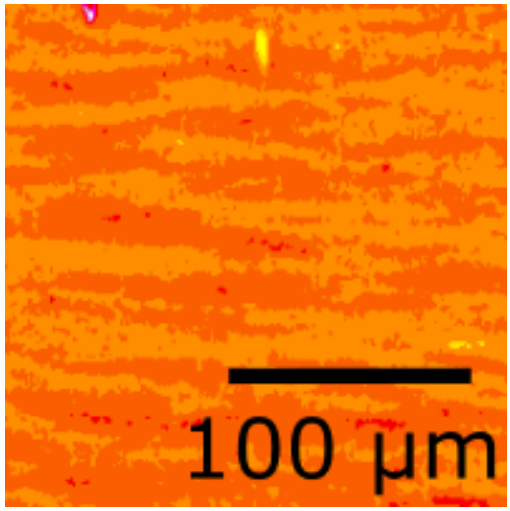

(b)

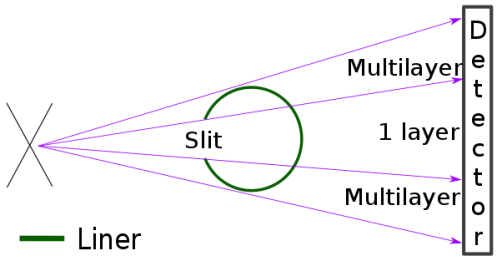

(c)

Figure 5.2: (a) Result from X-pinch radiography of an Al liner with a slit. A step wedge having 1 μm steps, shown in both units of μm and mg/cm^2, was used to obtain areal density distribution information. (b) Zoomed-in picture of box A, which is in the slit region of the image. (c) A sketch of the radiography setup for a liner with a slit.

The data is taken at about 65 ns into a 1.2 MA, 100 ns rise-time pulse. The current density is of order 10^{12} A/m^2. From the data shown, we find a local density variation of up to 40% in the single layer. Differences in density variation in different areas are at least partly attributed to random initial seeding that is present due to the foil manufacturing process. The average areal density in the single layer is about 4.05 mg/cm^2, or the equivalent of 15 μm worth of Al solid foil, versus the initial foil thickness of 16 μm. We believe that the 1 μm difference is an error caused largely by stray background radiation. An imperfect film development process may also have introduced some local measurement error. Including this error component, we estimate an areal density variation of up to $35 - 40\%$ using the image in Fig. 5.2 (a). Similar variation was found in other experiments with and without a slit cut into the liner.

We measured the structure's spatial scale from experiments by averaging measurements from 10 different locations in each radiograph. Using the averages from all of our Al liner data, we obtained 21 $\pm$ 4 μm, as shown in Table 5.1.

We used the PERSEUS 3D extended MHD code [57, 58], in which improved Al Equation-of-State (EOS)[60, 61] and low temperature resistivity [62, 63] models were recently implemented, to simulate a similar experiment. Starting with a square slab, 0.75 mm long along the x and y axes and 24 μm thick along the z axis, we ran a similar current pulse to that in the experiments along the x direction. The discontinuous Galerkin method used for the simulation employed a cell size of 7.8 μm with a cubic basis. In the following discussion, density mapping will be shown at various surface layers. The density values are those averaged over the cell thickness at the given surface.

A surface layer in the x-y plane, 5 μm away from the slab's initial outer surface in the negative z-direction, is shown in Fig. 5.3 (a). An edge-on view in the x-z plane is shown in Fig. 5.3 (b). Both images are taken at 60 ns into the pulse. At that time, the average current per cross-sectional area in the simulation is estimated to be within 10 $\%$ of that in the experiment of Fig. 5.2. The electromagnetic wave driving the simulation diffuses into the matter from the right side to the left in Fig. 5.3 (b).

Areal density information provided by a radiograph is different from density information in a given surface layer. Generally, variation in areal density will be affected most strongly by the surface layers where the density varies by the largest order of magnitude. Since Fig. 5.3 (a) looks at one such surface layer, we can compare that with the radiograph in Fig. 5.2 (a). In the layer shown in Fig. 5.3 (a), the length-to-width ratio of the features is comparable with that of the radiograph. We also observe that the high density structure shown in the liner expands largely towards the left in Fig. 5.3 (b). This corresponds to inward expansion in the context of a liner, and matches very well with experimental results that will be presented in section 5.3.3. In Fig. 5.3 (a) and (b), we also see that the feature sizes in the direction of the current measure about 15-20 μm, matching the experimental results given above. Integrating the density through the liner in the z-direction in Fig. 5.3 (b), as would be done by our radiographs, we obtain a local areal density variation in the slab of up to 35 $\%$. This matches with the experimental values from Fig. 5.2. We would like to point out that this variation is very sensitive to the EOS used in the model. The EOS sensitivity was noted in prior simulations using the MHD code, GORGON [6].

Overall, we found matching areal density variation, feature size in the cur-

rent direction, aspect ratio, and "inward" expansion of the slab. Hence, all our experimental results that can be compared with the computational results from PERSEUS give good agreement. Consequently, the regions in the liner that are strongly dependent on the improved physics models in PERSEUS, namely the EOS and low temperature resivity models, appear to be reasonably well simulated. We can then use PERSEUS to look at certain information that cannot be obtained clearly and unambiguously in experiments. For example, one interesting such result is shown in Fig. 5.3 (c). This is a surface layer displaying density information that is taken at 80 ns and 80 μm away from the slab's initial outer surface in the positive z-direction. We observe larger-scale features that are aligned roughly along the direction of the current as well as smaller-scale features that are aligned perpendicular to it. The simultaneous presence of such orthogonally aligned features was experimentally observed by Awe *et al.*[51] The computational result presented now additionally shows that not only do the parallel and perpendicular features exist simultaneously, they can exist within the same surface layer. This phenomenon occurs only in layers within a very narrow region. This will be analyzed in detail in future work.

5.3.2 Electrothermal Instability

To determine the factors affecting the size of the features, we tested the effect of material variation and the effect of expansion inhibition. The growth rate, Γ, for the proposed condensed matter electrothermal instability is, as shown in Chapter 3, given by[50, 33]

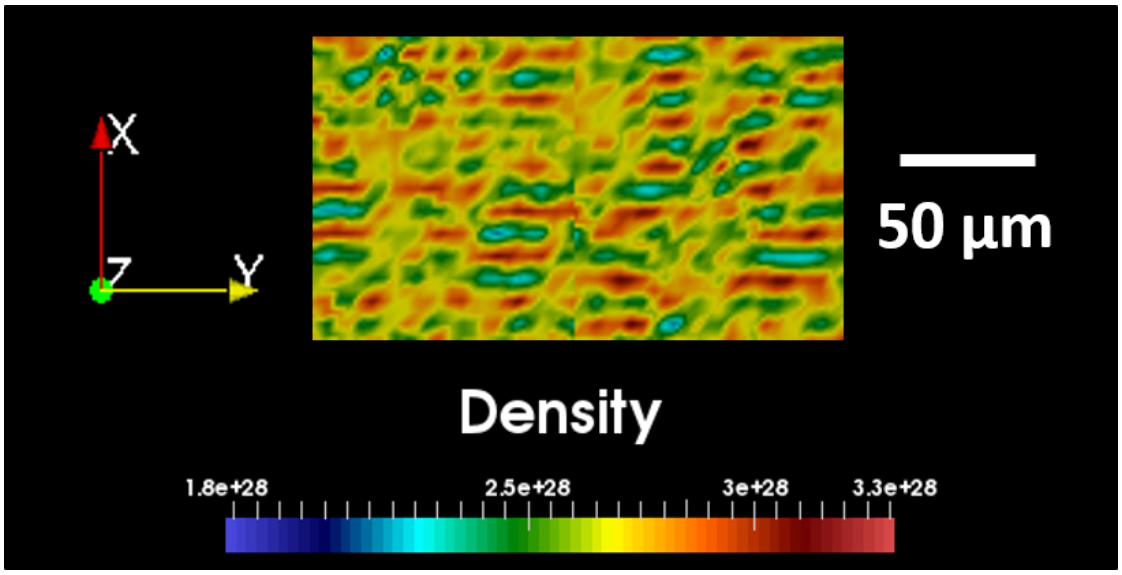

(a)

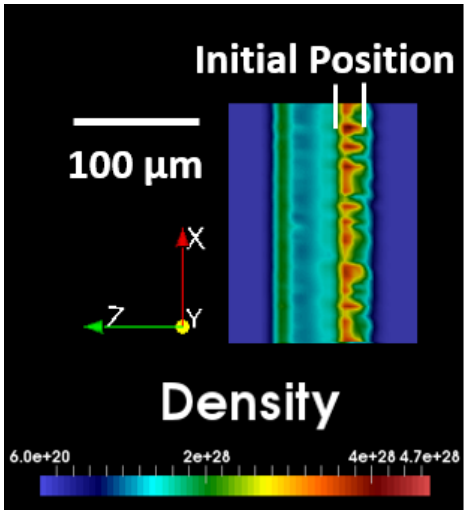

(b)

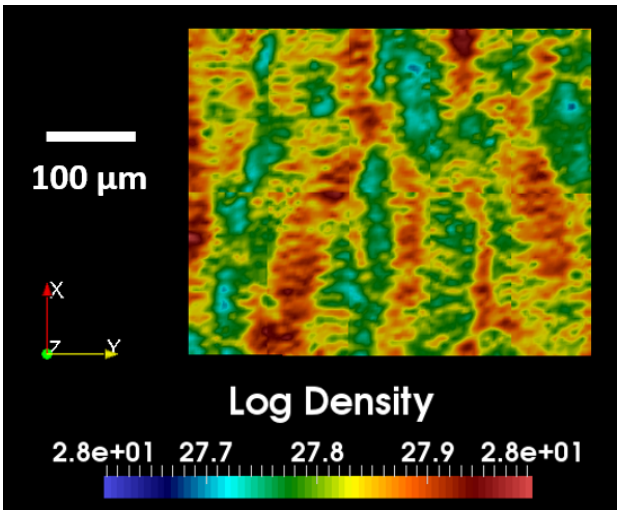

(c)

Figure 5.3: 3D simulation results of a 0.75x0.75 mm square slab 24 μm thick that is being driven by a similar current pulse to that in the experiments along the x direction. (a) Surface plot observing density taken at 60 ns in the x-y plane, 5 μm away from the slab's initial outer surface in the negative z-direction. (b) An edge-on-view of the density at 60 ns in the x-z plane. The initial slab position is highlighted. The pulse is driven in the x-direction from the right side ("outer" side). Integrating along z in (b), we get an areal density variation of up to 35 %. The horizontal features' average size in the x direction is about 15-20 μm. (c) Surface plot observing density taken at 80 ns in the x-y plane, 80 μm away from the slab's initial outer surface in the positive z-direction.

$$\Gamma = \frac{1}{\rho c_\nu}[\frac{\partial \eta}{\partial T} J_z^2 - k_z^2 \kappa] \tag{5.1}$$

where ρ is the material density, c_ν is the specific heat, η is the material electrical resistivity, T is the temperature, J_z is the current density, k_z is the perturbation wave number, and κ is the thermal conductivity. Equating the growth to zero, we find a threshold wavelength given by

$$\lambda_{min} = \frac{2\pi}{J_z}\sqrt{\frac{\kappa}{\frac{\partial \eta}{\partial T}}} \tag{5.2}$$

This equation accounts neither for density variation nor for any non-linear effects, both of which are important in our measurements. However, as was shown in Chapter 3, when liner motion and material density variation are accounted for, the growth rate peaks within an order of magnitude of λ_{min} for a material in liquid state.[50] Equation 5.2 has been shown to be an appropriate estimate when compared with experimental wire explosion results [50] and with HYDRA simulation results for Al rods [34]. In this Chapter, we use Eq. 5.2 to compare the predicted feature sizes of our four materials. We note that there may be differences between theory/simulation and experiment due to impurities in the materials we used. Impurities could create small non-uniformities in the liner and cause some material property variation. Before surface adsorption of ambient gases and surface changes, such as buildup of aluminum oxide, the Al was 98+$\%$ pure, Ti was 99.6+$\%$ pure, and Cu and Ni were 99.9 $\%$ pure.

In our experiments, the liner geometry for the various materials was kept constant except for the liner thickness as described in Section 5.2. To estimate wavelengths for each material, we use values in Eq. 5.2 that describe the conditions at melt, just on the solid side of the phase transition, and call this λ_{sm}.

We will briefly discuss results that use parameters from the liquid side of the phase transition as well, which we call λ_{lm}. However, from current integral estimates[64], the time difference between melt and vaporization, when non-linear effects and motion would become important and Eq. 5.2 would no longer be valid, is only a few ns. This would amount to very small growth, on the order of 1 e-folding, given the growth rates, and should not significantly affect the observed wavelength. Tabulated thermal conductivity values during melt at the solid phase [47] and the approximately constant $\frac{\partial \eta}{\partial T}$ [49] in solid state were used and are shown in Table 5.1. To determine J_z at the time of melt, we used the current integral $\int_{t_{room}}^{tmelt} J_z^2 dt$. Determining the current integral value for each material analytically, we could then determine t_{melt} and consequently $J_z(t_{melt})$. For the analytic calculations, we used tabulated specific heat values [47] and the same resistivity values as mentioned above [49]. To verify the computed current integral values for our four materials, we double-checked these with known Al and Cu tabulated values [64] as a proxy and found agreement within 5-10 $\%$, which leads to a current density variation of less than 10 $\%$.

Sample experimental results are shown for each material in Fig. 5.4. To determine the experimental feature size in Table 5.1, we took the averages from all our experiments for the corresponding materials. For the data presented, the measurements were taken between 60 and 80 $\%$ of the peak current time from a 1-1.2 MA 100-140 ns rise time current pulse. The smallest observable feature size was typically around 10 μm. There were a number of experiments in the case of Cu, Ni and Ti where features were not visible even though there was a good X-pinch X-ray burst [41, 42]. We believe that this is due to the features' being smaller than our resolution and/or not having enough areal density variation for our detector. Therefore, for those materials we have added "*" to the values

given to indicate that the average wavelength from experiments, λ_{exp}, might be less than those measured values.

As expected, λ_{exp} in all cases is noticeably larger than λ_{sm}. The latter, we point out again, is only representative of a minimum instability threshold value. The order of increasing feature size for λ_{exp} neither strongly agrees nor disagrees with that of λ_{sm}, partly due to the large variation of the feature sizes. A main takeaway corroborated by λ_{exp} and λ_{sm} may be that Al has the largest features and Ti the smallest. We also compared the experimental wavelength order with that of λ_{lm}. The order of increasing λ_{lm} goes as Cu, Ni, Ti, Al. Hence, the orders once again do not match. As mentioned before, that is not surprising given the small amount of growth predicted in that phase.

To test the electrothermal instability hypothesis further, one may use a different pulse shape so that the material is in the liquid phase for a longer time before vaporization. This will allow more instability growth in that phase. If this instability is indeed responsible for the structure, one may then expect a different order of feature sizes which may match better with λ_{lm}.

At the time of measurement, we estimate from a current integral argument that part of the liner is vaporized, i.e., undergoing significant changes in density. The following section will discuss possible effects once vaporization occurs.

5.3.3 Electrochoric Instability

To investigate the importance of the electrochoric instability in our experiments, we separately inhibited outer and outer+inner expansion of 16 μm thick Al lin-

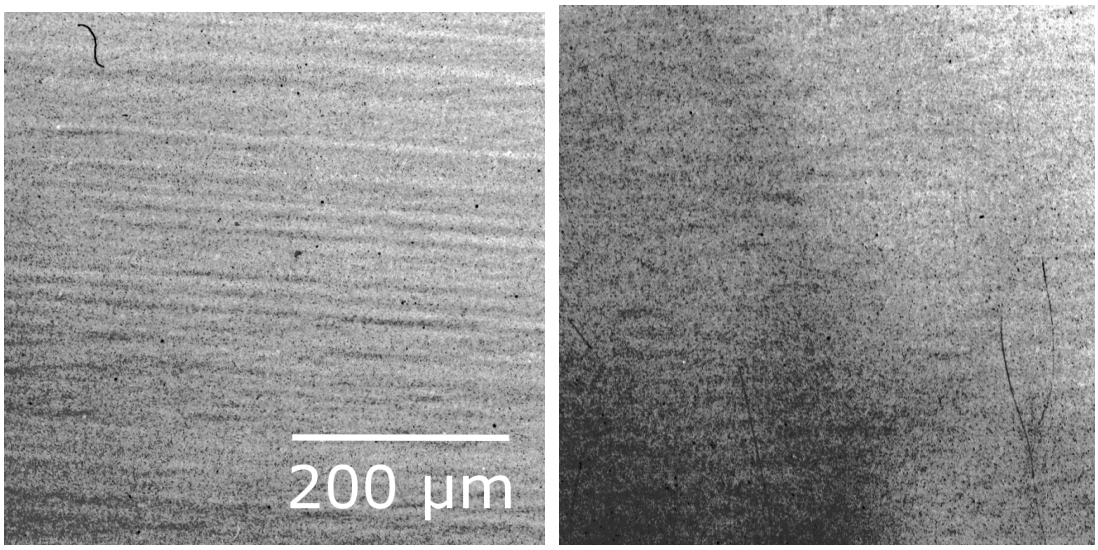

(a) Al - 16 μm

(b) Ni - 7.5 μm

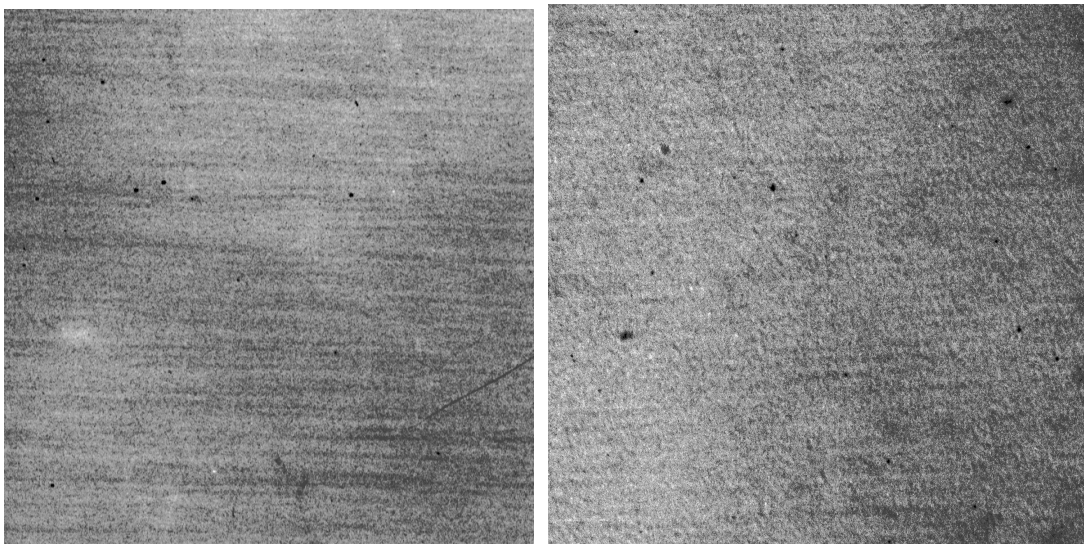

(c) Cu - 7 μm

(d) Ti - 10 μm

Figure 5.4: Radiographs of liners made of (a) 16 μm Al, (b) 7.5 μm Ni, (c) 7 μm Cu and (d) 10 μm Ti foil.

ers. We inhibited outer expansion only via setup 1, as described earlier, and used a 1.1 MA, 120 ns rise time pulse. We inhibited expansion from both sides of the liner/foil via setup 2 and used an estimated 350 kA, 150 ns rise time pulse [4]. Figure 5.5 (a), taken at 85 ns of the 120 ns pulse and with an axial profile plot in (b), shows that inhibiting outer expansion alone does not affect the wavelength nor the amplitude variation significantly. There is some overall in-

Table 5.1: Feature Size Comparison

	κ_{sm} $[\frac{W}{m*K}]$	$\frac{\partial \eta}{\partial T}_s$ $[\frac{n\Omega}{K}]$	J_z $[\frac{TA}{m^2}]$	λ_{sm} [μm]	λ_{exp} [μm]
Al	211	0.128	1.77	4.6	21 ± 4
Ni	70	0.391	1.97	1.35	$^*19 \pm 3$
Cu	330	0.087	3.15	3.9	$^*16 \pm 5$
Ti	31	1.2	8.89	1.14	$^*11 \pm 2$

creased absorption due to the added material (the insulator) but the amplitude of the features, i.e., areal density variation, does not noticeably change. Furthermore, the feature size is similar to that in non-insulated Al liner experiments. Since the current quickly diffuses throughout the liner, it can expand inward. This possibility, that expansion can still occur, evidently minimizes the effect of the outer insulator on the features.

On the other hand, inhibiting expansion on both sides of a cylindrical foil produces a significant effect, as shown in Fig. 5.6 (a). For clarity, Fig. 5.6 (b) shows a labeled representation of the data shown in (a). The data in that experiment is a result of two X-pinch bursts, at 85 and 135 ns, in the 150 ns pulse. For the profile plot shown in Fig. 5.6 (c), comparing the coated with the non-coated sections shown, the dominant feature wavelength in the former is reduced by 10 - 15 $\%$ and the average contrast is smaller by approximately 50 $\%$. Additionally, we can see significant cylindrical foil radial expansion, around 100 μm, in Fig. 5.6 (a). A schematic of this expansion is highlighted in Fig. 5.6 (b). Hence, liner expansion appears correlated with strong feature amplification, a result that is consistent with the electrochoric amplification hypothesis and the influence of density-vs-resistivity on the μm scale structure in general.

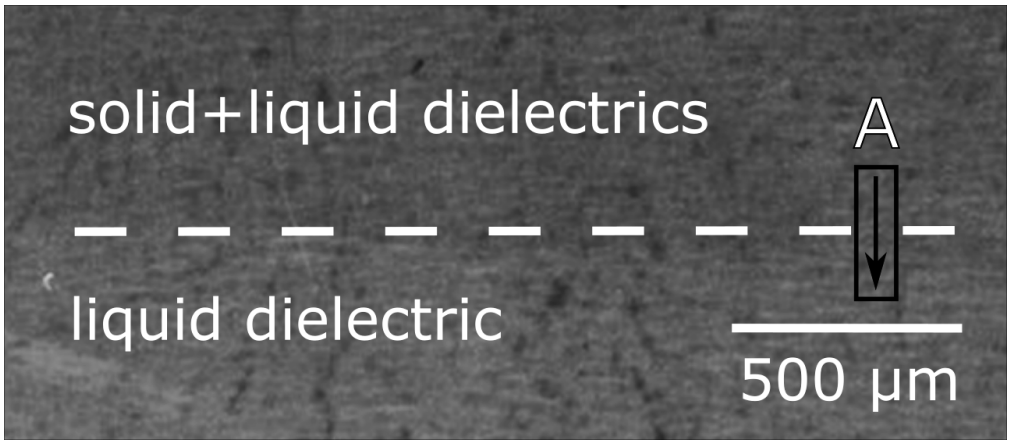

(a)

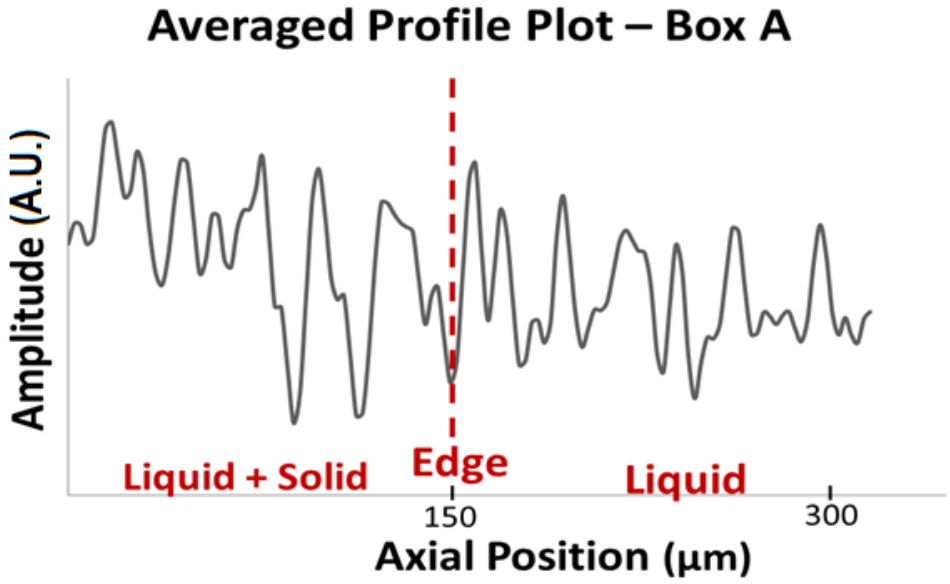

(b)

Figure 5.5: (a) Radiograph of an Al liner fully covered in liquid dielectric and then partly surrounded by two layers of solid dielectric on its outside surface. (b) Average profile plot of box A in (a), taken vertically downwards.

An analytic formula for instability growth that incorporates the dependence of resistivity on density, a key element for the electrochoric instability, has been previously derived.[50] However we do not have quantitative values for that resistivity-density dependence and hence cannot compare our experimental results with predictions.

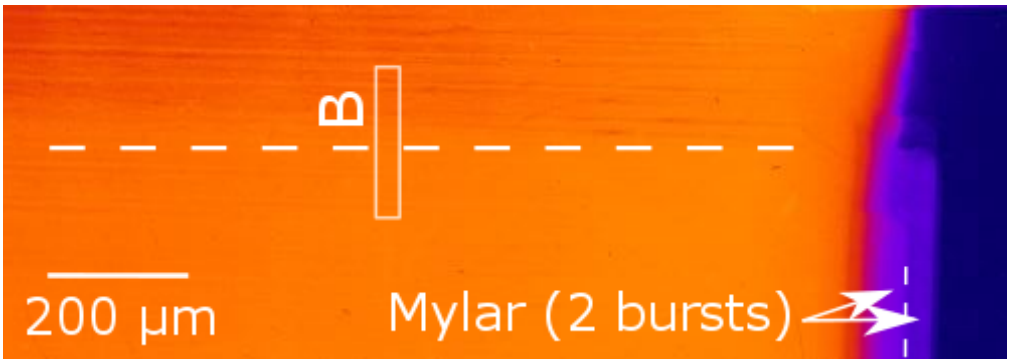

(a)

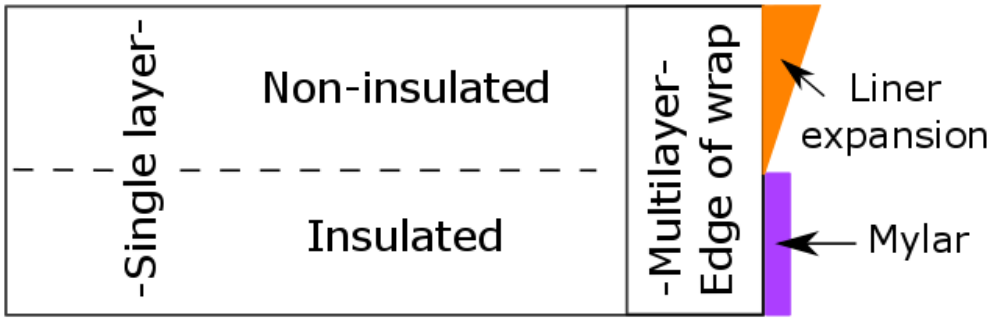

(b)

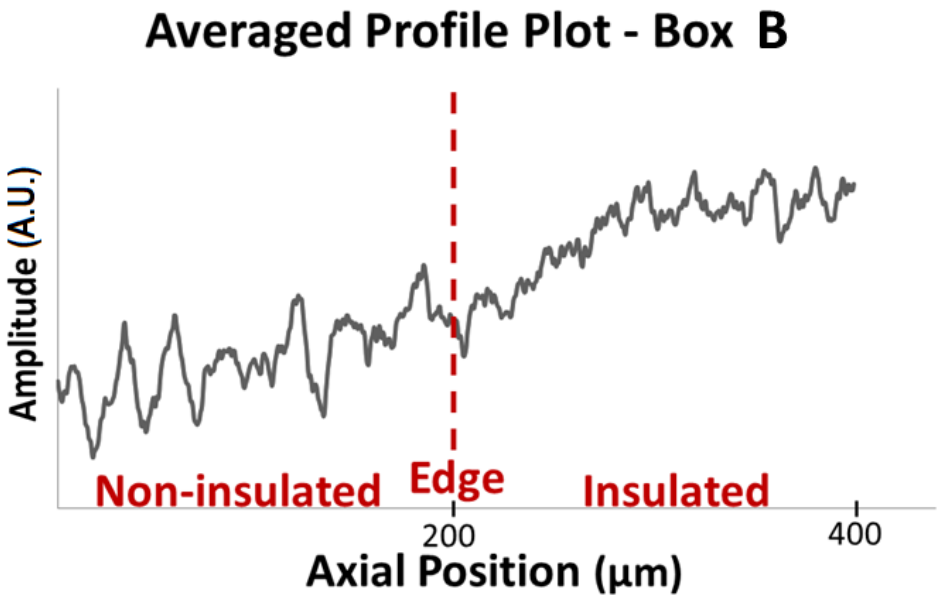

(c)

Figure 5.6: (a) Radiograph of a partly wrapped foil sandwiched between two layers of solid dielectric, one on each side of the foil, as shown in Fig. 5.1. (b) A visualization of that result for clarification purposes. (c) Average profile plot of box B in (a), taken vertically downwards.

5.3.4 Dielectric Expansion

In our experiments that inhibited expansion from both sides of the solid Al liner (setup 2), the outer mylar insulator expanded from its initial 100 μm thickness to between 130 and 190 μm at a time of measurement that was typically 100 $\pm$ 20 ns. As an example for setup 2 experimental results, refer to Fig. 5.6 (a). The image is produced by two X-pinch bursts, separated 50 ns from one another, so the insulator thicknesses at the times of the two bursts are difficult to tell with certainty. However, we estimate one to be 130 μm and the other to be 150 μm. We do not have a measurement for the solid insulator thickness from setup 1 as the regions with solid and liquid dielectrics were hard to distinguish. However, when only a solid outer dielectric was employed (setup 1 without a liquid dielectric in between liner and solid insulator), this typically resulted in a 100-200 μm gap between Al and dielectric in the radiographs and we did not measure insulator expansion above 5 - 10 μm. This relative lack of expansion suggests that radiation alone, up to the time of observation, did not heat the insulator sufficiently to lead to expansion.

The two setups used different loads, which changed the axial cross-sectional mass by more than a factor of 2, and different current drivers, the maximum current of which varied by a factor of $>$2. These introduce problems in the comparison of the results. However, comparing the total ohmic heating per cross-sectional area up to the time of measurement via a $\int J^2 dt$ proxy, the liners in the two setups are heated to within 10% of each other. Hence, in our experiments using the two different setups, the differing amounts of measured expansion suggest that dielectric heating and expansion is impacted more significantly by direct contact heating, such as conduction, than by radiation heating or ioniza-

tion.

5.3.5 Pattern Seeding

A final effect we tested was seeding the instability. Our Al foil, without any current flowing through it, is shown in Fig. 5.7. A sample photo is shown in (a), a microscope picture in (b), and a radiograph in (c). The microscope image displays surface features that are about 60 - 80 μm in size while the radiograph displays areal mass density variation at a feature scale of about 30 μm. Note that the microscope was at its resolution limit, and so the actual surface features may also have been about 30 μm in size.

To test whether this non-uniformity had an effect on the striations, we oriented the grooves of the structure perpendicular to the current flow direction in one case, which we will refer to as "seeded," and parallel to it in another, which we will refer to as "non-seeded." The results, displayed in Fig. 5.8, show a clear difference. First, in the seeded case we see full azimuthal correlation of the structures, as shown in Figs. 5.8 (a) and (e), whereas in the non-seeded case we find somewhat curving azimuthally-limited features, as shown in Figs. 5.8 (c) and (f). We will refer to the latter structure as "interspersed". Second, we can see ripples with larger amplitude and wavelength at the surface of the liner for the seeded case, as illustrated in Figs. 5.8 (b) and (d). Third, seeded experiments display a higher contrast, i.e., areal density variation, for the same feature size, as shown in Fig. 5.8 (g).

These three differences between seeded and non-seeded experiments were observed consistently. To explain the first observation, note that the proposed

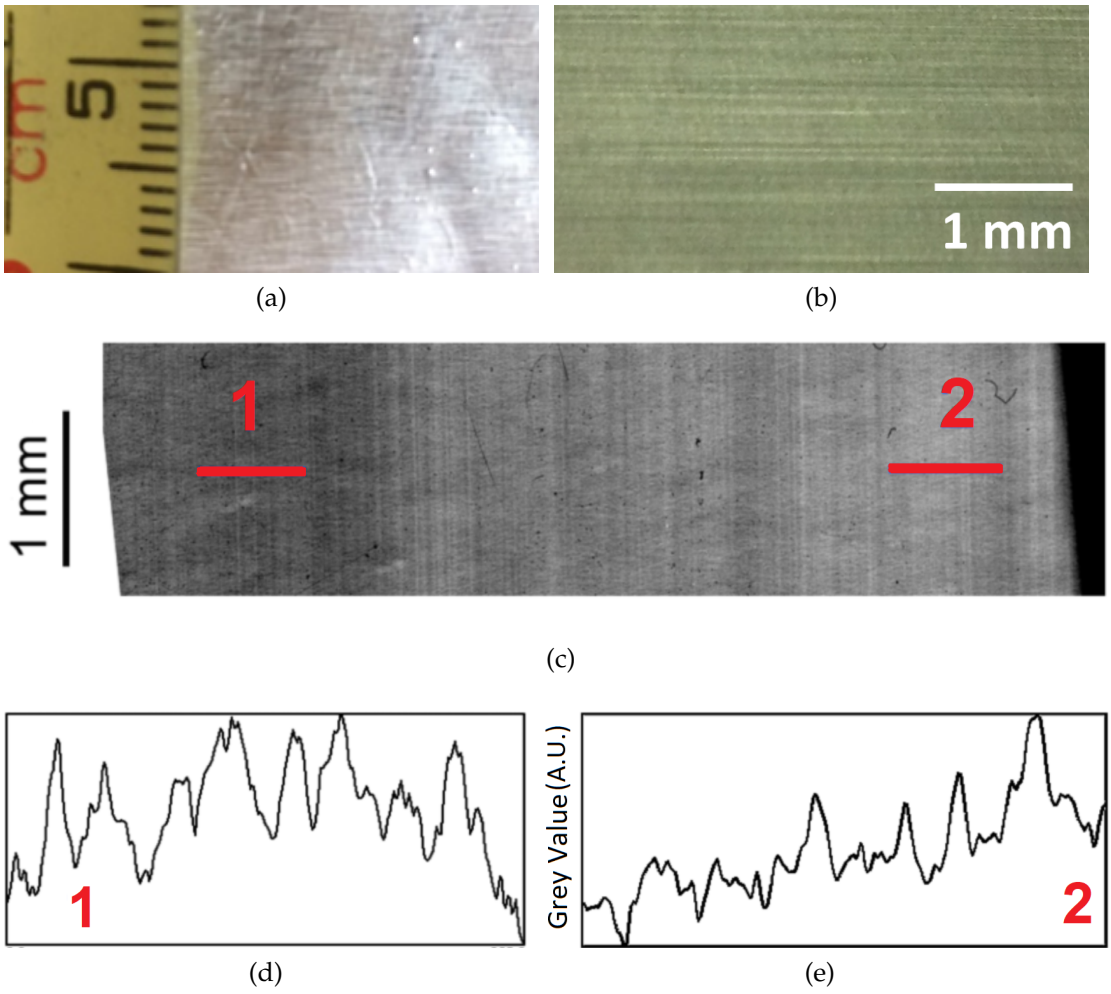

Figure 5.7: (a) A photo, (b) a microscope image and (c) a radiograph of an Al foil that is not carrying any current. (d) & (e) Profile plots taken along parts of the horizontal red lines in (c). The observed feature size in (b) is 60 - 80 μm and that in (c) is $\sim$ 30 μm.

electrothermal instability, from linear analysis, would reach and cross a minimum unstable feature size of about 30 μm early in the current pulse. Computing Eq. 5.2 near the beginning of the current pulse, when the liner is still expected to be in solid state using the current integral, the theoretical feature size is strongly affected by the rapidly increasing current density, weakly by the slowly changing thermal conductivity, and not at all by the constant $\frac{\partial \eta}{\partial T}$. At 50 kA the estimated minimum feature size is 36 μm and at 100 kA it is 18 μm.

Now note that there is sufficient initial mass variation in the foil at a 30 μm scale size to be detectable via a few keV radiography (Fig. 5.7 (c)). This will lead to hotter and colder bands forming at that size due to the different ohmic heating rates per unit mass in these bands for seeded experiments. Hence, once the instability size crosses the size of these bands, they can then seed the instability and produce azimuthally correlated features that look similar to the initial foil structure. The feature size measured is slightly smaller than the size of the foil's pre-existing structure, which means the features are not a simple amplification of the initial structure. In the non-seeded experiments, random physical and material non-uniformities in the foil would first lead to growth of local hot spots which might then lead to the interspersed pattern observed.

The observations regarding ripple size and contrast differences may be explained by the foil's initial mass variation. This variation in the foil may lead to faster instability growth earlier on in the seeded experiments and could be a contributing factor to the measured contrast difference. These two observations may also in part be explained by the different structures' geometries, keeping in mind the high pressures generated at vaporization and assuming that is driving the expansion. In the non-seeded experiments, once the curved azimuthally-limited hot regions vaporize, the vapor will be able to expand in the r, z and θ directions. In the seeded case, assuming the correlated features vaporize at about the same time, this vaporized region will face higher pressure in the θ direction and lower pressure in the r and z directions. This will lead to vapor expanding primarily in those two directions, hence into less volume. That in turn will result in increased areal density variation for the same feature size compared to non-seeded experiments a) along an axial line profile plot and b) in the $r - z$ plane. To approximate this difference in density variation quantita-

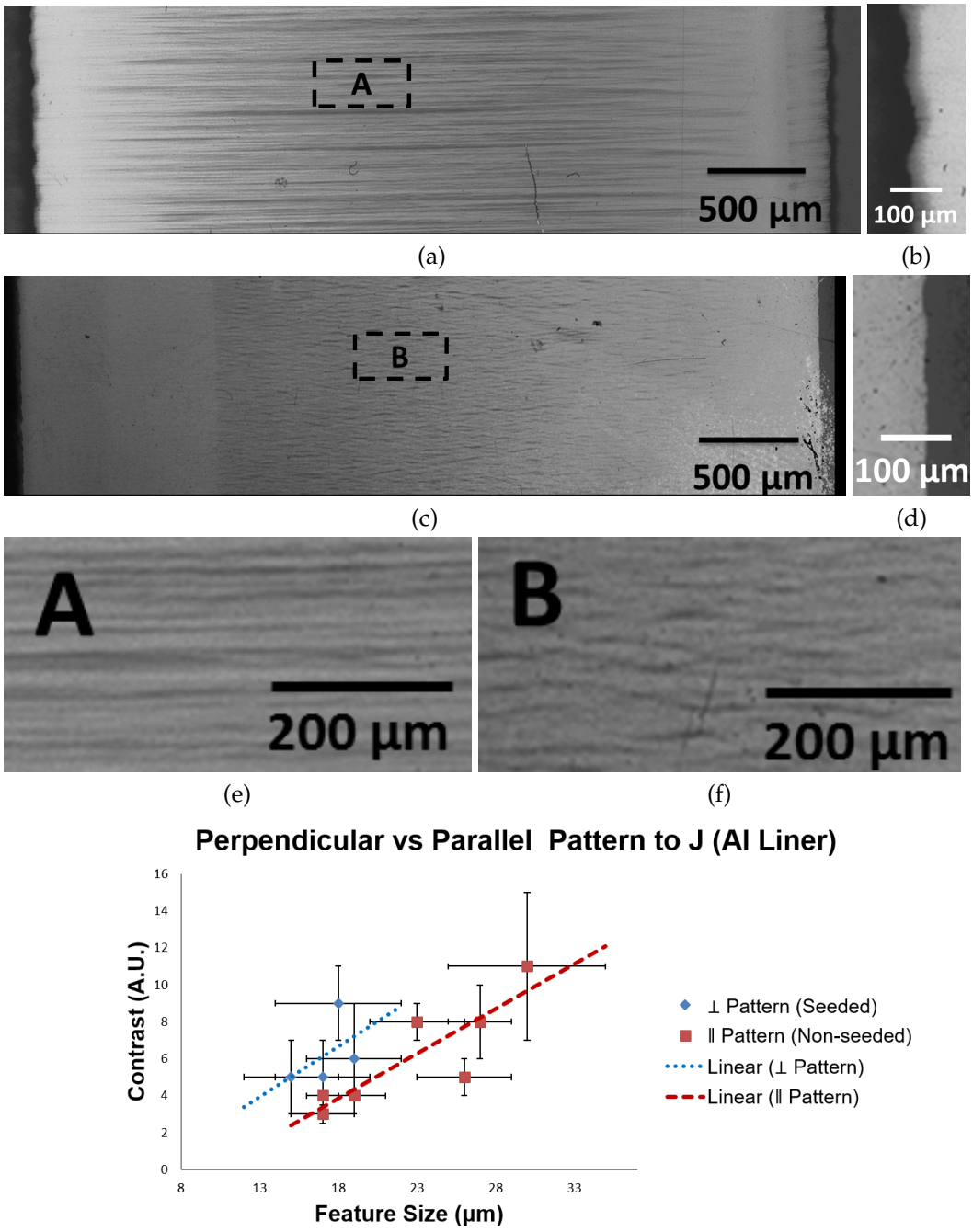

Figure 5.8: Radiographs showing the effect of an Al liner's foil orientation. (a) Radiograph with the foil's pattern perpendicular to current flow with (b) a zoomed-in view of the left edge. (c) Radiograph with the foil's pattern parallel to current flow with (d) a zoomed-in view of its right edge. (e) & (f) Zoomed-in views of the boxes in a and c. (g) Correlation between feature size and areal density variation (contrast) in perpendicular and parallel oriented foils.

tively, we can use a planar geometric approximation. Looking at the liner's surface as a 2-D plane, in the seeded experiments 100 % of the vapor mass moves axially along the surface. In the non-seeded experiments, approximating the interspersed patterns as rectangles, we get a length-to-width ratio of 5-10. Consequently, assuming a spatially uniform mass flow-rate across a given rectangle, the high pressure vapor drives 5-10 units of mass out of the rectangular region in the axial direction for every unit of mass leaving in the azimuthal direction. This means that, at the time of observation, 10-20 % of the total vapor mass now moves in the azimuthal direction across the edges instead of the axial direction. Hence we get a 10-20 % difference in density variation. This number is less than the measured difference of 20-30% in Fig. 5.8 (g), but it is a significant portion of it and may be an important effect.

CHAPTER 6

INVESTIGATION OF MILLIMETER SCALE FEATURES

6.1 Motivation

In MagLIF experiments carried out without an applied field on the 20 MA Z machine [14] at Sandia National Laboratories, an interesting observation in soft X-ray radiographs was the formation of half millimeter scale horizontal striations perpendicular to the current flow in the imploding liner.[35] Peterson, *et al.* proposed that these striations were caused by μm scale structure that developed earlier in the current pulse due to the non-ionized electrothermal instability and that later acted as a seed for the Magneto-Rayleigh-Taylor instability [33]. As discussed in Chapter 3, the electrothermal instability on its own cannot account for the 100 μm to millimeter scale structure that was observed.

Furthermore, applying an external axial magnetic field was shown to give these striations a helical pattern when viewed with soft X-ray radiography [65, 36]. Figure 6.1 shows sketches of how the striations in the liner appear from a side view.

The experiments reported here were motivated by the formation of these striations with and without an axial magnetic field. The principal diagnostic, the time gated XUV self-emission imaging system, was different from the principal diagnostic used on the Z-machine, X-ray radiography. While Awe's radiographs on Z looked at density through both sides of the liner in the same image, our images see self-emission only one side at a time as the liner is optically thick in the observed wavelength range. A typical COBRA current pulse for all ex-

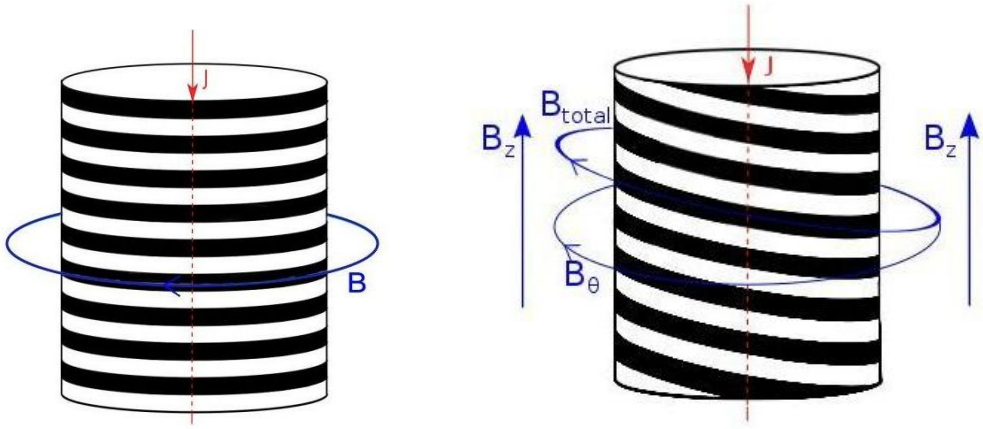

(a) (b)

Figure 6.1: Idealized sketches of cylindrical liners showing striation patterns (a) without and (b) with an axial magnetic field. The quantity B_{tot} is the vector sum of B_z and B_θ, the azimuthal field due to the axial current in the liner.

periments in this chapter is shown as a solid line in Fig. 6.2. The figure also shows two $\dot{B}$ traces which will be discussed in section 6.3.2. Two experimental arrangements were used to generate the axial magnetic fields. The first produced a time-varying and spatially non-uniform field by using twisted return current wires. The second produced a steady-state and spatially uniform field by using a Helmholtz coil. These will be described in detail in the following section.

6.2 Experimental Arrangement

6.2.1 $\dot{B}$ Probes

The light-based diagnostics used were time-gated self-emission XUV imaging, laser shadowgraphy, and time-integrated optical self-emission imaging. The

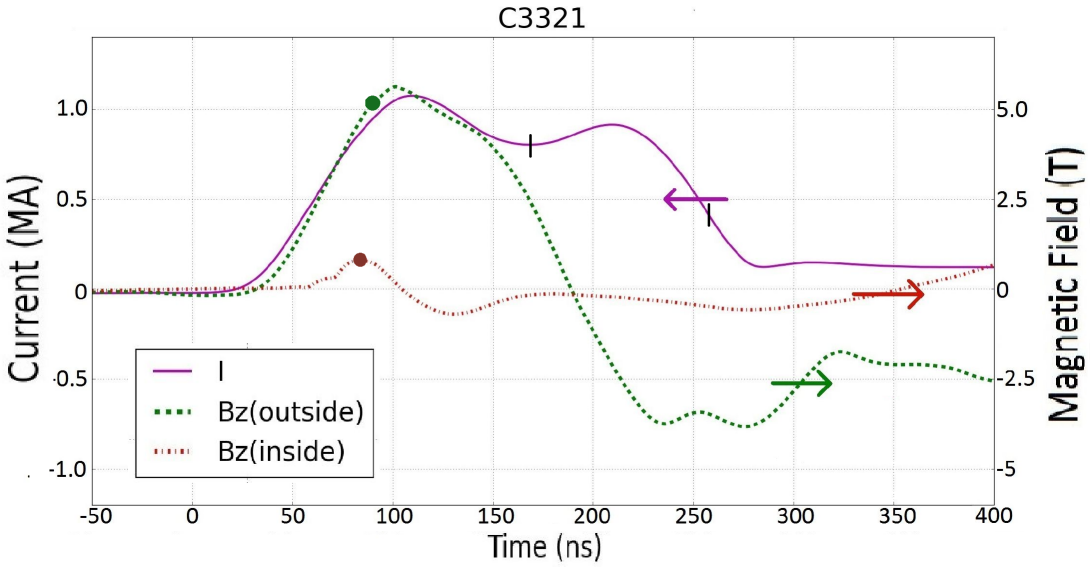

Figure 6.2: A typical COBRA current waveform produced in our experiments is shown. The vertical lines on the current trace delimit the interval during which XUV images were taken. The waveforms here correspond to pulse C3321 which used the twisted return current wires configuration. Measured axial magnetic fields both inside and outside the liner are shown in dash-dotted and dotted lines respectively. The estimated probe failure time is depicted on each probe's trace as a circle.

line-of-sight of the XUV detectors was near perpendicular to the optical detectors.

Magnetic fields were measured using micro $\dot{B}$ probes. Single loop probes, illustrated in Fig. 6.3(b), were placed outside the liner near its surface, as shown in Fig. 6.3(a) for the twisted return current wire experiments. Probes could be oriented to measure either axial or azimuthal magnetic fields. A probe was also placed on axis inside the liner, as shown in Fig. 6.3(a), to measure the axial field that penetrates through the liner.

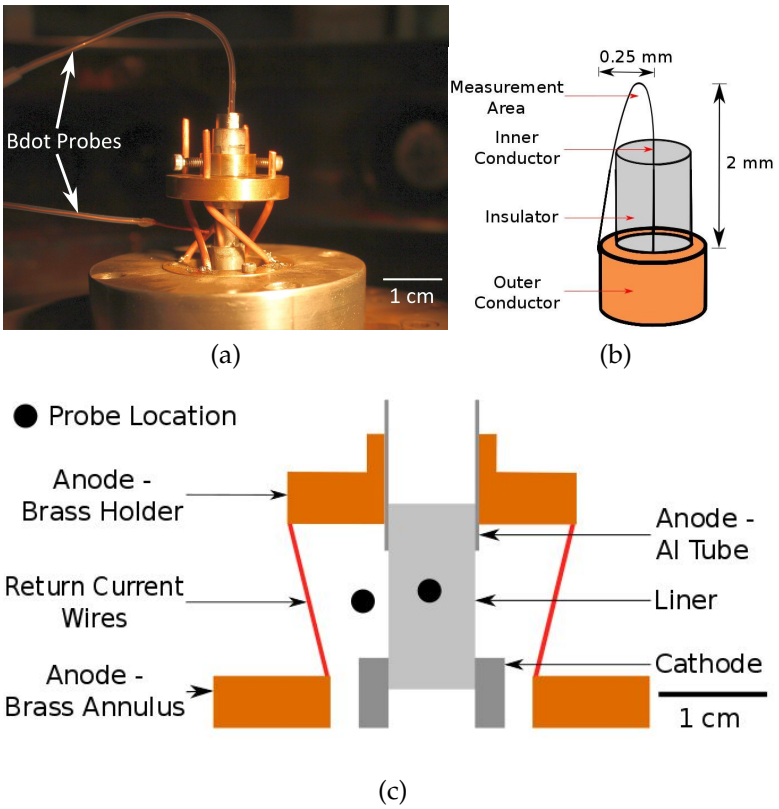

Figure 6.3: (a) A photograph of the twisted return current wires experimental arrangement. Copper wires, 2.1 mm in diameter, placed at a distance of 12.7 mm from the center line of the liner, were rotated 90° either clockwise or counterclockwise. A $\dot{B}$ probe on the end of a solid coaxial cable was positioned in the center of the liner. Another was positioned approximately 2.5 mm outside the liner wall. (b) A sketch of these $\dot{B}$ probes. (c) A sketch of the hardware configuration without the probes. The circles depict the location, not the orientation, of the probes.

6.2.2 Liner Configurations

Two designs were used for the liners. The first was the one-piece Al liner shown in Fig. 6.4. This liner was machined down to its final profile from an Al rod. The wall thickness of the liner tube shown in Fig. 6.4(a) was 50 μm. The bottom part of the piece was threaded so that it could be screwed into the brass cathode base, as shown in Fig. 6.4(a). The length of the tube, measured between anode and cathode, was 1 cm and the inner diameter of the liners was 4 mm.

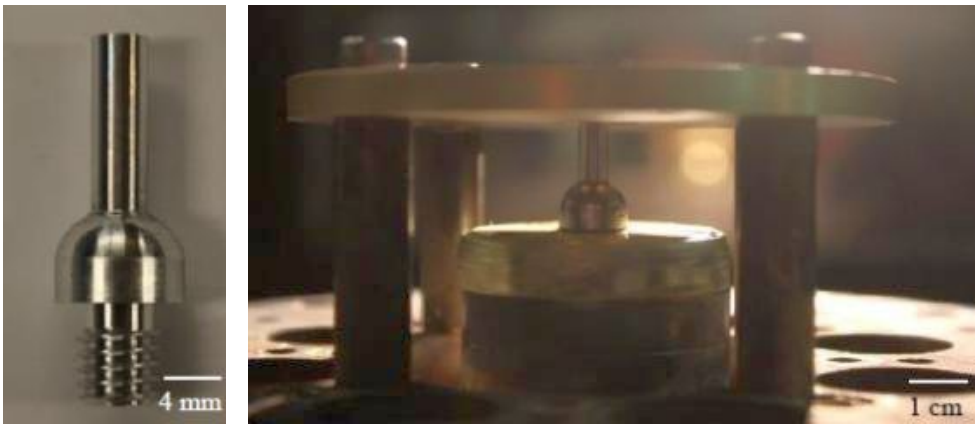

(a) (b)

Figure 6.4: The one-piece liner, consisting of a threaded section for mounting and a liner section, is shown in (a). The fully mounted design is shown in (b).

The second design consisted of a 4 or 16 μm thick Al foil wrapped into a cylinder with one or two turns. This was similar to the design used in the liner instability studies previously done on COBRA [66]. The cylindrical foil was placed inside a tube holder by sliding it through a hole in the anode into the bottom holder, which was the cathode, as shown in Fig. 6.3 and previously described in Chapter 4. Contact was made by the liner on the holder walls. The liners in this design were also 1 cm in length and were approximately 4, 8, or 16 mm in inner diameter.

Different diameters enabled a variation in the azimuthal magnetic field, B_θ, on the surface of the liner produced by the 1 MA current pulse flowing through it. The azimuthal field is given by

$$B_\theta = \frac{\mu_0 I}{2\pi r} \tag{6.1}$$

where r is the radius of the liner, μ_0 is the free space magnetic permeability and I is the current.

6.2.3 Straight Post and Twisted Return Current Wires Configurations

For experiments that did not require an externally applied axial magnetic field, straight return current posts were used, as shown in Fig. 6.4(b). The experimental results without a field shown below used liners of both the first and second design, with similar results. In experiments with applied B_z, it was important to reduce the self-generated B_θ from the liner in order to have a detectable striation tilt. Hence, for the twisted return current wires experiments we used 8 mm diameter liners. However, 50 μm thick liners with that diameter did not emit in the XUV wavelength. They were too massive and heated insufficiently. Thus, the experimental results from the twisted wires shown here were of the second design. They have an inner diameter of 8 mm and are double wrapped using 4 μm thick foil.

To produce an axial magnetic field in the configuration shown in Fig. 6.3, four 2.1 mm diameter copper wires placed inside four equally spaced holes, each a distance 12.7 mm from the center, carried the current between upper and lower anode plates. The upper anode section was rotated 90° by hand either clockwise or counterclockwise, and was at a height of 2.5 cm with respect to the lower section. Solder was applied at the connections between the copper wires and the brass holders. The part of the anode that touched the liner consisted of an Al tube that could slide freely inside the top brass holder, as shown in Fig. 6.3. This way, the configuration could be adjusted so that the liner was always 1 cm long before vacuum pump-down (between cathode and anode).

The possible disadvantages of this arrangement were the following. First,

the rotation and concentricity of the Cu return current wires were determined only by eye. A more robust method for the rotation could be devised. However, the non-uniformity of the axial magnetic field at the liner due to a possible deviation from concentricity is much less significant than that due to there being only four twisted return current wires. This non-uniformity is visible in our data and will be discussed further in the results section. Second, the $\dot{B}$ probes used to measure the B_z field were positioned at varying locations around the liner. As the magnetic field from the return current wires is inherently non-uniform, $\frac{B_z}{B_\theta}$ is location specific. However, as we will be looking only at average ratios of the field components and comparing them to average striation tilt angles, the $\dot{B}$ measurements are still meaningful for qualitative comparison.

6.2.4 Helmholtz Coil Experimental arrangement

For the second experimental arrangement, a Helmholtz coil having a 150 μs rise time was used, which is considered steady-state on the time scale of the COBRA pulse. The spatial uniformity of the coil, with the load hardware included, was within 5% in the area of interest. This coil produced 0.5 T to 1.5 T axial magnetic fields depending on the driving capacitor bank voltage. A photograph of the coil with a loaded liner, along with a $\dot{B}$ probe on axis in the liner, is shown in Fig. 6.5(a).

Most liners used in the Helmholtz coil experiments were single wrapped 4 μm thick foils of the second design, with an overlap region of 3-5 mm, and are shown in the sketch of Fig. 6.5(b). Some of these experiments used liners that were single wrapped on one side and double wrapped on the other side.

We will refer to such liners as 1.5 turn liners. Experiments with the latter liners investigated what effects doubling the current path area might have on the striations.

The liners were 16 mm in diameter in all of the Helmholtz coil experiments. As mentioned before, the reason for the larger diameter was to reduce the azimuthal magnetic field produced by the machine current running through the liner. The applied B_z was 1.5 T at most. The expected maximum azimuthal magnetic field strength at an 8 mm radius was about 25 T, giving a minimum $\frac{B_z}{B_\theta}$ ratio of 0.06. If the helical pitch is determined by this magnetic field ratio, then the minimum pitch angle would be 3.4°.

At this point, let us define the average angle of striations as the projected average, measured via averaging straight lines drawn between the leftmost and rightmost ends of given striations in the images. Note that the measured average angles from our XUV images will be different from the real angles because we are looking at a 2-D representation of a 3-D cylindrical system. For a given striation, the vertical height change from one side to the other in both geometric systems is the same, but the horizontal distance changes from $2r$ to πr between these two systems. This changes the angle by a factor of $\frac{2}{\pi}$, as shown in Eq. 6.2.

$$\theta_{3D} \approx \frac{B_z}{B_\theta} = (\frac{y}{\pi r}) = \frac{2}{\pi}(\frac{y}{2r}) \approx \frac{2}{\pi}\theta_{2D} \tag{6.2}$$

where θ is the angle in radians, y is the vertical delta, r is the radius of the liner, and a small angle approximation has been used.

Using this, we note that the 3.4° will actually correspond to a 5.3° measured angle, which we should be able to detect in our XUV images. To avoid confu-

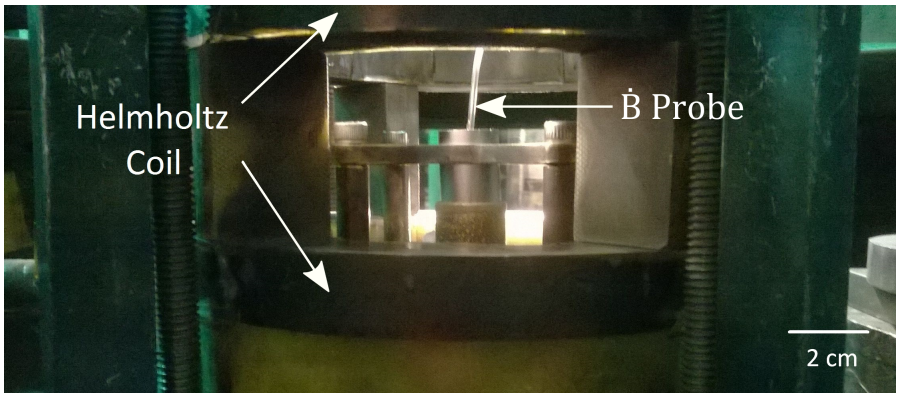

(a)

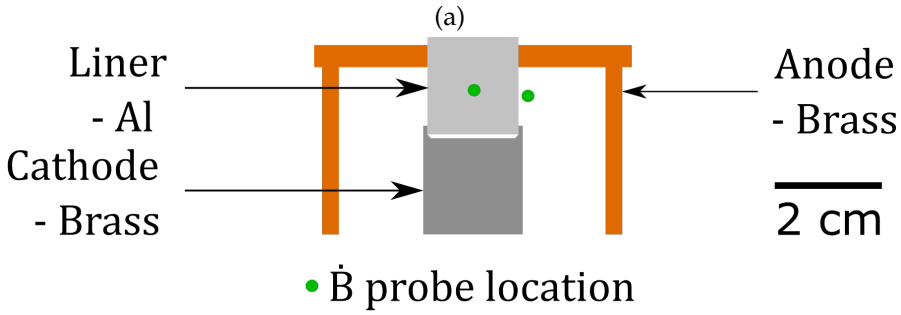

(b)

Figure 6.5: Photograph and sketch of the Helmholtz coil experimental arrangement. The sketch highlights locations where magnetic probes were positioned in various experiments.

sion, from now on all angles given will be the 3D angles that occur in reality as that is what is of interest. We also note that local angles will have their own transformation factors as $\frac{2}{\pi}$ is not appropriate when dealing with short sections of a striation. While most angles presented will be averages, we will explicitly point out when we talk about local angles.

6.3 Experimental Results and Discussion

6.3.1 No Applied Axial Magnetic Field

In this section, a number of observations will be made that imply the liner's perceived self-emission structure, which is related to plasma temperature, and surface ripples, which are related to plasma density, are linked to the same growth mechanism. Moreover, the spikes and bubbles will be shown to respectively match with weaker and stronger perceived radiation, both in the visible light and XUV energy ranges. We propose that the matching is due to radiation, coming from an inner region in the liner, being absorbed as it passes through the spikes. In section 6.3.4, we will show that PrismSpect simulations support this hypothesis, within a set of density and temperature approximations. Also, to clarify, whenever the words "spikes" and "bubbles" will be used, these are referring to the liner's surface ripple's extruded regions and non-extruded regions respectively. The terminology does not imply an association with the MRT instability.

Without an axial magnetic field, horizontal striations with deviation of up to $\pm\ 2^{\circ}$ were observed in XUV self-emission, as shown in Fig. 6.6. Please note that all deviation values presented in this chapter reflect the maximum change in angle and not a standard deviation. Also, all XUV images shown are, once again, "negatives", meaning that darker regions correspond to stronger emission and vice-versa. The wavelength of the striations, when comparing no applied field experiments with the alternative, did not noticeably change: they all averaged 600 - 750 μm when looking late in time.

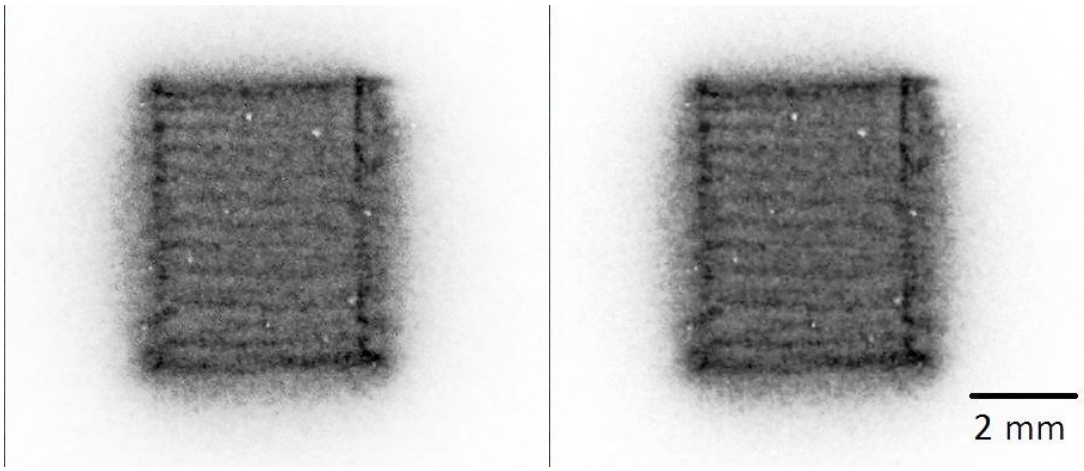

(a) C3170 - 210 ns (b) C3170 - 250 ns

Figure 6.6: Side-on XUV emission from a 50 μm thick aluminum liner without an axial external magnetic field. The striations appear horizontal, with a pitch of $0 \pm 2^{\circ}$. The time given for each image, in this and the following figures, represents the start of the 10 ns gate pulse with respect to the start of the current pulse, as shown in Fig. 6.2.

As described in Chapter 2, the detectors that imaged the laser shadowgraphs were noticeably sensitive to time-integrated visible light self-emission emanating from the liner. Therefore, in the following discussion, when we want to allude to both shadowgraphy and self-emission measurements in the images, we will use the broadly encompassing terminology "visible-light imaging".

The setup for experiments using liners that were partly covered with a dielectric was described in Chapter 4 and is shown here in Fig. 6.7 (a). Figure 6.7 (b) - (e) show results of an Al liner with a 225 μm thick dielectric placed over half of its outer surface carrying a 1.1 MA 120 ns rise-time current pulse. The second shadowgraph shows small ripples appearing on the surface of the insulator, while slightly larger ripples are present at the surface of the uncovered liner. Overall, the dielectric, whether kapton or mylar, whether 50 μm or up to 225 μm thick, mitigates, but does not prevent, expansion of the liner through-

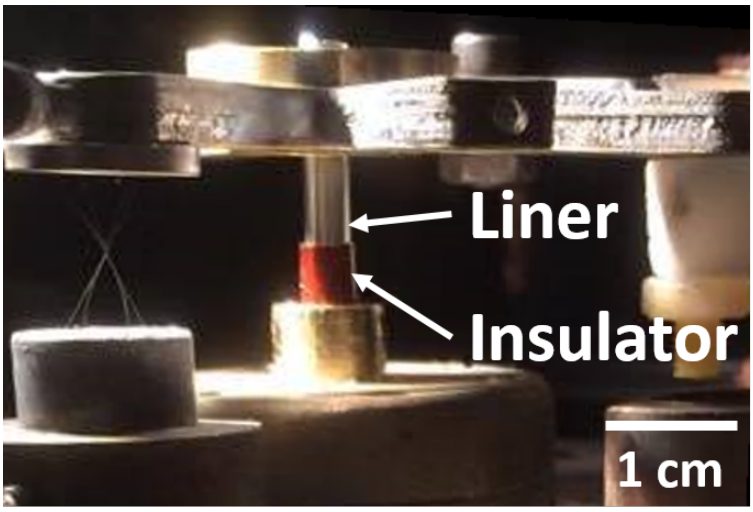

(a) Setup.png

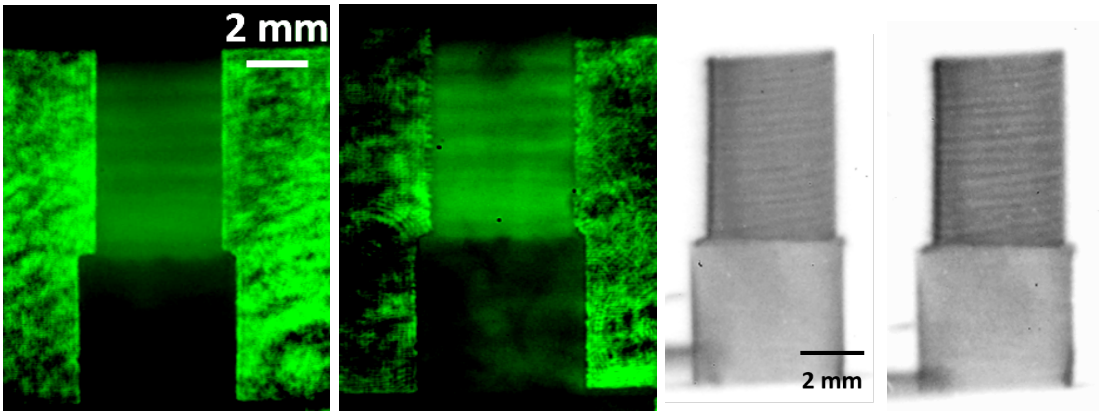

(b) Shadowgraph - 70 ns (c) Shadowgraph - 90 ns (d) XUV - 100 ns (e) XUV - 110 ns

Figure 6.7: (a) Setup of half-insulated Al liner carrying a 120 ns rise-time 1.1 MA current pulse. The liner has a thickness of 16 μm and a diameter of 4.2 mm. The insulator shown comprises of 3 dielectric layers with a total thickness of 225 μm. (b)-(c) Visible-light imaging and (d)-(e) XUV self-emission imaging of the experiment.

out the pulse. This expansion is visible in subsequent images presented in this section.

The self-emission striation pattern radiating from the uncovered liner region in the visible-light images displays a larger wavelength than the pattern visible in the XUV self-emission images. The latter pattern in turn has a larger wavelength than the surface ripples in the shadowgraphs. If the ripple and self-

emission structures are linked to the same phenomenon, then the difference in structure size can simply be attributed to a growth over time, eventually reaching a saturation wavelength.

Note that the structure in the XUV images is slightly angled while that in the optical self-emission images is visibly horizontal. One evident explanation for the mismatch is that the XUV cameras are viewing the liner nearly orthogonal to the shadowgraph, hence they are not looking at the same 2-D projected surface.

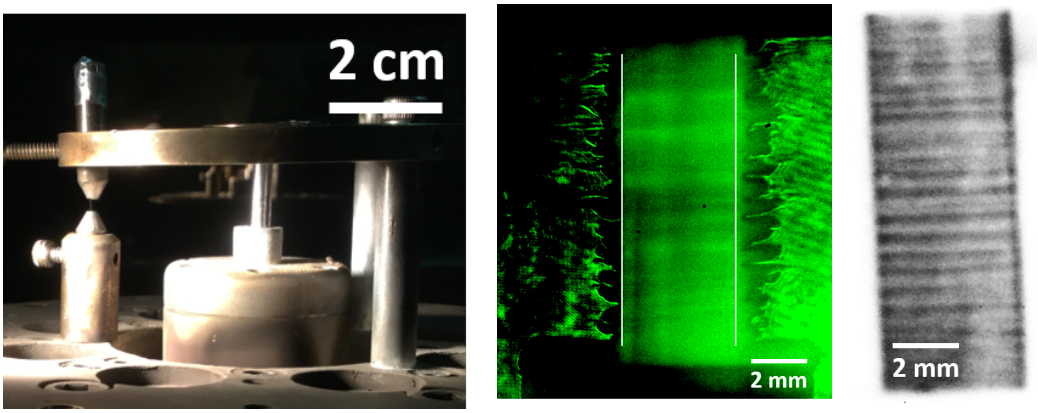

(a) Setup.png (b) Shadowgraph - 110 ns (c) XUV - 70 ns

Figure 6.8: (a) Setup, (b) visible-light imaging and (c) XUV self-emission imaging of a 4.2 mm diameter 16 μm thick Al liner under a 1.1 MA 110 ns rise-time current pulse. The white lines in (b) represent the liner's initial position.

Figure 6.8 shows data for a 4.2 mm 16 μm thick Al liner using a 1.1 MA 110 ns rise-time current pulse. The white line indicates the liner's initial position. The striation features' wavelength in the XUV image, taken at 70 ns, is about 25% smaller than the ripples' wavelength taken at 110 ns. That again may be explained by growing features in both wavelength and amplitude. Also notice the radial extent of the liner's XUV self-emission. It is limited to a rather straight surface contained behind the spikes that appear in the shadowgraphs. While there is a 30-40 ns time difference between the two images in this experiment, the above characteristic of the XUV self-emission boundary is also true when

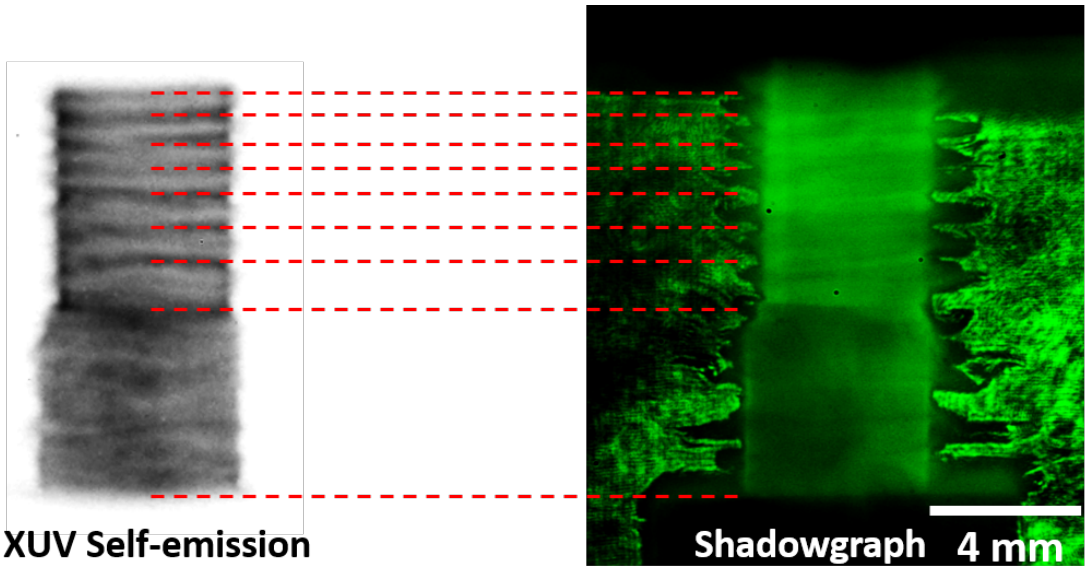

Figure 6.9: Time aligned XUV self-emision and shadowgraphy of a half-insulated Al liner similar to Fig. 6.7 taken at 200 ns in a 240 ns rise-time 1.05 MA current pulse. The time gated XUV and time integrated optical self-emission patterns match with the time-gated ripple pattern of the shadowgraph, as indicated by the dashed red lines.

observing the images simultaneously, as shown in the next result.

Figure 6.9 displays data from an experiment similar to that of Fig. 6.7, except with a pulse having a 240 ns rise time to peak current. The data is taken considerably later in the current pulse, at 200 ns, than that in Fig. 6.7. In Fig. 6.9, we see up to 1-2 mm extension of the spikes now. We also see XUV self-emission coming from a nearly straight cylindrical surface radially behind the spikes, as before. Furthermore, the time-integrated self-emission pattern from the uncovered liner in the shadowgraph now matches the surface ripples well, and it also matches the pattern on the XUV image. This correlation of the time-integrated and time-gated features suggests that there is a saturation wavelength of the features. One important detail in the result shown is that the bubbles match with the stronger emitting regions and the spikes with the weaker emitting regions.

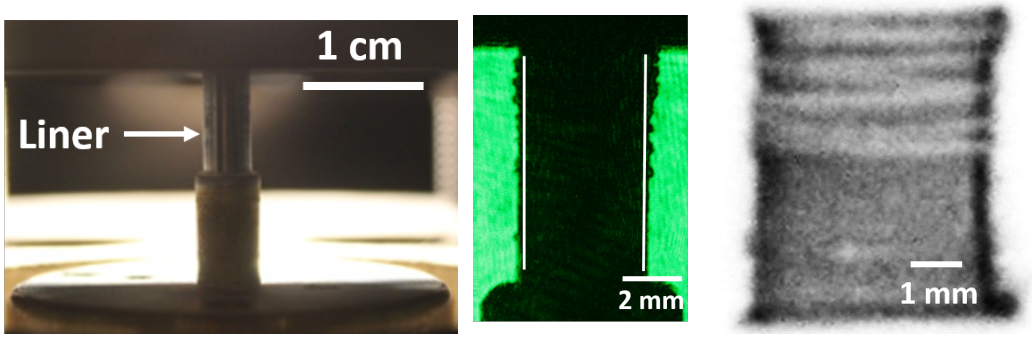

(a) Setup (b) Shadowgraph - 115 ns (c) XUV - 170 ns

Figure 6.10: (a) Experimental setup, (b) laser shadowgraph and (c) XUV self-emission image of C3161. In (b), the white lines indicate the liner's initial position.

Figure 6.10 shows results of an $\approx$ 4 mm diameter 50 μm thick Al liner experiment, displaying an early-time shadowgraph and a late time XUV self-emission image. The white lines in the shadowgraph indicate the liner's initial position, as obtained from a shadowgraph taken before the current pulse. The pulse had a 130 ns rise-time and a peak current of 1.0 MA. In the shadowgraph, we see clear axial non-uniformity in the ripples' amplitude. In the XUV image, we see matching axial non-uniformity in the visibility of the striations. This supports the observed correlation between the ripples and the self-emission pattern shown in the earlier figures. There may also be a correlation between ripple amplitude and striation contrast.

A final observation concerning the striation pattern without an applied axial magnetic field is shown in Fig. 6.11, where a rectangular slot was cut into the Al liner: the striations develop perpendicular to the current channels. There are clear differences in the striation orientation caused by the slot in the images. The current channels that would have flown through the slot region if the gap was not there can be expected to bend in these experiments in order to bypass the gap, as shown in Fig. 6.11 (e). The striations bend accordingly, orthogonal to

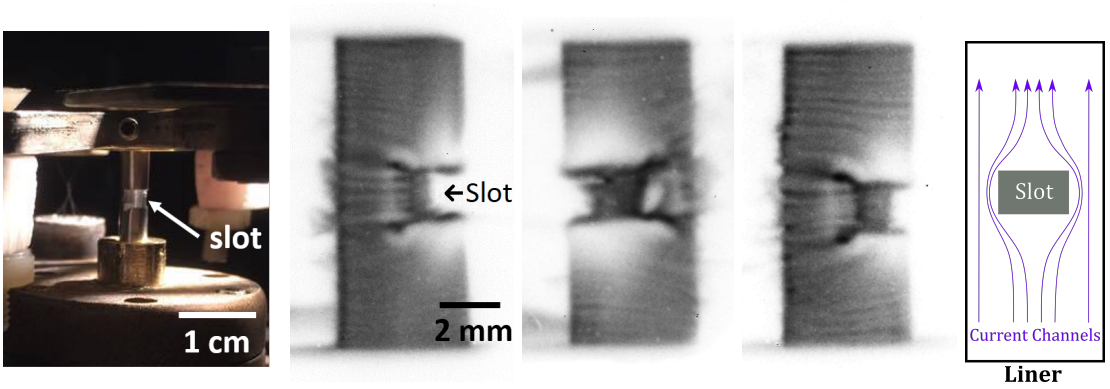

(a) Sample Setup (b) C4381 (c) C4382 (d) C4383 (e) Sketch

Figure 6.11: (a) Sample Setup, (b)-(d) XUV images, and (e) schematic representation of Al liner experiments with a slot cut into them.

such an expected current path. Note that the lines of strong radiation extending from the slit's corners could be due to micro-tears produced from the cut in the foil.

6.3.2 Twisted Wires Results

Sample experimental results when the axial field was produced by the twisted return current wires are shown in Fig. 6.12. The difference between pulse C3317, corresponding to Fig. 6.12(a) and (b), and pulse C3318, corresponding to Fig. 6.12(c) and (d), is the direction of the axial magnetic field determined by the return current wire twist. C3318 is turned clockwise when viewed from above, similar to Fig. 6.3, producing an axially downward magnetic field at the liner's surface. The opposite is true for experiment C3317.

With four return current wires, the uniformity of the axial magnetic field at the liner radius, both azimuthally and axially, was poor. As a result, $\frac{B_z}{B_\theta}$ in the areas of the liner closer to the wires was greater than elsewhere. However,

a meaningful average pitch angle could still be measured from the images for both twist orientations: both cases averaged $8 \pm 1^\circ$ in their respective directions. Considering the sources of error, this matches reasonably well with analysis using a combination of basic calculations of the expected B_θ field and data from $\dot{B}$ probes, as will be shown.

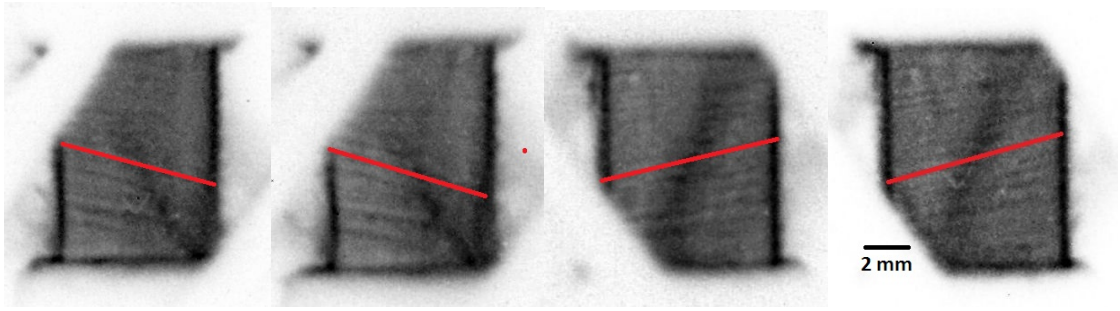

(a) C3317 - 190 ns (b) C3317 - 220 ns (c) C3318 - 180 ns (d) C3318 - 210 ns

Figure 6.12: Side-on XUV emission of COBRA pulses 3317 and 3318. C3317 had a counterclockwise twist in the anode section, producing an upwards axial magnetic field. C3318 had a clockwise twist similar to Fig. 6.3, producing a downwards field. One can see that the pitch does not change with time.

Fig. 6.3 shows the hardware configuration for the data used in the following discussion. According to the probe external to the liner, the maximum axial field strength measured roughly midway between anode and cathode axially, at the midpoint between two return current wires azimuthally, and 2.5 $\pm$ 0.5 mm radially outside the liner was 5.6 T (Fig. 6.2). As the return current wires were at an angle of approximately 45°, it is reasonable to assume that a similar strength azimuthal magnetic field due to a single wire was present. The current at this time is close to 1 MA. Note that the "single wire assumption" will introduce some error as the combination of four wires will reduce the measured B_θ whereas B_z contributions will add. To get the proper fields with the load hardware, a 3 dimensional simulation could be run. However, such a simulation would not be including magnetic field non-uniformities from the current flow

and plasma ablation dynamics discussed in section 6.3. Hence, the following discussion will be semi-quantitative instead as that is useful in illustrating all the factors that need to be taken into account in the twisted wire configuration.

In both twist orientation cases, the azimuthal field created by the wire currents will add to the B_θ generated by the current flowing through the liner. According to Eq. 6.1 which assumes azimuthal symmetry, the machine current flowing through the liner generates 31 T azimuthal magnetic field at the radius of the probe (4 + 2.5 = 6.5 mm) when the "axial" $\dot{B}$ probe reads 5.6 T. Using a superposition of azimuthal fields generated from the current running through the liner and the return current posts, the total azimuthal field at the location of the probe becomes 36.6 T. The $\frac{B_z}{B_\theta}$ ratio of $\frac{5.6}{36.6}$ gives an angle of roughly 7°. However, this ratio is valid only near the probe and not at the liner surface.

We do expect a discrepancy between this $\frac{B_z}{B_\theta}$ and that measured from the XUV images. In general, this discrepancy is likely to have four sources: imprecise angle measurement due to spatial and temporal limitation of XUV camera resolution, the "single wire assumption", probe locations 2.5 mm exterior to the liner, leading to the axial and azimuthal field ratio being different at those locations compared to the ratio at the liner wall, and error in the location and orientation of the probes when placing them. If the striation tilt angle corresponds to $\frac{B_z}{B_\theta}$, then the last of these four sources is the most important and quite significant. It is reasonable to assume that the orientation of the probe relative to the z-axis may have an offset of up to 10°. This roughly corresponds to measuring 15% of the B_θ in the B_z measurement, giving an error bar of $\frac{\pm\Delta B_z}{B_z} = \pm 60\%$.

In addition to the tilted striations, a wide column of plasma can be seen in Fig. 6.12, stretching from the cathode to the anode at an angle of about 30° from

the vertical. The source of that hot plasma is yet to be determined for certain, but it is likely due to the load hardware. It is not due to the presence of a seam in the liner as the quad-cams were positioned 180° from one another and both quad-cams saw such a plasma column.

Another measurement of interest in these experiments was the axial magnetic field inside the liner. An example is shown by the dash-dotted curve in Fig. 6.2 for pulse C3321. First, there is a time delay between the axial field outside the liner and that measured inside. This is to be expected as the field has to diffuse through the liner. However, when the field does appear inside the liner, it increases in two bursts rather than a smooth increase, as seen outside the liner. This suggests that the magnetic field does not penetrate through the liner via a simple field diffusion process. One possible explanation for the bursts could be magnetic flux compression via radially converging plasma ablated off the inside surface of the liner. It is possible that a wave reaches the inside surface of the liner and carries plasma from there radially inward. The presence of converging shock waves inside thick liners has been studied recently by Burdiak *et al.* [45] In comparison with those experiments, the main differences in our experimental arrangement were that our liners were thin (8 μm, which was significantly less than the skin depth), made out of double wrapped foil, and had no gas fill.

6.3.3 Helmholtz Coil Results

We also observed a tilt in striations in single wrapped foil experiments using the Helmholtz coil. Referring to Fig. 6.13, the orientation of the average tilt angle matches in orientation with the twisted wires experiments, i.e. left-handed

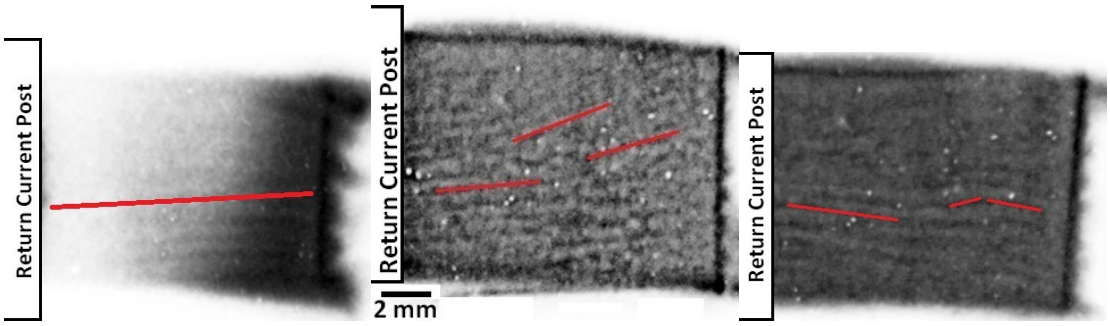

(a) C3626 - 240 ns (b) C3624 - 200 ns (c) C3623 - 205 ns

Figure 6.13: Side-on XUV self-emission images from COBRA pulses 3626, 3624, and 3623 having 0.5 T downwards, 1.5 T downwards and 1.5 T upwards axially applied fields respectively. A return current post was blocking about 1/3 of the liner on the left side of each image, as shown. The liners were single wrapped and specific striation tilts discussed in the main text are highlighted in red.

twist for an upwards axial field and right-handed twist for a downwards applied field. The average angle shows some correlation with the applied axial field strength. In pulse C3626, in which a 0.5 T downward field was applied, the average is 3° whereas in pulse C3624, in which a 1.5 T field was applied, the average is 8°. Multiple measurements of the average angle in an image gave a maximum variation between 0.75° and 1.25° from the averages given above. Note however that local variations in tilt are not reflected in the average value and can be significant. This variation is present both azimuthally and axially along the liner, as shown in Fig. 6.13. For example, the angles of the highlighted striations in C3624 shown in Fig. 6.13(b) and determined using local transformation factors change from 6° to 18°.

C3623 stands out as an exception. That experiment had a 1.5 T applied field upwards producing the striations shown in Fig. 6.13(c). The average angle is 4.7 ± 1 °. However, a small section of the striations are tilted in the opposite direction from the average angle orientation. Since the magnetic field was applied only in one direction, this suggests that either the striations observed are

not determined purely by the magnetic field ratio, or that there was azimuthal non-uniformity in the current distribution in the liner such that the twisting of the current channels produced oppositely directed B_z fields. Bott-Suzuki *et al.* [67, 68] showed that vacuum gaps at contacts can cause non-uniform current flow with an azimuthal magnetic field variation of up to 50% that persists along the liner. While we did not introduce vacuum gaps on purpose, there were bound to be contact gaps at the electrodes in our wrapped liner hardware. Hence, we think it is possible that there was a non-uniform azimuthal and axial current distribution, at least in that particular liner, that persisted throughout the pulse. Such non-uniformity could also explain why there is a large angle variation in the tilts at a given time. Furthermore, 16 mm diameter wrapped foils have less curvature than, e.g., 4 or 8 mm diameter wrapped foils. This means that the mechanical forces generated in the material to straighten the originally flat foil is smaller for wider tubes. That can lead to larger vacuum gaps, and hence larger current non-uniformity, which can explain why we see larger angle variations in the Helmholtz experiments, where the field is uniform, than in the twisted return current wire experiments, where the field is spatially varying.

In all our experiments the tilt angle stayed constant in time, within the angle variations described above. This in itself does not confirm that the striation angle is locked in starting at a certain time or disprove that the striations continuously follow the changing magnetic field lines as the images were taken at nearly constant current, hence nearly constant B_θ. However, the angles measured do not correspond to the angles one would expect from the $\frac{B_z}{B_\theta}$ ratio at the times of measurement, as shown in Fig. 6.14. The measured angles are higher, corresponding to a higher $\frac{B_z}{B_\theta}$. Possible explanations will be discussed in section

6.3.4.

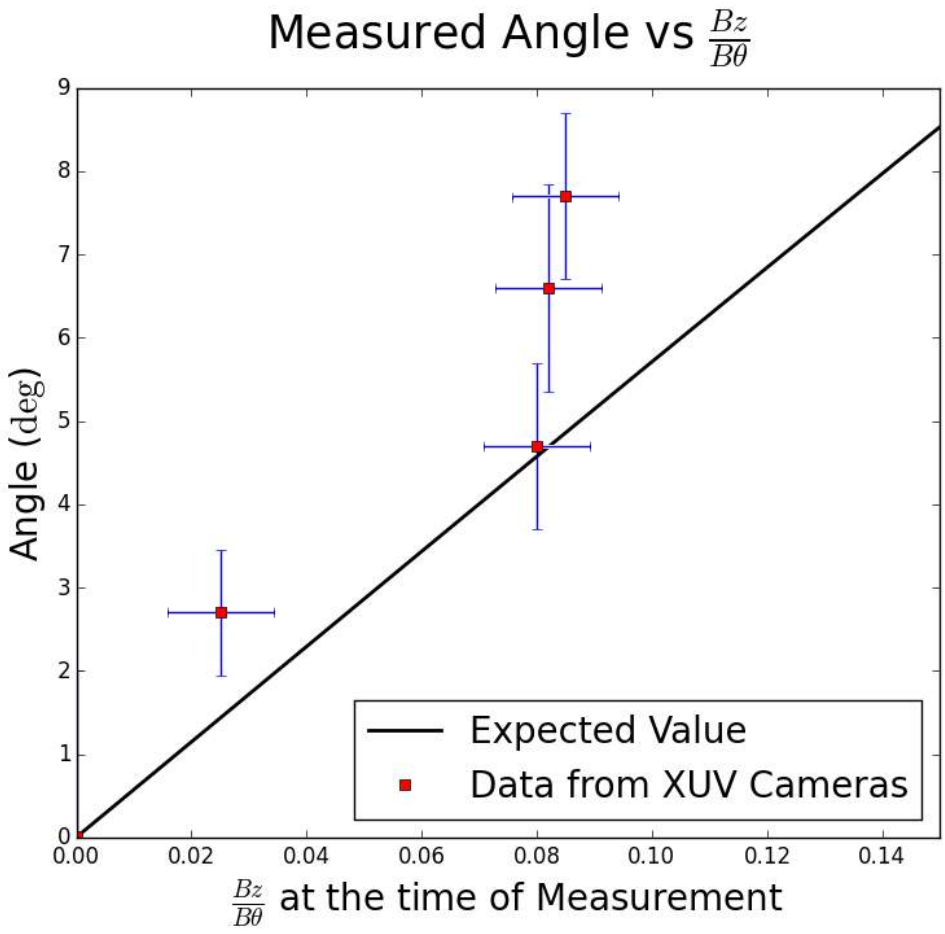

Figure 6.14: Plot of expected striation angle with respect to $\frac{B_z}{B_\theta}$, along with measured data points that relate the angles from the XUV images to $\frac{B_z}{B_\theta}$ at the time these images were taken. To determine the $\frac{B_z}{B_\theta}$ ratio, we assume B_z is that produced by the Helmholtz coil and B_θ is that calculated from $\frac{\mu_0 I}{2\pi r}$ at the liner's XUV self-emission surface.

Negative XUV images of 1.5 turn liner experiments are shown in Fig. 6.15. Noting that the current pulse penetration depth was significantly larger than the 4 or 8 μm liner thicknesses, we assume that the current flowed through the whole liner, not just an outer layer of it. The wavelengths of the striations on the single and double wrapped sides of the liner are the same. Moreover, we can see that while there is a hot vertical column of plasma near the seam, the

striations can be individually traced from one side of the plasma column to the other. The average angle changes across the seam. The angles highlighted in red in Fig. 6.15, which were determined using local transformation factors, change approximately from 12° to 8° in C3618 and from 11° to 14° in C3621. These changes are closer to upper limits; for the striations that we could trace through the seam with confidence, we measured changes between 1° and 4°. No matter the value of the change, the striations on the single wrapped side have an average stronger tilt than on the double wrapped side in both pulses. One possible explanation could be the following. First, since the current was flowing throughout the whole thickness of the liner, the effective mass and current area on the double wrap side were doubled. Initially, when the liner was cold and its resistivity low, the liner would be mainly driven by an inductive voltage, meaning that the total current would be evenly distributed azimuthally. The liner would then ohmically heat up, the single wrapped side heating faster due to its smaller mass. At the melting point, the resistive impedance would become comparable to the inductive impedance, meaning that more current would progressively shift to the double wrapped side. From this point on, the resistive impedance of the liner would be dominant and the total resistance on the double wrapped side would be less (true even when their resistivities are equal), leading to significantly more current flowing on the double wrapped side. This would lead to a higher B_θ on the outside of that section compared to the single wrapped section. This in turn would lead to an angle in the double wrapped section that is smaller than in the single wrapped section, which is observed. In reality there would probably also be complications added from the electrode contact effects discussed earlier.

We can determine the photon energy scale of our observed striations using

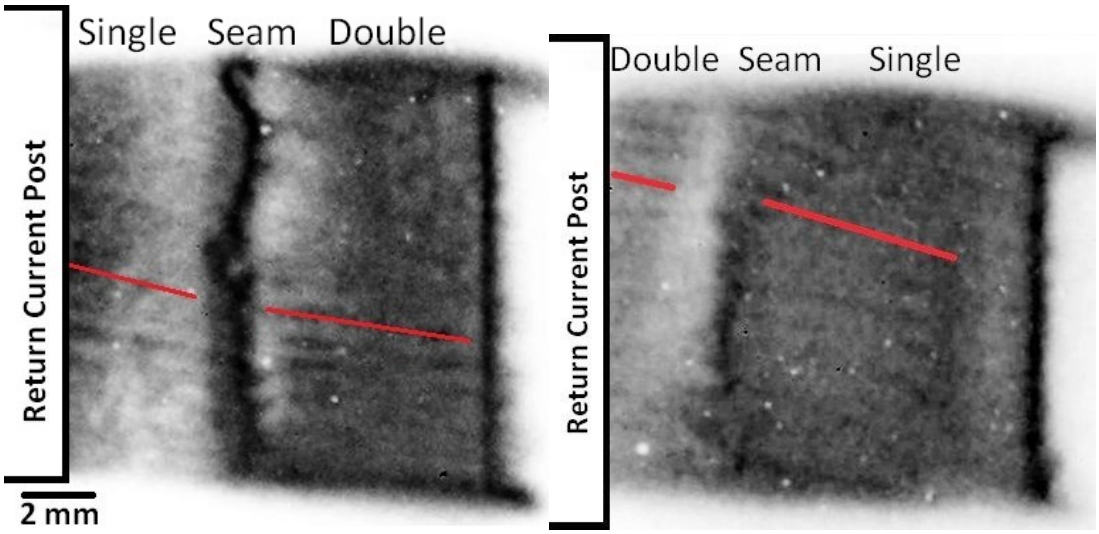

(a) C3618 - 170 ns (b) C3621 - 220 ns

Figure 6.15: Side-on XUV emission of COBRA pulses 3618 and 3621, having 1.5 and 1 T axially upwards applied fields respectively. The liners were half single half double wrapped liners. Their respective sides are marked on top of the images along with the location of the seam. Average tilt angles are shown in red. A return current post was blocking about 1/3 of the liner on the left side of each image, as shown.

the combined results of our 50, 100, and 200 μm diameter pinholes. A comparison between data from 50 μm and 100 μm pinholes is shown in Fig. 6.16.

The 100 μm pinholes gave the clearest images. It may be that our 200 μm pinholes, which did not show striations, did not have a high enough resolution and our 50 μm pinholes, which show the $\approx$ 0.5 mm features in a blurry manner, required too high an energy range for the liners to reach easily. By "reach easily", we are implying that a significant percentage of the radiation needs be emitted in a higher energy range so that it is not washed out by the diffractive blurring of the lower energy radiation. The minimum energy limit coming from diffraction considerations in pinhole cameras can be estimated using

$$y \approx \frac{1.22\lambda D}{d} \tag{6.3}$$

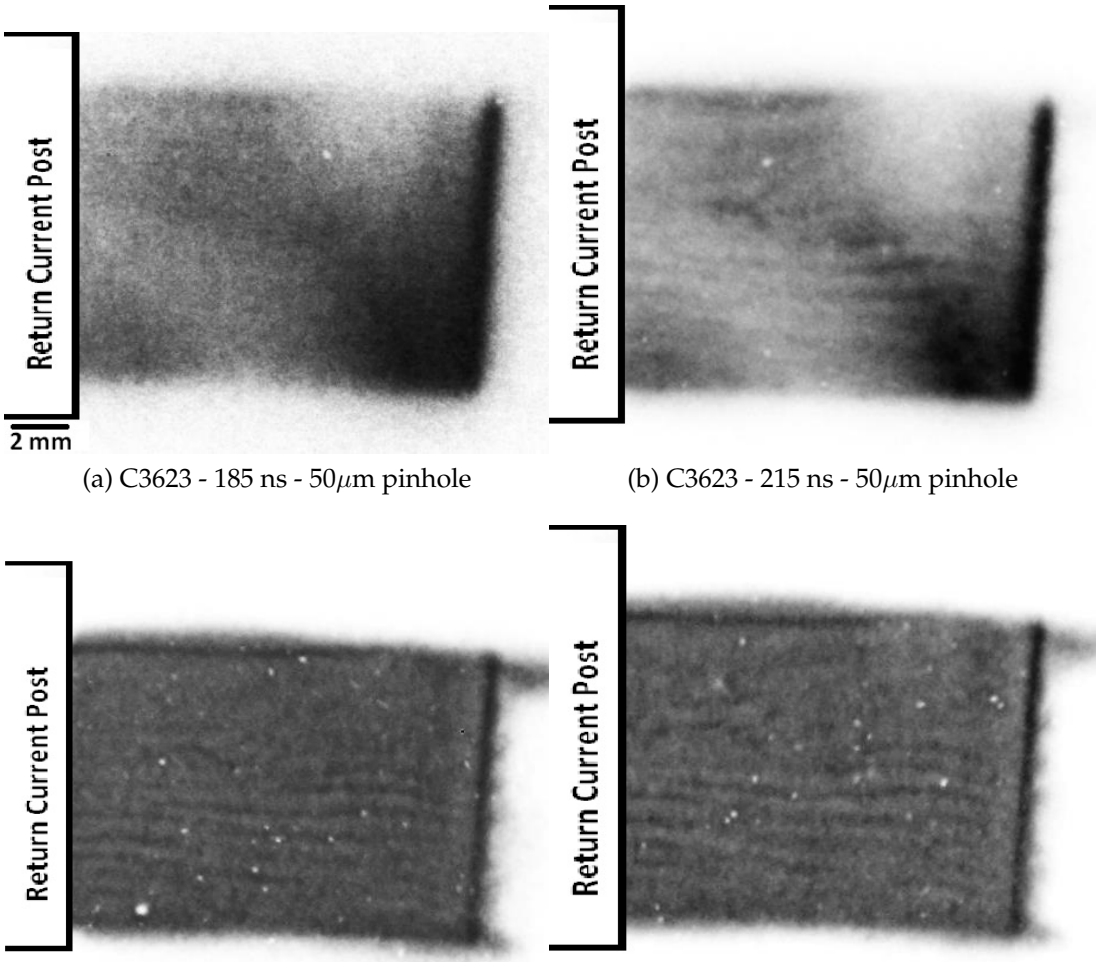

(a) C3623 - 185 ns - 50μm pinhole

(b) C3623 - 215 ns - 50μm pinhole

(c) C3623 - 195 ns - 100μm pinhole

(d) C3623 - 205 ns - 100μm pinhole

Figure 6.16: Time evolution of striations in the presence of a steady state axial magnetic field, using both 50μm pinholes and 100μm pinholes. A return current post was blocking about 1/3 of the liner on the left side of each image, as shown.

where y is the radius of the Airy disk minimum at the detector, λ is the wavelength, d is the pinhole diameter, and D is the distance from the pinhole to the detector. If 2y exceeds the resolution of interest, then wave diffraction through the pinhole is assumed to be too great to observe that feature. This gives a minimum energy limit of $\approx$ 50 eV for our 100 μm pinholes and $\approx$ 100 eV for our 50 μm pinholes. As the intensity of the features in Fig. 6.16 is blurry and/or fading for the 50 μm pinholes, we can estimate the radiation energy range of the

perceived features being somewhere near 50 - 100 eV.

6.3.4 Discussion

Even though the pattern looks similar on COBRA scale machines and Z, the mechanism responsible for this structure on the two machines may be different. There are a couple of proposed explanations for why the helical twist appears, both potentially correct depending on the parameters of the experiment. For example, using the PERSEUS extended MHD code, there is reason to believe that the helical structure is due to the current following a force-free path. This comes about from the Hall term $\frac{1}{n_e e}\boldsymbol{J} \times \boldsymbol{B}$ in the generalized Ohm's law which adds to the resistive term $\eta \boldsymbol{J}$. This increases the "effective resistance" in the $\boldsymbol{J} \times \boldsymbol{B}$ direction, which is perpendicular to $\boldsymbol{J}$. To minimize this, $\boldsymbol{J}$ can preferentially flow along $\boldsymbol{B}$, which has a helical twist, hence the label "force-free". Note that this assumes the Hall term is important compared to the resistivity term, which only holds for relatively low density plasmas. This also assumes the $\frac{B_z}{B_\theta}$ ratio is high enough to match the obseved tilt. As the applied B_z is too small in both COBRA and Z experiments, a field amplification mechanism is needed to explain the formation of the features. This mechanism is one reason why the helical structure observed on Z and COBRA may potentially be generated differently. On Z, there is significant low density plasma generated below the experimental load in the transmission line's feed section. Once this plasma is generated, it can sweep up onto the surface of the liner, compressing the B_z generated from the coil. However, on COBRA no such breakdown has been observed in the transmission line below the experimental load. Other possible field compression mechanisms at the surface of the liner on COBRA are not

evident.

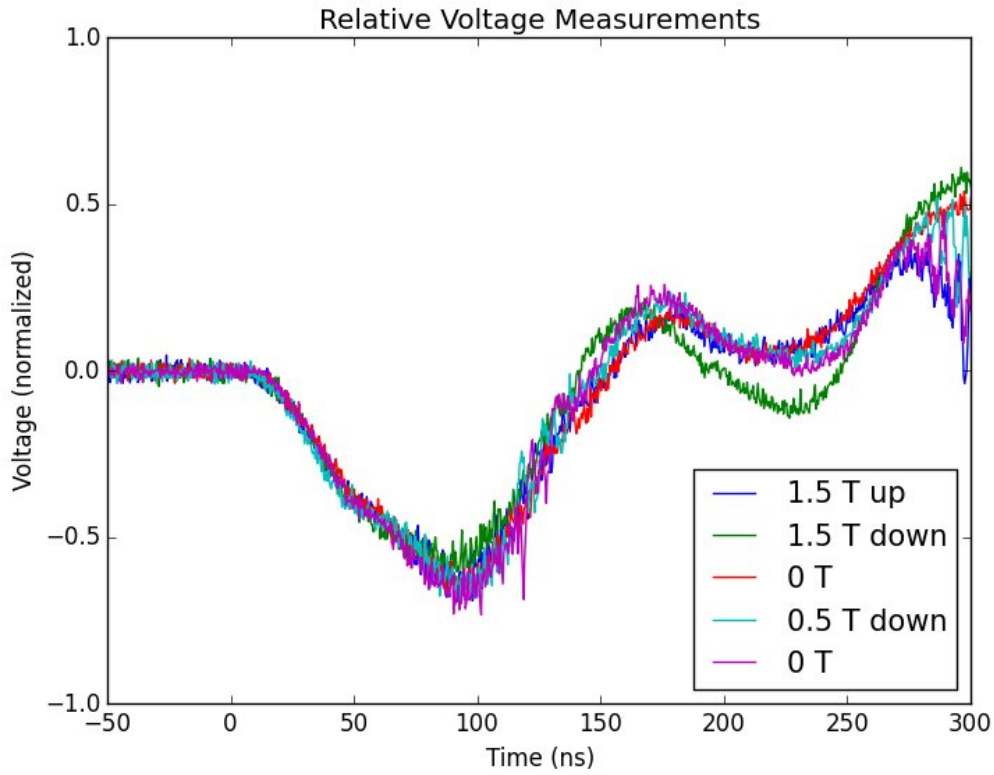

Figure 6.17: The voltage measurements in the load region show no significant difference in experiments with and without an axial field. The voltage waveforms shown are in arbitrary units, with the voltage at peak current estimated to be about 300 kV.

Furthermore, if the current path was indeed helical around the liner on COBRA, one might expect the inductance of the load to change when comparing a no applied axial field experiment to one with a field because of the different current paths. Consequently the voltage measured at the load should also be different. Figure 6.17 shows that the voltages in our experiments, with and without an axial applied magnetic field, do not change enough with respect to each other to draw such a conclusion.

A second explanation for the structure, which is applicable to COBRA ex-

periments, is given by Yager-Elorriaga *et al.*[18, 69] They performed side-on self-emission and shadowgraphy measurements on a 550 kA 150 ns rise-time machine. They argue that the helical pattern they observed is due to the kink m=1,2 modes, depending on the intensity of the applied axial magnetic field, and show agreement in their results within their error bars. Moreover, they display simultaneous optical self-emission and shadowgraphy data, which shows clear matching of the self-emission striation pattern with the spikes and bubbles. Using their data, they could also correlate the amplitude of the surface ripples with the self-emission contrast. These observations agree with results presented in section 6.3.1.

One possible hypothesis for the presence of XUV self-emission striations, both with and without an applied axial magnetic field, is that there is an inner hot surface in the liner that is emitting radiation, some of which the outer spikes are absorbing. Hence, striations in our XUV images appear due to more and less absorption occurring through the spikes and bubbles. To test for this possibility, PrismSPECT was used to determine the absorption characteristics of the plasma. While the structure with and without an applied magnetic field qualitatively changes, in both cases it displays a similar wavelength, similar self-emission intensity, a similar surface ripple amplitude, and matching of spikes and bubbles with the self-emission pattern. We will consequently assume that in both scenarios, the plasmas emitting and absorbing radiation are in the same energy and density range.

We can use our experimental data to help us determine these ranges of the plasma. First, as shown in section 6.3.3, the energy range of the features being observed is $\sim$ 50 - 100 eV from diffraction considerations. We will use that as

the energy of the radiating plasma. Regarding the absorbing plasma present in the spikes, we note from section 6.3.1 that it does not emit visibly in the XUV range, but it does in visible light. So let us assume a range of $\sim$ 10-50 eV for the plasma in the spikes (10 eV is the lowest energy that can be used in PrismSpect).

For a minimum density range estimate of the absorbing plasma, consider Fig. 6.18, which is the corresponding interferometry image of the shadowgraph in Fig. 6.8. Near the edges of the spikes, such as in the highlighted box, we can observe a fringe shift of 1-2 fringes. In order to estimate a density from this, we need to assume a path length. We know that our initial liner radius was 2.1 mm and the radii where fringes are visible span from $\sim$ 2.5 mm to $\sim$ 2.9 mm. Using the last two radii, we can determine that the path length varies from 0 to 1.5 mm, depending on the optical chord. We mainly care about the order, so we will use a 1 mm path length. Hence, for the 532 nm laser, 1-2 fringe shifts will correspond to an electron density of $4 - 8 \times 10^{18}$ cm^{-3}. Given the plasma temperature range, we can assume an ionization level Z = 5 - 10. This gives an ion density of $\sim 10^{18}$ cm^{-3} near the edges of the shadowgraph's ripples. We will use this as our minimum density approximation. For a maximum density range estimate, we can approximate by overshooting. If we assume the initial $\sim$ 10 μm thick Al foil expands into the 400 μm long spike region uniformly, then the density would be $\sim 10^{21}$ cm^{-3}. But since we know that the liner does not expand uniformly, that there is a high density region that does not expand more than a 100 μm or so as shown in Chapter 5, the spikes will in reality have a lower density than the average of $\sim 10^{21}$ cm^{-3}. We are then justified to use $\sim 10^{20}$ cm^{-3} as an upper density range.

Figures 6.19 (a) and (b) show simulation results from PrismSpect. (a) dis-

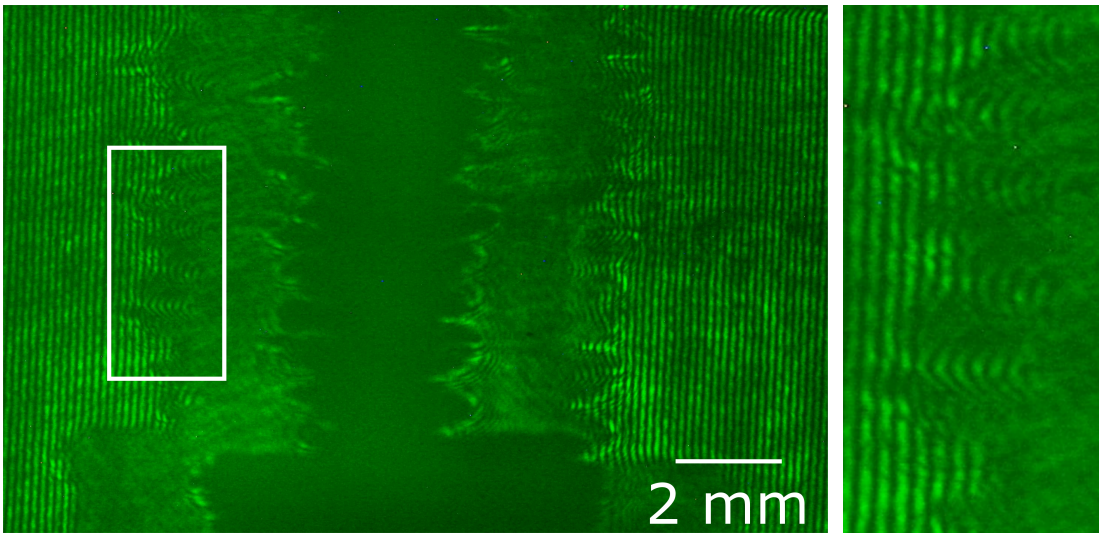

(a) (b)

Figure 6.18: (a) Interferometry image corresponding to the shadowgraph in Fig. 6.8 (b), taken at peak current in a 1.1 MA 110 ns rise-time COBRA pulse. (b) Zoomed-in view of the white box in (a).

plays a 100 eV black body radiation spectrum used in all the following PrismSpect simulations as the radiation source. (b) depicts the absorption spectrum of such radiation through 500 μm plasma at $\approx$ 17 eV and an ion number density of 10^{18} cm^{-3}. Figures 6.20 and 6.21 show absorption through 500 μm plasma at an ion number density of 10^{19} cm^{-3} and 10^{20} cm^{-3} respectively, each divided into two plots, one for an $\approx$ 17 eV plasma and another for an $\approx$ 46 eV plasma.

From these figures, we can see that there is strong absorption near the 90 - 100 eV radiation range through $\approx$ 17 eV and 10^{19} cm^{-3} plasma. The absorption also becomes significant across a large portion of the 50 - 100 eV radiation range of interest through $\approx$ 17 eV and 10^{20} cm^{-3} plasma. There is some absorption at 46 eV at this number density as well. To focus a little further on the 10^{19} cm^{-3} - 10^{20} cm^{-3} density range, Fig. 6.22 shows absorption through plasma at those densities at $\approx$ 33 eV. The main difference in the $<$ 100 eV radiation range between the $\approx$ 33 eV plasma and the $\approx$ 47 eV plasma is that at an ion density of

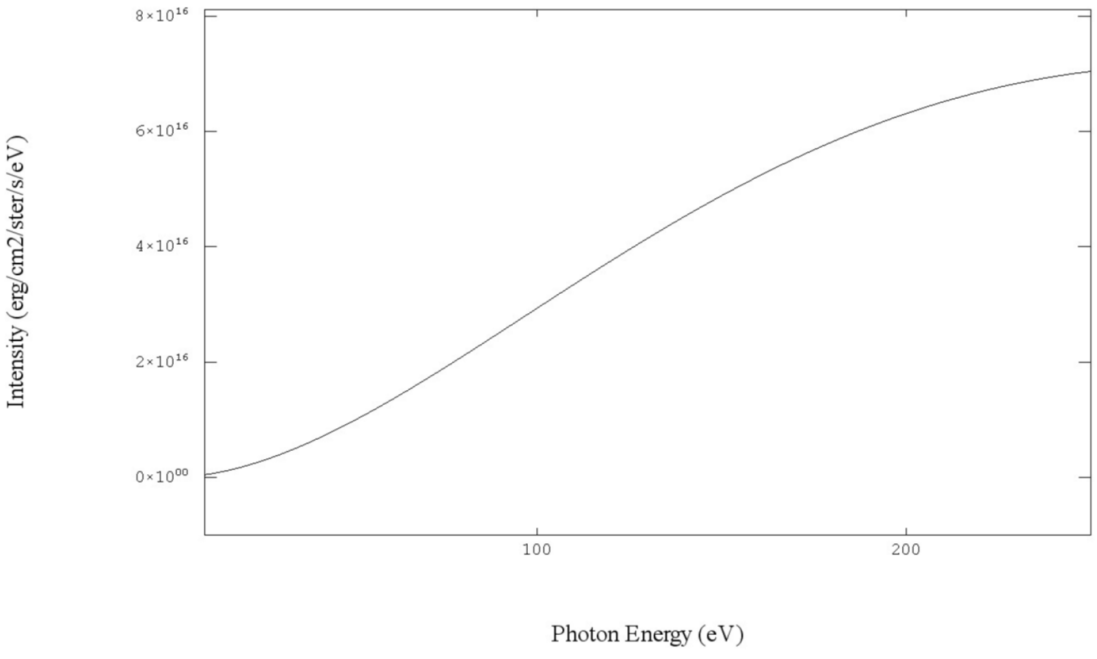

(a)

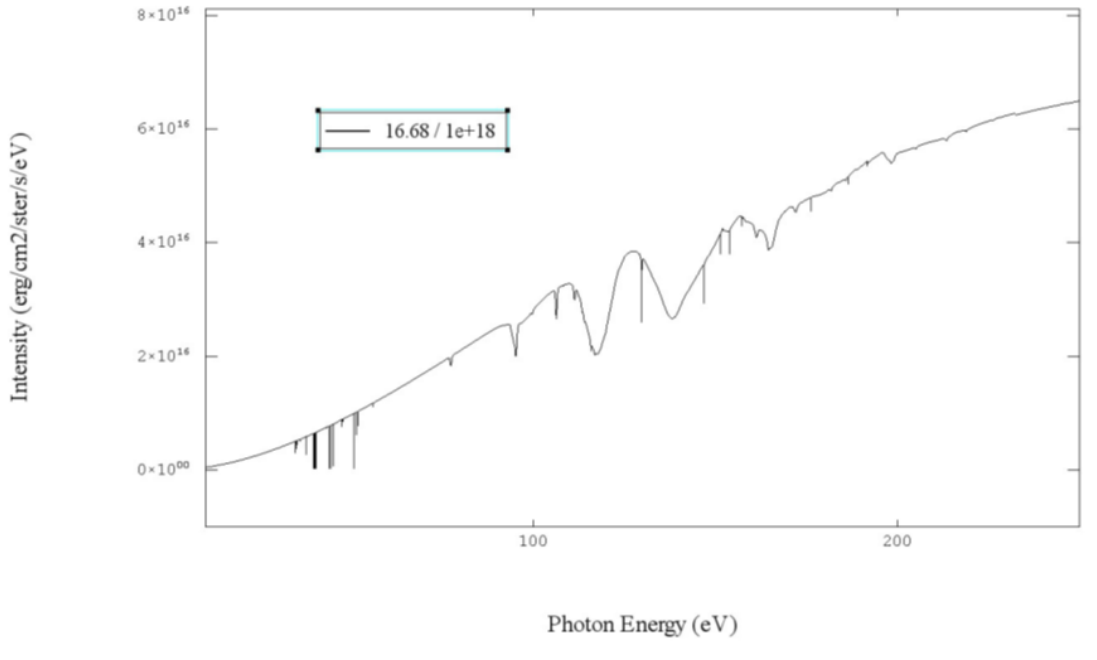

(b)

Figure 6.19: PrismSpect (a) 100 eV black body radiation curve and (b) absorption plot through 0.5 mm plasma at an ion temperature of 16.68 eV and a density of 10^{18} cm^{-3} using that 100 eV blackbody radiation source.

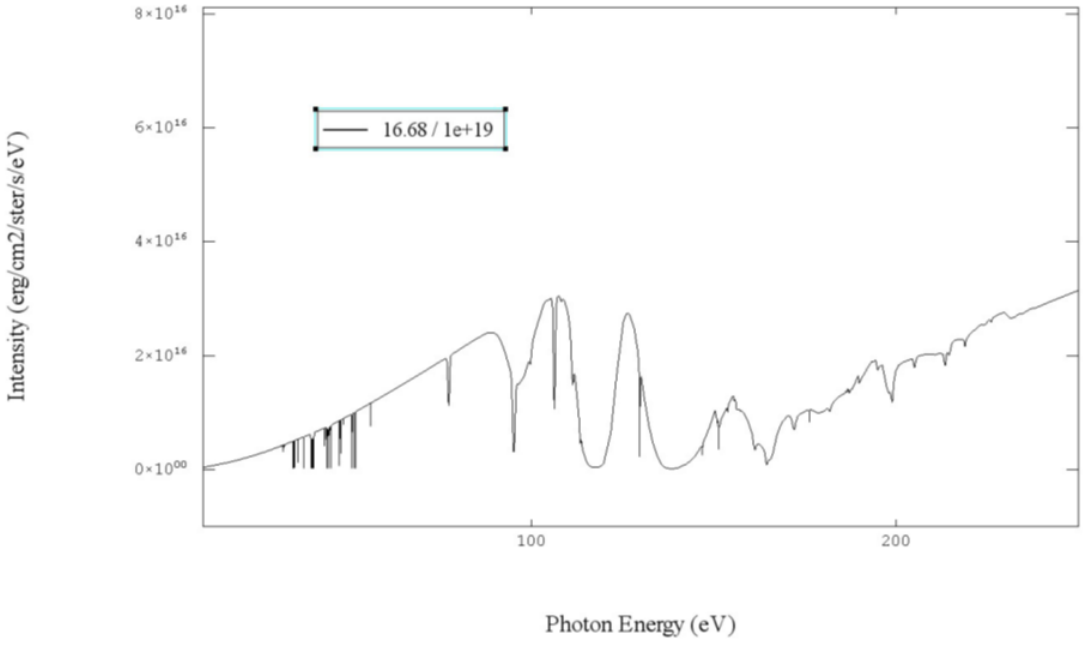

(a)

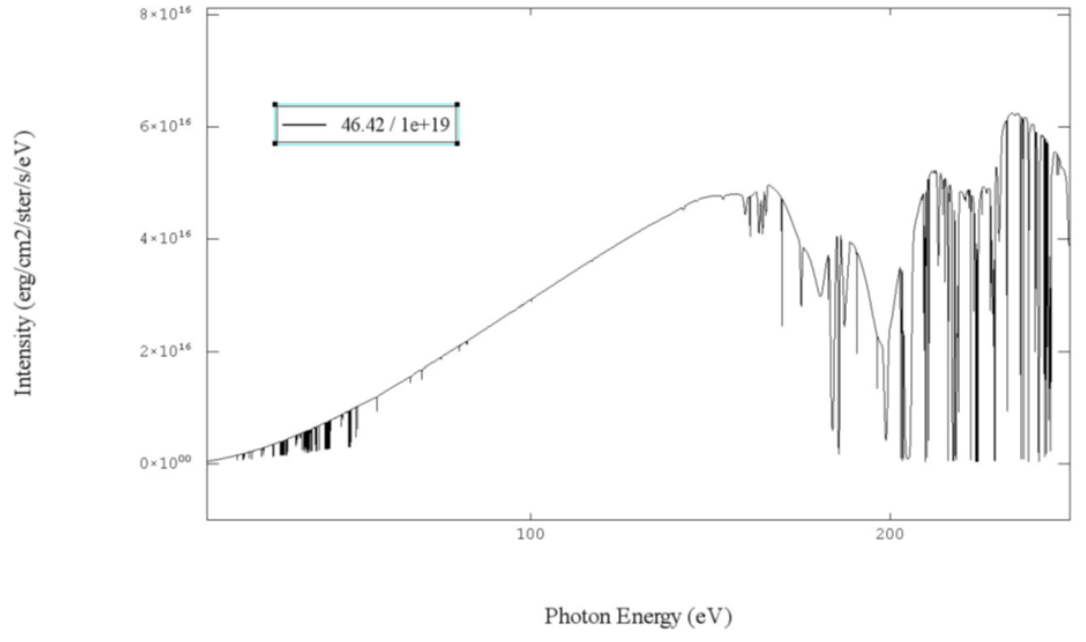

(b)

Figure 6.20: PrismSpect absorption plots through 0.5 mm plasma at an ion density of 10^{19} cm^{-3} and temperature of (a) 16.68 eV and (b) 46.42 eV using a 100 eV blackbody radiation source.

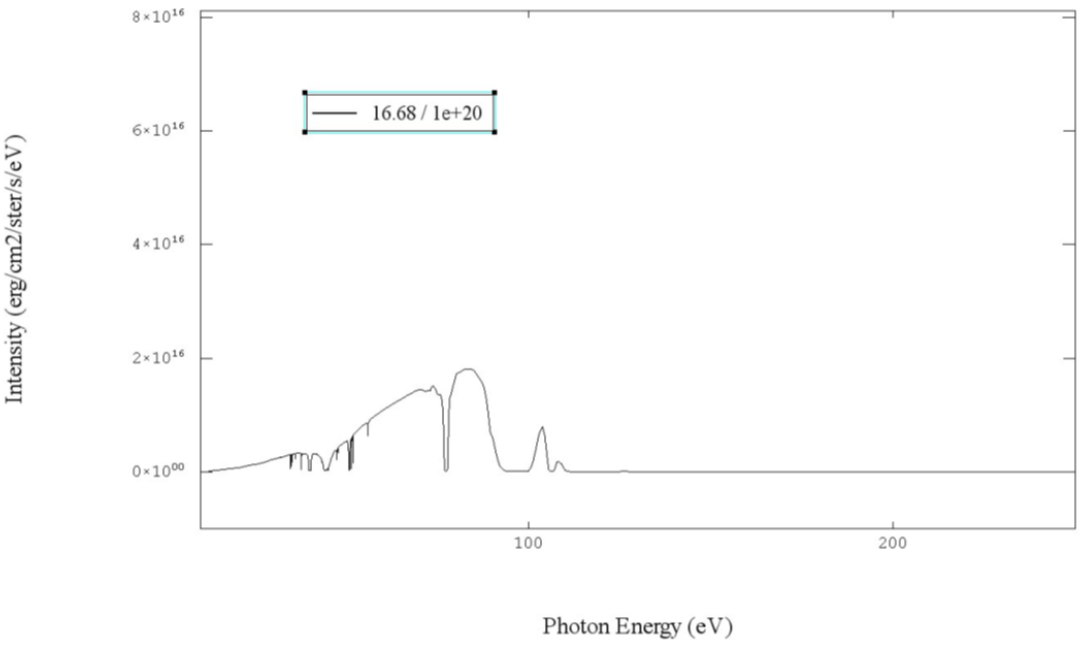

(a)

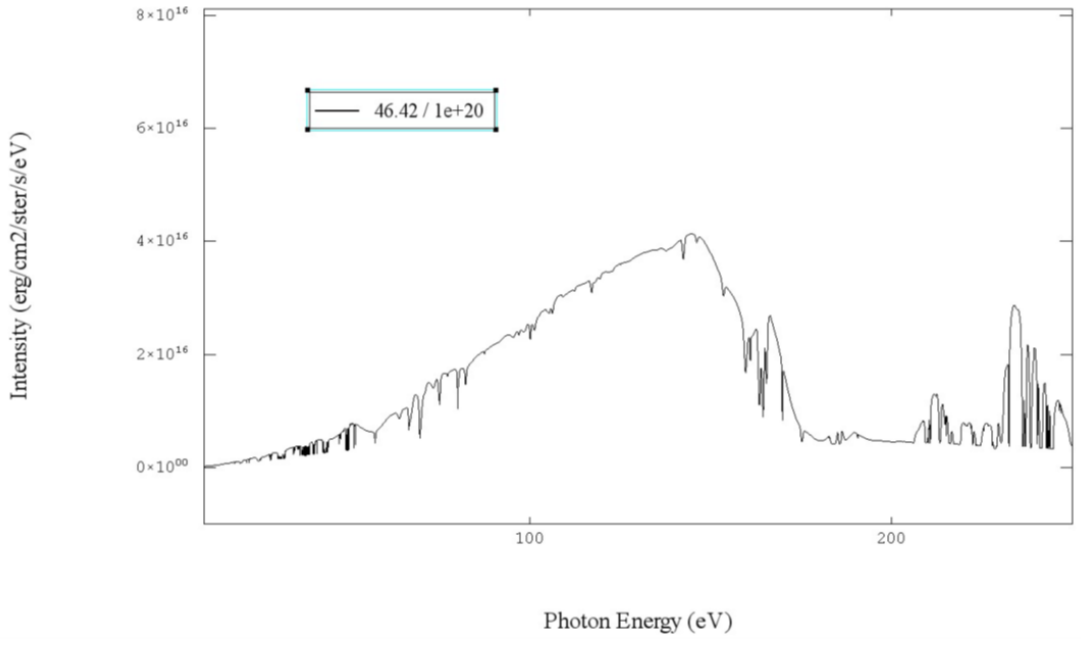

(b)

Figure 6.21: PrismSpect absorption plots through 0.5 mm plasma at an ion density of 10^{20} cm^{-3} and temperature of (a) 16.68 eV and (b) 46.42 eV using a 100 eV blackbody radiation source.

10^{20} cm^{-3}, the colder temperature plasma absorbs slightly more radiation.

Overall, PrismSpect simulation results show that within our range of interest, absorption through the spikes is a reasonable cause for the appearance of striations in the XUV cameras.

One last issue to address now is the cause of the horizontal structure formation in our experiments. A few explanations are considered here. First, the features are not caused by the classical sausage MHD instability. We can infer this from previous PERSEUS simulation results. These used a cartesian geometry without any magnetic field curvature. The features formed even though the plasma described was not prone to the classical m = 0 instability. Second, the features are not due to the MRT instability as that depends on an imploding liner, something our liners did not do. Possible explanations may come either from thermal pressure driving turbulent expansion or from Hall-related phenomena [70, 71, 72, 73]. Note that the Hall parameter for the spikes' estimated plasma parameters above is greater than 1.

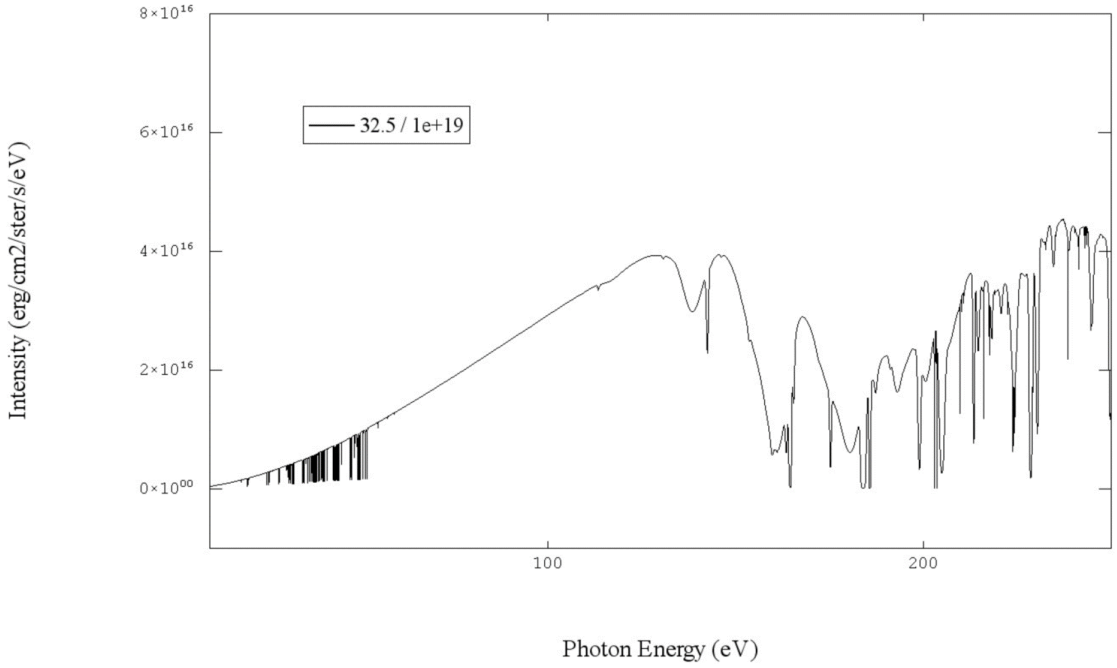

(a)

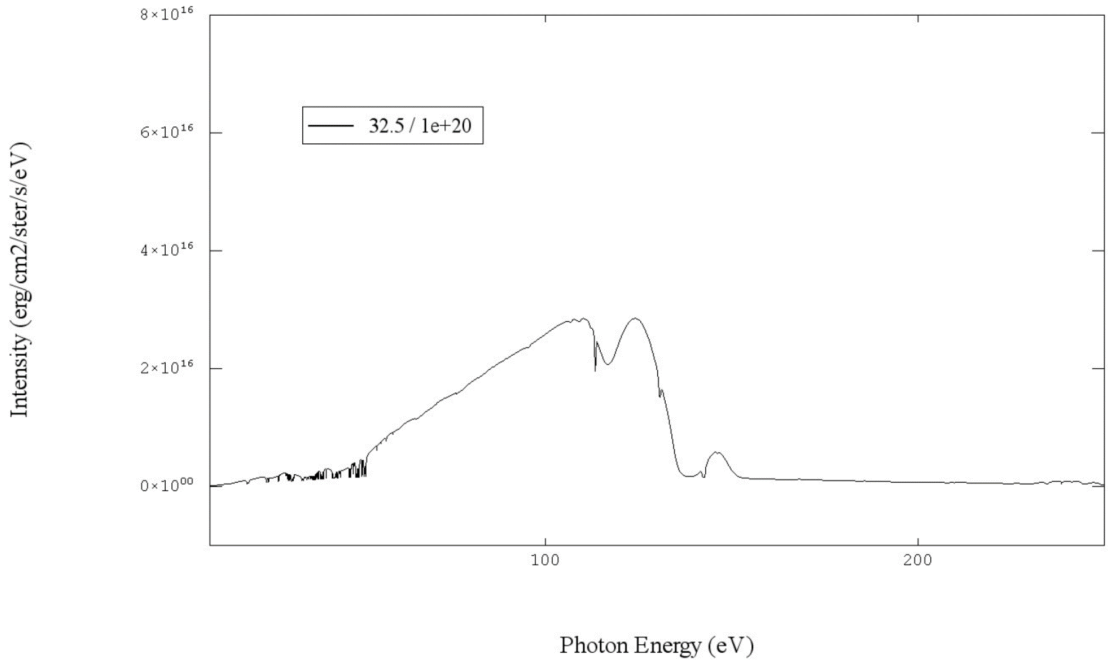

(b)

Figure 6.22: PrismSpect absorption plots through 0.5 mm plasma at an ion density of (a) 10^{19} cm^{-3} and (b) 10^{20} cm^{-3} and temperature of 32.5 eV using a 100 eV blackbody radiation source.

CHAPTER 7

CONCLUSION

MagLIF has a number of important physics issues related to efficient axial magnetic field generation, efficient laser preheat, implosion stability and minimal fuel-liner mix that need to be studied further. Reducing susceptibility to the MRT instability to improve implosion uniformity could be achieved by using thicker walls. But that comes at the expense of a lower implosion speed. If the MRT instability can be mitigated through other means, then thinner liner walls could be used with larger diameter liners. This could enable an increased velocity of the imploding liner, increasing the compression of the plasma. One could then expect to get a higher fusion yield. To help conceive possible MRT mitigation methods, we first focused on investigating the early-time micrometer scale structure that is believed to seed the subsequent MRT instability. Understanding how and why this structure forms can be used to diminish its development and to mitigate any ensuing instability that it seeds.

To study the development of micrometer scale structure, we first needed to optimize the X-pinch X-ray diagnostic for near-micrometer resolution measurements in cylindrical liner experiments. We compared images from two types of detectors, the SR image plate and the DR-50 film, demonstrating that using film is critical for the detection of the micrometer structure in Ti, Ni and Cu. This result is arguably due to the film being less sensitive than the image plate to the harder radiation ($\gtrsim 5$ keV), the source size of which is > 10 μm (at hard enough radiation even > 100 μm). As the features being observed were 10-20 μm, such a source size would cause a blurring of the structure on the detector.

We then analyzed the experimental results produced using this diagnostic.

Aluminum liners showed local areal density variation of up to 35 - 40 $\%$ and feature sizes between 17 and 25 μm. We showed that the feature size reduces in the order Al, Ni, Cu, Ti for comparable areal mass density foils. Since we were observing density variations at a time when non-linear effects may reasonably be expected to occur, any linear analysis that does not account for density perturbation should not be expected to correctly describe our observed structure. Consequently, it is not surprising that the linear electrothermal instability without density perturbation (nor motion) proposed in literature [50] does not quantitatively explain the observed features.

We observed that inhibiting the material's expansion from both sides leads to a density perturbation amplitude reduction of about 50 $\%$ and a wavelength reduction of up to 15 $\%$. Such an overall feature reduction can help mitigate the Magneto-Rayleigh-Taylor instability growth in any subsequent liner implosion [55], helping improve the performance of a liner implosion Z-pinch. We also investigated the effect of ingrained structure in Al foils. Orienting the structure's grooves perpendicular vs parallel to the current flow resulted in azimuthally correlated vs interspersed features with different local areal density variation for the two cases.

Our experimental results on micrometer-scale features can help validate EOS models used in computational codes, as well as test the inclusion of additional material properties deemed important to the development of the structure[6], resulting in a better treatment of the transition from cold metal to plasma. For example, we compared our results with simulation results using the PERSEUS code, which includes improved EOS and low-temperature resistivity models, and found good qualitative and quantitative agreement. Such validation will in

turn allow prediction of more accurate conditions at the time of plasma formation that start with a material at solid density and room temperature.

Moving on from these micrometer scale features, we also observed the development of near-millimeter scale features using self-emission detectors and laser imaging. In non-magnetized experiments, we observed a self-emission striation pattern that was correlated with the spikes and bubbles at the surface of the liner. The pattern grows in time, reaching a saturation wavelength of about 600 - 750 μm for Al. Furthermore, from experiments employing a slit, the pattern appears to be orthogonal to the expected current channels in the liner. We showed credible evidence that the self-emission striation pattern is caused by the absorption of radiation emitted from the liner's inner region through the spikes.

We have also observed a helical striation pattern in liners in the presence of an axial magnetic field from XUV self-emission. In the case of the twisted wires experiments, the pitch of the tilt matches within experimental error, admittedly large, with the axial to azimuthal magnetic field ratio inferred from $\dot{B}$ probes. Furthermore, we observed magnetic field inside the liner that cannot be explained via simple magnetic field diffusion. In experiments that used a Helmholtz coil, we observed a tilt in striations that stayed constant in time and that was not determined by the expected axial to azimuthal magnetic field ratio at the time of measurement. However, while the variation in tilt angle was significant in a given image, there was correlation between average tilt angle and applied field strength.

Based on the work in this dissertation, there are a few interesting avenues for future work, both experimentally and computationally. First, we propose exam-

ining the micrometer-scale features on XP and COBRA using different materials in a flat foil geometry. For example, in preliminary experiments on XP, graphene appeared to be fairly resistant to the growth of these features. Testing graphene on COBRA would be a natural next step in order to observe the growth of the features at higher energies. Note that a flat foil geometry allows investigating these features with a setup that is easier to load. A flat foil also allows the load to contact the electrodes better, resulting in more repeatable initial conditions of the experiment. Second, within the range of physical regimes that PERSEUS has been shown to simulate reliably, which now includes the low-temperature high density regions, we can use the code to investigate regions of interest that are not measurable experimentally, especially those related to the micrometer-scale features. One such example was given in Chapter 5.

Finally, as a next step regarding the helical features on COBRA, one can experimentally determine whether these features are associated with an earlier-time phenomenon, such as melting, vaporization or initiation, by changing the material. Specifically, we propose changing it from Al to Ti as the resistivities of these, and hence their time to melting, vaporization and initiation, are significantly different. If the helical angle is indeed "locked-in" due to phenomena occurring at those times, one will observe a measurable change in angle.

APPENDIX A

HELICAL PLASMA STRIATIONS IN LINERS IN THE PRESENCE OF AN EXTERNAL AXIAL MAGNETIC FIELD

Helical Plasma Striations in Liners in the Presence of an External Axial Magnetic Field

L. Atoyan,[1] D. A. Hammer,[1] B. R. Kusse,[1] T. Byvank,[1] A. D. Cahill,[1] J. B. Greenly,[1] S. A. Pikuz,[1, a)] and T. A. Shelkovenko[1, a)]
Laboratory of Plasma Studies, Cornell University, Rhodes Hall, Ithaca, NY, 14853

Awe *et al.* found on the 20 MA Z machine [Acta Phys. Pol. A **115**, 956, (2009)] that applying an externally generated axial magnetic field to an imploding liner leads to a helical pattern in the liner when viewed with soft x-ray radiography [Phys. Rev. Lett **111**, 235005, (2013)][Phys. Plasmas **21**, 056303, (2014)]. Here we show that this phenomenon is also observed in extreme ultraviolet self-emission images of 10 mm long cylindrical metal liners having varying diameters and varying wall thicknesses on a 1 MA, 100-200 ns pulsed power generator. The magnetic field in these experiments is created using either twisted return current wires positioned close to the liner, generating a time-varying B_z, or a Helmholtz coil, generating a steady-state B_z.

I. INTRODUCTION

Recently, the MagLIF magneto-inertial confinement fusion concept[1] has attracted interest as an approach to achieving inertial confinement fusion, and preliminary results are encouraging[2]. In these experiments, a cylindrical current carrying tube, referred to as a liner, containing a preheated plasma is compressed by imploding the liner in a time of the order of 100 ns. An axial magnetic field is applied to provide thermal insulation between the hot plasma and the imploding liner. In experiments without an applied field conducted on the 20 MA Z machine[3] at Sandia National Laboratories, an interesting observation in soft X-ray radiographs was the formation of horizontal striations perpendicular to the current flow in the imploding liner. Peterson, Sinars *et al.* proposed that these striations were formed early in the current pulse due to an electrothermal instability initiated in the condensed matter states, which later acted as a seed for the Magneto-Rayleigh-Taylor instability[4]. Similar striations have also been observed on the 1 MA Cornell Beam Research Accelerator (COBRA) with a gated extreme ultraviolet (XUV) imaging diagnostic[5].

In order to mitigate these instabilities, thick dielectric coatings were applied to the surface of the liner in experiments on Z reported by Peterson, Awe *et al.*[6] Furthermore, applying an external axial magnetic field was shown to tilt these striations, giving them a helical pattern when viewed with soft X-ray radiography[7,8]. Figure 1 shows sketches of how the striations in the liner appear from a side view. A thin-shell model analysis was later applied to give a theoretical picture of the evolution of helical perturbations[9].

In the experiments reported here, we have confirmed the formation of striations with and without an axial magnetic field. The principal diagnostic, a time gated XUV self-emission imaging system, was different from that used on the Z-machine and the experiments reported here have a factor of 20 less peak current. Our experiments, which used non-imploding liners, were carried out on the 1 MA COBRA machine[10] at Cornell University with 100 ns pulse rise time. A typical COBRA current pulse for all experiments related to our investigation is shown as a solid line in Fig. 2. The figure also shows two $\dot{B}$ traces which will be discussed in section III A. The two experimental arrangements that were used to generate the axial magnetic fields were significantly different. The first produced a time-varying and spatially non-uniform field by using twisted return current wires. The second produced a steady-state and spatially uniform field by using a Helmholtz coil. These will be described in detail in the following section. While we can confirm the helical morphology qualitatively, we cannot say anything definitive about the mechanism that generates the striations.

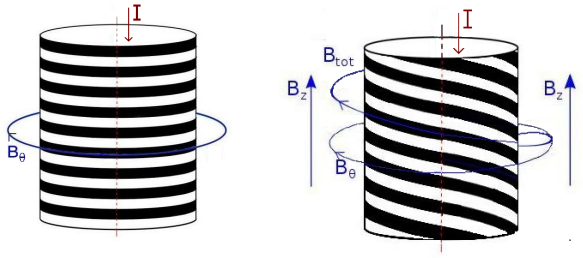

(a) (b)

FIG. 1. Idealized sketches of cylindrical liners showing striation patterns without (a) and with (b) an axial magnetic field. The quantity B_{tot} is the vector sum of B_z and B_θ, the azimuthal field due to I.

II. DIAGNOSTICS AND EXPERIMENTAL ARRANGEMENT

A. Diagnostics

The primary diagnostic system for monitoring the striations produced in the liner was a pair of XUV time gated

a)Permanent Address: P.N. Lebedev Physical Institute, Moscow, Russia

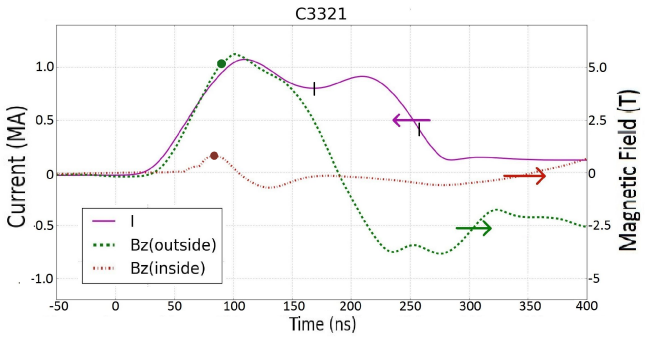

FIG. 2. A typical COBRA current waveform produced in our experiments is shown. The vertical lines on the current trace delimit the interval during which XUV images were taken. The experiment here corresponds to pulse C3321 which used the twisted return current wires configuration. Measured axial magnetic fields both inside and outside the liner are shown in dash-dotted and dotted lines respectively. The estimated probe failure time is depicted on each probe's trace as a circle. Color plots are available in the online version of this paper.

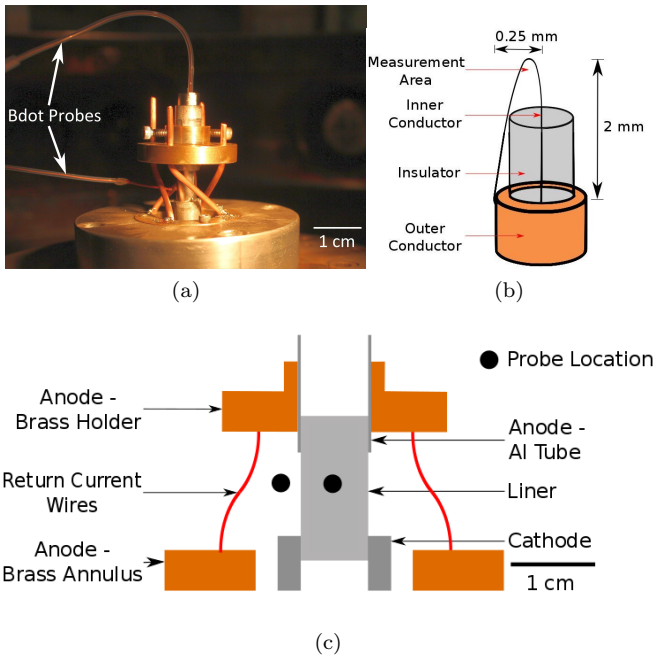

FIG. 3. (a) A photograph of the twisted return current wires experimental arrangement. Copper wires, 2.1 mm in diameter, placed at a distance of 12.7 mm from the center line of the liner, were rotated 90° either clockwise or counterclockwise. A $\dot{B}$ probe on the end of a solid coaxial cable was positioned in the center of the liner. Another was positioned approximately 2.5 mm outside the liner wall. (b) A sketch of these $\dot{B}$ probes. (c) A sketch of the hardware configuration without the probes. Note that the circles only depict the location, not the orientation, of the probes.

pinhole cameras positioned side-on and one opposite the other. While Awe's radiographs on Z looked through both sides of the liner in the same image, our images see only one side at a time as the liner is optically thick in the observed wavelength range. Each camera viewed the liner through four pinholes having a diameter of either 50, 100 or 200 μm, resulting in different energy sensitivities as discussed later in section III B. Each pinhole cast an image on a different quadrant of a microchannel plate. All four quadrant frames had an exposure time of either 5 or 10 ns, with exposures two through four delayed by 10, 20, and 30 ns respectively with respect to the first one. We refer to these devices as quad-cams. As there was no observable difference in the data from the 5 and 10 ns exposures, we will only be presenting data that used 10 ns exposures. In all of our experiments, these images were taken significantly after the pulse rise time, as shown in Fig. 2.

Magnetic fields were measured using micro $\dot{B}$ probes. Single loop probes, illustrated in Fig. 3(b), were placed outside the liner near its surface, as shown in Fig. 3(a) for the twisted return current wire experiments. Probes could be oriented to measure either axial or azimuthal magnetic fields. A probe was also placed on axis inside the liner, as shown in Fig. 3(a), to measure the axial field that penetrates through the liner.

B. Experimental Arrangement

1. Liner Configurations

Two designs were used for the liners. The first was the one-piece Al liner shown in Fig. 4. This liner was machined down to its final profile from an Al rod. The wall thickness of the liner tube shown in Fig. 4(a) was 50 μm. The bottom part of the piece was threaded so that it could be screwed into the brass cathode base, as shown in Fig. 4(a). The length of the tube, measured between anode and cathode, was 1 cm and the inner diameter of the liners was 4 mm.

The second design consisted of a 4 μm thick Al foil wrapped into a cylinder with one or two turns. This was similar to the design used in the liner instability studies previously done on COBRA[11]. The cylindrical foil was placed inside a tube holder by sliding it through a hole in the anode into the bottom holder, which was the cathode, as shown in Fig. 3. Contact was made by the liner on the holder walls. The liners in this design were also 1 cm in length and were 4, 8, or 16 mm in inner diameter.

Different diameters enabled a variation in the azimuthal magnetic field, B_θ, on the surface of the liner produced by the 1 MA current pulse flowing through it. The azimuthal field is given by

$$B_\theta = \frac{\mu_0 I}{2\pi r} \tag{1}$$

where r is the radius of the liner, μ_0 is the free space magnetic permeability and I is the current.

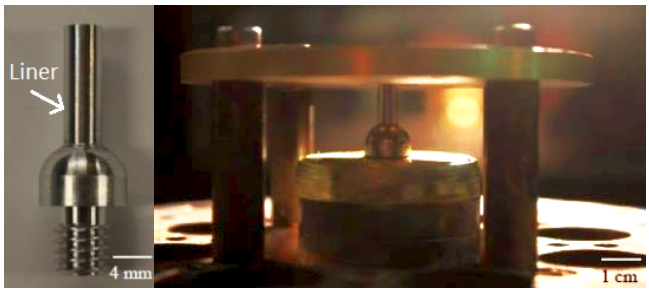

(a) (b)

FIG. 4. The one-piece liner, consisting of a threaded section for mounting and a liner section, is shown in (a). The fully mounted design is shown in (b).

2. Straight Post and Twisted Return Current Wires Configurations

For experiments that did not require an externally applied axial magnetic field, straight return current posts were used, as shown in Fig. 4(b). The experimental results without a field shown below used liners of the first design, though we have also done experiments using the second design, with similar results. In experiments with applied B_z, it was important to reduce the self-generated B_θ from the liner in order to have a detectable striation tilt. Hence, for the twisted return current wires experiments we used 8 mm diameter liners. However, 50 μm thick liners with that diameter did not emit in the XUV wavelength. They were too massive and heated insufficiently. Thus, the experimental results from the twisted wires shown here were of the second design. They have an inner diameter of 8 mm and are double wrapped.

To produce an axial magnetic field in the configuration shown in Fig. 3, four 2.1 mm diameter copper wires placed inside four equally spaced holes, each a distance 12.7 mm from the center, carried the current between upper and lower anode plates. The upper anode section was rotated 90° by hand either clockwise or counterclockwise, and was at a height of 2.5 cm with respect to the lower section. Solder was applied at the connections between the copper wires and the brass holders. The part of the anode that touched the liner consisted of an Al tube that could slide freely inside the top brass holder, as shown in Fig. 3. This way, the configuration could be adjusted so that the liner was always 1 cm long before vacuum pump-down (between cathode and anode).

The possible disadvantages of this arrangement were the following. First, the rotation and concentricity of the Cu return current wires were determined only by eye. A more robust method for the rotation could be devised. However, the non-uniformity of the axial magnetic field at the liner due to a possible deviation from concentricity is much less significant than that due to there being only four twisted return current wires. This non-uniformity is visible in our data and will be discussed further in the results section. Second, the $\dot{B}$ probes used to measure the B_z field were positioned at varying locations around the liner. As the magnetic field from the return current wires is inherently non-uniform, $\frac{B_z}{B_\theta}$ is location specific. However, as we will be looking only at average ratios of the field components and comparing them to average striation tilt angles, the $\dot{B}$ measurements are still meaningful for qualitative comparison.

3. Helmholtz Coil Experimental arrangement

For the second experimental arrangement, a Helmholtz coil having a 150 μs rise time was used, which is considered steady-state on the time scale of the COBRA pulse. The spatial uniformity of the coil, with the load hardware included, was within 5% in the area of interest. This coil produced 0.5 T to 1.5 T axial magnetic fields depending on the driving capacitor bank voltage. A photograph of the coil with a loaded liner, along with a $\dot{B}$ probe on axis in the liner, is shown in Fig. 5(a).

Most liners used in the Helmholtz coil experiments were single wrapped of the second design, with an overlap region of 3-5 mm, and are shown in the sketch of Fig. 5(b). Some of these experiments used liners that were single wrapped on one side and double wrapped on the other side. We will refer to such liners as 1.5 turn liners. Experiments with the latter liners investigated what effects doubling the current path area might have on the striations.

The liners were 16 mm in diameter in all of the coil experiments. As mentioned before, the reason for the larger diameter was to reduce the azimuthal magnetic field produced by the machine current running through the liner. For a B_z of 1.5 T, the expected maximum azimuthal magnetic field strength at such a diameter is about 25 T, giving a minimum $\frac{B_z}{B_\theta}$ ratio of 0.06. If the helical pitch is determined by this magnetic field ratio, then the minimum pitch angle would be 3.4°.

At this point, let us define the average angle of striations as the projected average, measured via averaging straight lines drawn between the leftmost and rightmost ends of given striations in the images. Note that the measured average angles from our XUV images will be different from the real angles because we are looking at a 2-D representation of a 3-D cylindrical system. For a given striation, the vertical height change from one side to the other in both geometric systems is the same, but the horizontal distance changes from $2r$ to πr between these two systems. This changes the angle by a factor of $\frac{2}{\pi}$, as shown in Eq. 2.

$$\theta_{3D} \approx \frac{B_z}{B_\theta} = (\frac{y}{\pi r}) = \frac{2}{\pi}(\frac{y}{2r}) \approx \frac{2}{\pi}\theta_{2D} \qquad (2)$$

where θ is the angle in radians, y is the vertical delta, r is the radius of the liner, and a small angle approximation has been used.

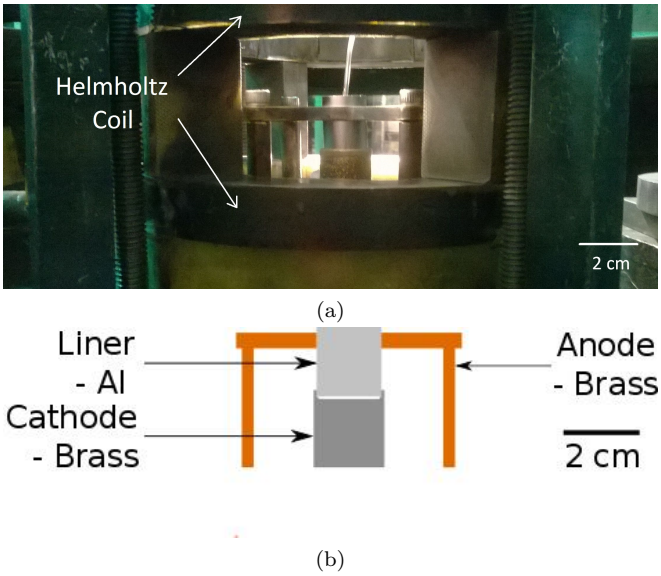

FIG. 5. Photograph and sketch of the Helmholtz coil experimental arrangement.

Using this, we note that the 3.4° will actually correspond to a 5.3° measured angle, which we should be able to detect in our XUV images. To avoid confusion, from now on all angles given will be the 3D angles that occur in reality as that is what is of interest. We also note that local angles will have their own transformation factors as $\frac{2}{\pi}$ is not appropriate when dealing with short sections of a striation. While most angles presented will be averages, we will explicitly point out when we talk about local angles.

III. EXPERIMENTAL RESULTS AND DISCUSSION

A. No Axial Field and Twisted Wires Results

Without an axial magnetic field, horizontal striations with deviation of up to ± 2° were observed in XUV self-emission, as shown in Fig. 6. Please note that all deviation values presented in this paper reflect the maximum change in angle and not a standard deviation. Also, all XUV images shown are "negatives", meaning that darker regions correspond to stronger emission and vice-versa. The no-field images are useful as controls for experiments with axial fields. The wavelength of the striations when comparing no applied field experiments with the alternative did not noticeably change: they all averaged 600 - 750 μm. While our liners do not implode, we believe that this wavelength is dominated by the Magneto-Rayleigh-Taylor instability in the ablated plasma, as the latter moves slightly in response to the radial forces.

Sample experimental results when the axial field was produced by the twisted return current wires are shown in Fig. 7. The difference between pulse C3317, corresponding to Fig. 7(a) and (b), and pulse C3318, corresponding to Fig. 7(c) and (d), is the direction of the axial magnetic field determined by the return current wire twist. C3318 is turned clockwise when viewed from above, similar to Fig. 3, producing an axially downward magnetic field at the liner's surface. The opposite is true for experiment C3317.

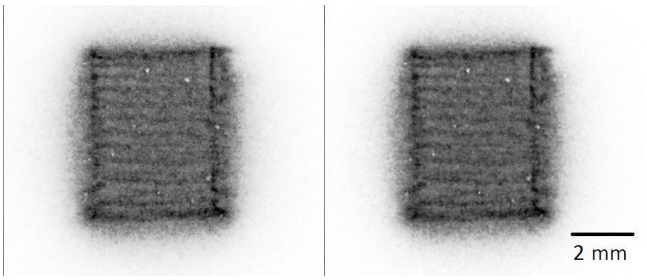

(a) C3170 - 210 ns (b) C3170 - 250 ns

FIG. 6. Side-on XUV emission from a 50 μm thick aluminum liner without an axial external magnetic field. The striations appear horizontal, with a pitch of 0 ± 2°. The time given for each image, in this and the following figures, represents the start of the 10 ns gate pulse with respect to the start of the current pulse, as shown in Fig. 2.

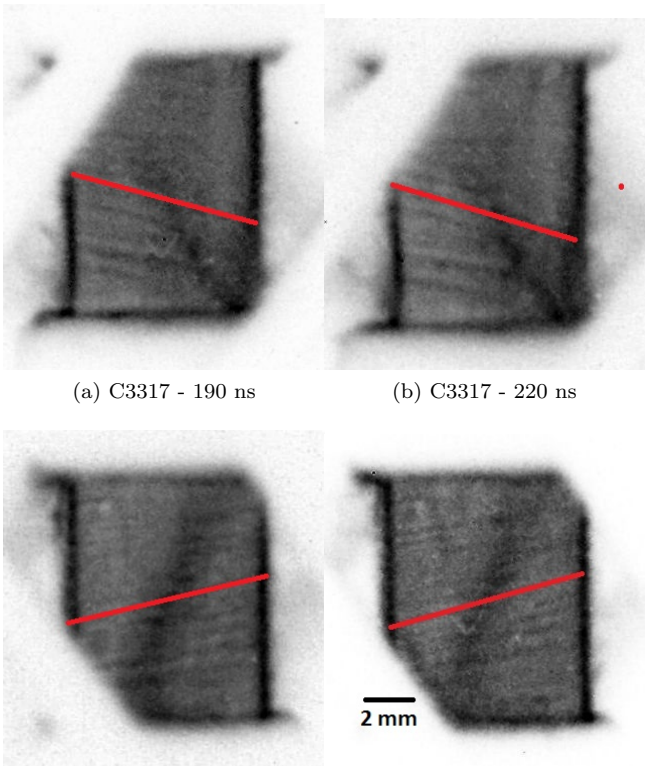

(a) C3317 - 190 ns (b) C3317 - 220 ns

(c) C3318 - 180 ns (d) C3318 - 210 ns

FIG. 7. Side-on XUV emission of COBRA pulses 3317 and 3318. C3317 had a counterclockwise twist in the anode section, producing an upwards axial magnetic field. C3318 had a clockwise twist similar to Fig. 3, producing a downwards field. One can see that the pitch does not change with time.

With four return current wires, the uniformity of the axial magnetic field at the liner radius, both azimuthally and axially, was poor. As a result, $\frac{B_z}{B_\theta}$ in the areas of the liner closer to the wires was stronger than elsewhere. However, a meaningful average pitch angle could still be measured from the images for both twist orientations: both cases averaged $8 \pm 1°$ in their respective directions. Considering the sources of error, this matches reasonably well with analysis using a combination of basic calculations of the expected B_θ field and data from $\dot{B}$ probes, as will be shown.

Fig. 3 shows the hardware configuration for the data used in the following discussion. According to the probe external to the liner, the maximum axial field strength measured roughly midway between anode and cathode axially, at the midpoint between two return current wires azimuthally, and 2.5 ± 0.5 mm radially outside the liner was 5.6 T (Fig. 2). As the return current wires were at an angle of approximately 45°, it is reasonable to assume that a similar strength azimuthal magnetic field due to a single wire was present. The current at this time is close to 1 MA. Note that the "single wire assumption" will introduce some error as the combination of four wires will reduce the measured B_θ whereas B_z contributions will add. To get the proper fields with the load hardware, a 3 dimensional simulation could be run. However, such a simulation would not be including magnetic field non-uniformities from current flow and plasma ablation dynamics, discussed in section III. Hence, the following discussion will be semi-quantitative instead as that is useful in illustrating all the factors that need to be taken into account in the twisted wire configuration.

In both twist orientation cases, the azimuthal field created by the wire currents will add to the B_θ generated by the current flowing through the liner. According to Eq. 1 which assumes azimuthal symmetry, the machine current flowing through the liner generates 31 T azimuthal magnetic field at the radius of the probe ($4 + 2.5 = 6.5$ mm) when the "axial" $\dot{B}$ probe reads 5.6 T. Using a superposition of azimuthal fields generated from the current running through the liner and the return current posts, the total azimuthal field at the location of the probe becomes 36.6 T. This $\frac{B_z}{B_\theta}$ ratio gives an angle of roughly 7°. However, this ratio is valid only near the probe and not at the liner surface.

We do expect a discrepancy between this $\frac{B_z}{B_\theta}$ and that measured from the XUV images. In general, this discrepancy is likely to have four sources: imprecise angle measurement due to spatial and temporal limitation of XUV camera resolution, the "single wire assumption", probe locations 2.5 mm exterior to the liner, leading to the axial and azimuthal field ratio being different at those locations compared to the ratio at the liner wall, and error in the location and orientation of the probes when placing them. If the striation tilt angle corresponds to $\frac{B_z}{B_\theta}$, then the last of these four sources is likely the most important and quite significant. It is reasonable to assume that the orientation of the probe relative to the z-axis may have an offset of up to 10°. This roughly corresponds to measuring 15% of the B_θ in the B_z measurement, giving an error bar of $\frac{\pm\Delta B_z}{B_z} = \pm 60\%$.

In addition to the tilted striations, a wide column of plasma can be seen in Fig. 7, stretching from the cathode to the anode at an angle of about 30° from the vertical. The source of that hot plasma is yet to be determined for certain, but it is likely due to the load hardware. It is not due to the presence of a seam in the liner as the quad-cams were positioned 180° from one another and both quad-cams saw such a plasma column.

Another measurement of interest in these experiments was the axial magnetic field inside the liner. An example is shown by the dash-dotted curve in Fig. 2 for pulse C3321. First, there is a time delay between the axial field outside the liner and that measured inside. This is to be expected as the field has to diffuse through the liner. However, when the field does appear inside the liner, it increases in two bursts rather than a smooth increase, as seen outside the liner. This suggests that the magnetic field does not penetrate through the liner via a simple field diffusion process. One possible explanation for the bursts could be magnetic flux compression via radially converging plasma ablated off the inside surface of the liner. It is possible that a wave reaches the inside surface of the liner and carries plasma from there radially inwards. The presence of converging shock waves inside thick liners has been studied recently by Burdiak *et al.*[12] In comparison with those experiments, the main differences in our experimental arrangement were that our liners were thin (8μm, which was significantly less than the pulse penetration depth), made out of double wrapped foil, and had no gas fill.

B. Helmholtz Coil Results

We also observed a tilt in striations in single wrapped foil experiments using the Helmholtz coil. Referring to Fig. 8, the orientation of the average tilt angle matches in orientation with the twisted wires experiments, i.e. left-handed twist for an upwards axial field and right-handed twist for a downwards applied field. The average angle shows some correlation with the applied axial field strength. In pulse C3626, in which a 0.5 T downward field was applied, the average is 3° whereas in pulse C3624, in which a 1.5 T field was applied, the average is 8°. Multiple measurements of the average angle in an image gave a maximum variation between 0.75° and 1.25° from the averages given above. Note however that local variations in tilt are not reflected in the average value and can be significant. This variation is present both azimuthally and axially along the liner, as shown in Fig. 8. For example, the angles of the highlighted striations in C3624 shown in Fig. 8(b) and determined using local transformation factors change from 6° to 18°.

C3623 stands out as an exception. That experiment had a 1.5 T applied field upwards producing the striations

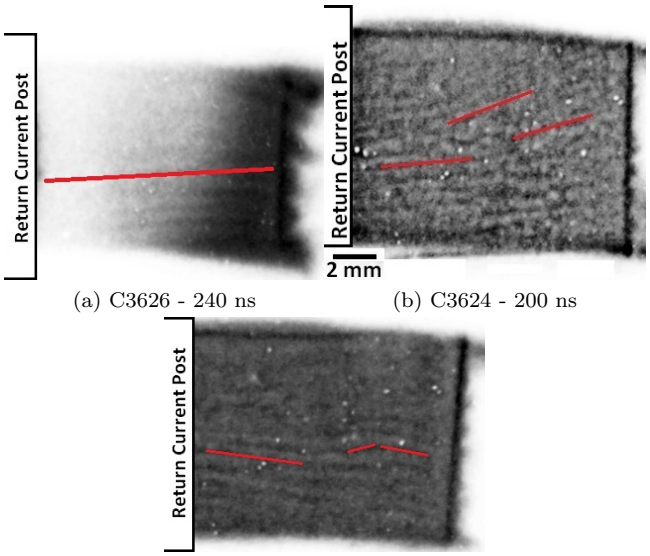

(a) C3626 - 240 ns (b) C3624 - 200 ns

(c) C3623 - 205 ns

FIG. 8. Side-on XUV self-emission images from COBRA pulses 3626, 3624, and 3623 having 0.5 T downwards, 1.5 T downwards and 1.5 T upwards axially applied fields respectively. A return current post was blocking about 1/3 of the liner on the left side of each image, as shown. The liners were single wrapped and specific striation tilts discussed in the main text are highlighted in red.

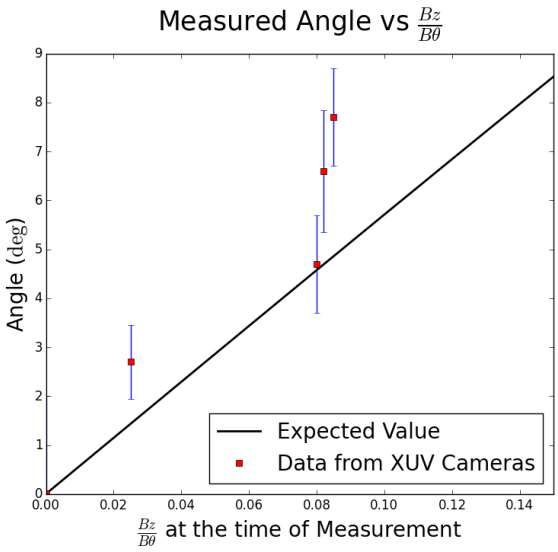

FIG. 9. Plot of expected striation angle with respect to $\frac{B_z}{B_\theta}$ at the surface of the liner, along with measured data points that relate the angles from the XUV images to $\frac{B_z}{B_\theta}$ at the time these images were taken. The horizontal error bars are small enough that they are within the red squares.

shown in Fig. 8(c). The average angle is 4.7 ± 1 °. However, a small section of the striations are tilted in the opposite direction from the average angle orientation. Since the magnetic field was applied only in one direction, this suggests that either the striations observed are not determined purely by the magnetic field ratio, or that there was azimuthal non-uniformity in the current distribution in the liner such that the twisting of the current channels produced oppositely directed B_z fields. Bott-Suzuki, Cordaro, *et al.* showed that vacuum gaps at contacts can cause non-uniform current flow with an azimuthal magnetic field variation of up to 50% that persists along the liner[13]. While we did not introduce vacuum gaps on purpose, there were bound to be contact gaps at the electrodes in our wrapped liner hardware. Hence, we think it is possible that there was a non-uniform azimuthal and axial current distribution, at least in that particular liner, that persisted throughout the pulse. Such non-uniformity could also explain why there is a large angle variation in the tilts at a given time and why we see larger angle variations in the Helmholtz experiments, where the field is uniform, than in the twisted return current wire experiments. We know from optical self-emission images that the larger diameter liners used in the former experiments created more non-uniform plasma from contact arcs, which would lead to more pronounced current non-uniformity.

We can determine the photon energy scale of our observed striations using the combined results of our 50, 100, and 200 μm diameter pinholes. Only the 100 μm pinholes gave clear images. It may be that our 200 μm pinholes, which did not show striations, did not have a high enough resolution and our 50 μm pinholes required too high an energy range for the liners to reach easily. The second limitation in pinhole cameras comes about from diffraction, which we can estimate using

$$y \approx \frac{1.22\lambda D}{d} \tag{3}$$

where y is the radius of the Airy disk minimum at the detector, λ is the wavelength, D is the pinhole diameter, and d is the distance from the pinhole to the detector. If y exceeds the size of the image, then wave diffraction through the pinhole is assumed to be too great to observe a liner image. Using this estimate, the striations shown in this paper are limited to the energy range of 20 to 40 eV.

In all our experiments the tilt angle stayed constant in time, within the angle variations described above. This in itself does not confirm that the striation angle is a locked in behaviour starting at a certain time or disprove that the striations continuously follow the changing magnetic field lines as the images were taken at nearly constant current, hence nearly constant B_θ. However, the angles measured do not correspond to the angles one would expect from the $\frac{B_z}{B_\theta}$ at the times of measurement, as shown in Fig. 9. The measured angles are higher, corresponding to a higher $\frac{B_z}{B_\theta}$ and suggesting that these angles were locked in earlier in time, when the B_θ was lower.

Negative XUV images of 1.5 turn liner experiments are shown in Fig. 10. Noting that the current pulse penetration depth was significantly larger than the 4 or 8

μm liner thicknesses, we assume that the current flowed through the whole liner, not just an outside layer of it. The wavelengths of the striations on the single and double wrapped sides of the liner are the same. Moreover, we can see that while there is a hot vertical column of plasma near the seam, the striations can be individually traced from one side of the plasma column to the other. The average angle changes across the seam. The angles highlighted in red in Fig. 10, which were determined using local transformation factors, change approximately from 12° to 8° in C3618 and from 11° to 14° in C3621. These changes are closer to upper limits; for the striations that we could trace through the seam with confidence, we measured changes between 1° and 4°. No matter the value of the change, the striations on the single wrapped side have an average stronger tilt than on the double wrapped side in both pulses. One possible explanation could be the following. First, since the current was flowing throughout the whole thickness of the liner, the effective mass and current area on the double wrap side were double. Initially, when the liner was cold and its resistivity low, the liner would be mainly driven by an inductive voltage, meaning that the total current would be evenly distributed azimuthally. The liner would then ohmically heat up, the single wrapped side heating faster due to its smaller mass. At the melting point, the resistive impedance would become comparable to the inductive impedance, meaning that more current would progressively shift to the double wrapped side. From this point on, the resistive impedance of the liner would be dominant and the total resistance on the double wrapped side would be less (true even when their resistivities are equal), leading to significantly more current flowing on the double wrapped side. This would lead to a higher B_θ around that section compared to the single wrapped section. This in turn would lead to an angle in the double wrapped section that is smaller than in the single wrapped section, which is observed. In reality there would probably also be complications added from the electrode contact effects discussed earlier.

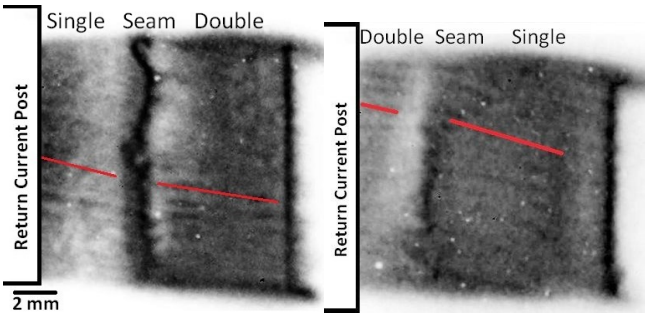

(a) C3618 - 170 ns (b) C3621 - 220 ns

FIG. 10. Side-on XUV emission of COBRA pulses 3618 and 3621, having 1.5 and 1 T axially upwards applied fields respectively. The liners were half single half double wrapped liners. Their respective sides are marked on top of the images along with the location of the seam. Average tilt angles are shown in red. A return current post was blocking about 1/3 of the liner on the left side of each image, as shown.

IV. SUMMARY AND CONCLUSION

We have observed a helical striation pattern in liners in the presence of an axial magnetic field from XUV self-emission. In the case of the twisted wires experiments, the pitch of the tilt matches within experimental error, admittedly large, with the axial to azimuthal magnetic field ratio inferred from $\dot{B}$ probes. Furthermore, we observed magnetic field inside the liner that cannot be explained via simple field diffusion. In the case of the Helmholtz coil experiments, we observed a tilt in striations that stayed constant in time. Even though the variation in tilt angle was significant in a given image, there was correlation between average tilt angle and applied field strength. Also, the combined data from single wrapped liners and 1.5 turn liners suggests current non-uniformity exists in single thickness liners.

V. ACKNOWLEDGMENTS

This research was supported by the National Nuclear Security Administration Stewardship Sciences Academic Programs under Department of Energy Cooperative Agreement DE-NA0001836, as well as by the National Science Foundation Grant number PHY-1102471. The authors would like to thank Pierre Gourdain, Harry Wilhelm, Todd Blanchard, Daniel Hawkes and William Potter for their excellent technical support. We would also like to thank the very careful anonymous reviewer of our manuscript whose comments and suggestions substantially improved the final manuscript.

[1] S. A. Slutz, M. C. Herrmann, R. A. Vesey, A. B. Sefkow, D. B. Sinars, D. C. Rovang, K. J. Peterson, and M. E. Cuneo, Physics of Plasmas **17**, 056303 (2010).

[2] M. R. Gomez, S. A. Slutz, A. B. Sefkow, D. B. Sinars, K. D. Hahn, S. B. Hansen, E. C. Harding, P. F. Knapp, M. C. Herrmann, M. H. Hess, O. Johns, D. C. Lamppa, M. R. Martin, and R. D. Mcbride, **155003**, 1 (2014).

[3] M. K. Matzen, B. W. Atherton, M. E. Cuneo, G. L. Donovan, C. A. Hall, M. Herrmann, M. L. Kiefer, R. J. Leeper, G. T. Leifeste, F. W. Long, G. R. Mckee, T. A. Mehlhorn, J. L. Porter, L. X. Schneider, K. W. Struve, W. A. Stygar, and E. A. Weinbrecht, Acta Physica Polonica A **115**, 956 (2009).

[4] K. J. Peterson, D. B. Sinars, E. P. Yu, M. C. Herrmann, M. E. Cuneo, S. A. Slutz, I. C. Smith, B. W. Atherton, M. D. Knudson, and C. Nakhleh, Physics of Plasmas **19**, 092701 (2012).

[5] L. Atoyan, T. Byvank, A. D. Cahill, C. L. Hoyt, P. W. L. de Grouchy, W. M. Potter, B. R. Kusse, and D. A. Hammer, Proc. 9th Int. Conf. on Dense Z Pinches **67**, 67 (2014).

[6] K. J. Peterson, T. J. Awe, E. P. Yu, D. B. Sinars, E. S. Field, M. E. Cuneo, M. C. Herrmann, M. Savage, D. Schroen, K. Tomlinson, and C. Nakhleh, Physical Review Letters **112**, 135002 (2014).

[7] T. Awe, R. McBride, C. Jennings, D. Lamppa, M. Martin, D. Rovang, S. Slutz, M. Cuneo, A. Owen, D. Sinars, K. Tomlinson, M. Gomez, S. Hansen, M. Herrmann, J. McKenney,

C. Nakhleh, G. Robertson, G. Rochau, M. Savage, D. Schroen, and W. Stygar, Physical Review Letters **111**, 235005 (2013).

[8] T. J. Awe, C. A. Jennings, R. D. McBride, M. E. Cuneo, D. C. Lamppa, M. R. Martin, D. C. Rovang, D. B. Sinars, S. A. Slutz, A. C. Owen, K. Tomlinson, M. R. Gomez, S. B. Hansen, M. C. Herrmann, M. C. Jones, J. L. McKenney, G. K. Robertson, G. A. Rochau, M. E. Savage, D. G. Schroen, and W. A. Stygar, Physics of Plasmas **21**, 056303 (2014).

[9] D. D. Ryutov and M. A. Dorf, Physics of Plasmas **21**, 112704 (2014).

[10] T. A. Shelkovenko, D. A. Chalenski, K. M. Chandler, J. D. Douglass, J. B. Greenly, D. A. Hammer, B. R. Kusse, R. D. McBride, and S. A. Pikuz, Review of Scientific Instruments **77**, 10F521 (2006).

[11] P.-A. Gourdain, R. Concepcion, M. Evans, J. Greenly, D. Hammer, C. Hoyt, E. Kroupp, B. Kusse, Y. Maron, A. Novick, S. Pikuz, N. Qi, G. Rondeau, E. Rosenberg, P. Schrafel, C. Seyler, and T. Shelkovenko, Nuclear Fusion **53**, 083006 (2013).

[12] G. C. Burdiak, S. V. Lebedev, R. P. Drake, A. J. Harvey-Thompson, G. F. Swadling, F. Suzuki-Vidal, J. Skidmore, L. Suttle, E. Khoory, L. Pickworth, P. de Grouchy, G. N. Hall, S. N. Bland, M. Weinwurm, and J. P. Chittenden, High Energy Density Physics **9**, 52 (2013).

[13] S. C. Bott-Suzuki, S. W. Cordaro, L. S. Caballero Bendixsen, I. C. Blesener, L. Atoyan, T. Byvank, W. Potter, K. S. Bell, B. R. Kusse, J. B. Greenly, and D. a. Hammer, Physics of Plasmas **22**, 094501 (2015).

APPENDIX B

TECHNIQUE FOR INSULATED AND NON-INSULATED METAL LINER X-PINCH RADIOGRAPHY ON A 1 MA PULSED POWER MACHINE

Technique for insulated and non-insulated metal liner X-pinch radiography on a 1 MA pulsed power machine

L. Atoyan, T. A. Shelkovenko, S. A. Pikuz, D. A. Hammer, T. Byvank, J. B. Greenly, and W. M. Potter

Citation: Review of Scientific Instruments **88**, 113502 (2017);
View online: https://doi.org/10.1063/1.4989985
View Table of Contents: http://aip.scitation.org/toc/rsi/88/11
Published by the American Institute of Physics

Technique for insulated and non-insulated metal liner X-pinch radiography on a 1 MA pulsed power machine

L. Atoyan, T. A. Shelkovenko,[a)] S. A. Pikuz,[a)] D. A. Hammer, T. Byvank, J. B. Greenly, and W. M. Potter
Laboratory of Plasma Studies, Cornell University, Rhodes Hall, Ithaca, New York 14853, USA

(Received 13 June 2017; accepted 18 October 2017; published online 1 November 2017)

Broadband, high resolution X-pinch radiography has been demonstrated as a method to view the instability induced small scale structure that develops in near solid density regions of both insulated and non-insulated cylindrical metallic liners. In experiments carried out on a 1-1.2 MA 100-200 ns rise time pulsed power generator, μm scale features were imaged in initially 16 μm thick Al foil cylindrical liners. Better resolution and contrast were obtained using an X-ray sensitive film than with image plate detectors because of the properties of the X-pinch X-ray source. We also discuss configuration variations that were made to the simple cylindrical liner geometry that appeared to maintain validity of the small-scale structure measurements while improving measurement quality. *Published by AIP Publishing.* https://doi.org/10.1063/1.4989985

I. INTRODUCTION

Radiography is a common diagnostic in a wide array of applications such as medical imaging, product inspection for material integrity, and airport security. In the field of plasma physics, it is very useful for probing high density regions of a plasma. For example, it was used in the Magnetized Liner Inertial Fusion (MagLIF) experiments to show the existence of a helical structure in the liner when an axial magnetic field was applied.[1] In those experiments, monochromatic X-rays were produced using a laser source. Another source of X-rays that can be used for dense plasma radiography in the $\lesssim$5 keV range is the X-pinch,[2,3] a very small and broadband source that can lead to high resolution imaging. If the experiment uses a pulsed power machine designed to drive sufficiently high current, then a benefit is the ability to put an X-pinch in series or in parallel with the main experimental load so that a separate X-ray driver is not needed. This is especially useful when a high-power laser is not available to produce X-rays.

In the MagLIF experiments, features of the order of 10-100 μm were observed to develop[4,5] in the liner and were mitigated using thick dielectric coatings.[6] In this paper, we describe a means to use radiography to study the development of such a structure. We present the first demonstration of using X-pinch radiography in cylindrical liner experiments with and without dielectric coatings where the high-density regions of both the liner and insulator were directly observed. We make use of a method that allows looking through only one layer of the liner, as opposed to the default of two layers, by employing a slit that we will show does not significantly affect the radiography results at the time of measurement. We also compare images from two types of detectors, the image plate and film, showing the difference in results from similar experiments. Finally, we discuss extra diagnostic protection needed in experiments with solid dielectrics due to the presence of destructive debris.

II. EXPERIMENTAL ARRANGEMENT AND DIAGNOSTICS

A. Liner and X-pinch setup

A sample experimental configuration is shown in Fig. 1. There is a 4.2 mm diameter, 11 mm long, and 16 μm thick cylindrical Al foil liner located in the center of Fig. 1(a), serving as the load of the 1-1.2 MA 100-200 ns rise time Cornell Beam Research Accelerator (COBRA).[7] It delivers ~5 kJ of energy to the liner in a 200 ns pulse. It is made by taking flat Al foil, wrapping it once around a rod, positioning it between anode and cathode holders, letting the foil's elasticity expand it against the inner wall of the holders [e.g., the hole in the brass anode in Fig. 1(b)] and finally removing the rod. Similar wrapping methods have been used in previous experiments, one group using foils as thin as 400 nm.[8] Such methods allow using sufficiently thin liners to enable radiography through the solid regions of the liner. A schematic diagram of what the X-ray radiography detector sees in such foil setups is shown in Fig. 1(c). Using the Center for X-ray Optics' (CXRO) free online database, we show in Fig. 2 that there is very little transmission through 50 μm Al, but there is significant transmission for 10 μm Al over a portion of the $\approx$1–4 keV X-ray emission region of a Mo wire X-pinch.[3] As foils generally enable liner thicknesses and tolerances that are much smaller than those that are practical to machine, they are an attractive means to make liner loads for 1 MA pulsed power generators.

A clear disadvantage of using foils in the manner described above is the lack of symmetry that will induce near the overlap region in the wrapped foil. Complete azimuthal symmetry must be not of vital importance to the experiment if this configuration is to be valid. Furthermore, if symmetry is not critical, a narrow axial slit can be made, as shown in

[a)]Permanent address: P.N. Lebedev Physical Institute, Moscow, Russia.

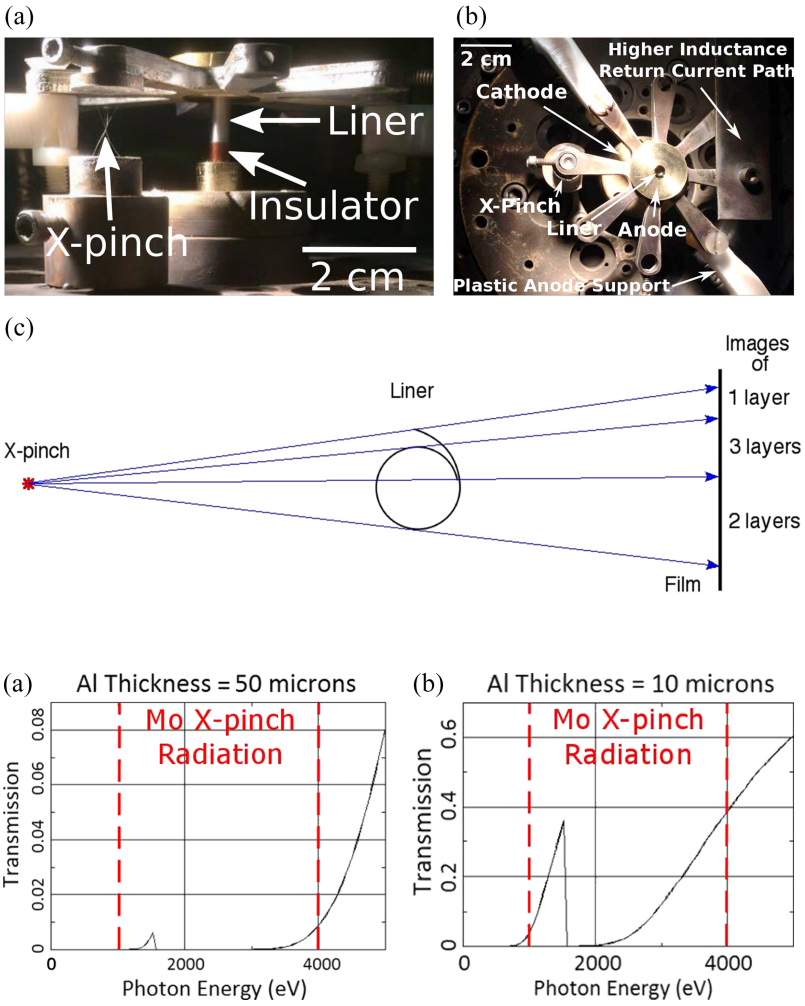

FIG. 1. (a) Side view and (b) the top view of a half-insulated Al liner setup. The 11 mm long, 16 μm thick liner in the center is surrounded by a 4 mm long 50 μm thick solid insulator. There is a 4-wire 25 μm Mo X-pinch positioned in place of one of the return current posts. The second return current post is positioned radially farther out than the X-pinch in order to increase its relative current path inductance. The anode is held in place by the white plastic supports. (c) Top view schematic representation of a liner showing X-ray paths through different layers of foil. The diagram is not to scale.

FIG. 2. X-ray transmission percentage through solid Al as a function of photon energy, data obtained from CXRO's online X-ray database. The increased transmission with decreased Al thickness from (a) 50 μm to (b) 10 μm is evident. The X-ray emission range of Mo-wire X-pinches is highlighted.

Fig. 3(a), for radiography purposes. The approximation then is that the resulting physical and magnetic field perturbations from side B in Fig. 3(b) that do not affect the development of the observed structure on side A at the time of the radiograph. The advantage of this compromise is that one can now use thicker foils for the liner and still obtain high-resolution radiography of side A as the X-rays are transmitted through only one layer. Comparing data with and without slits, we find similar small scale structure sizes for both, between 17 and 25 μm, meaning that the approximation concerning the impact of the slit evidently holds for our radiography measurements.

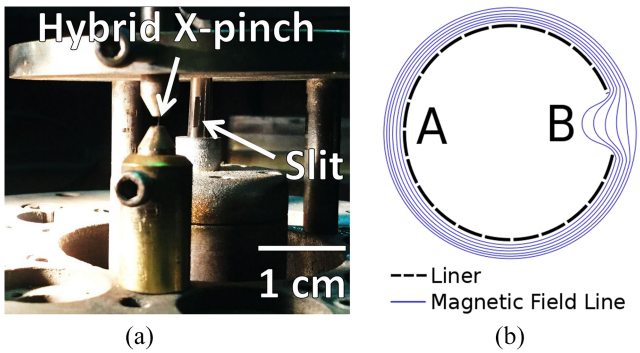

FIG. 3. (a) Photograph showing the liner with a slit cut in it and a hybrid X-pinch on the return current post. (b) Cross-sectional view of the liner illustrating the magnetic field line bending.

A comprehensive review of X-pinches as X-ray sources for radiography has been given by Pikuz *et al.*[2,3] and Shelkovenko *et al.*[9] The hybrid X-pinches that were used, shown in Fig. 3(a), consisted of two conical stainless steel electrodes with a 2 mm long wire connecting them. Both these hybrid X-pinches and the 4-wire X-pinches, shown in Fig. 1, are discussed in detail in the review articles earlier. They were both used successfully in experiments described here when positioned in return current posts on the COBRA. For Al liners, the filter we used in front of the detector was 12.5 μm thick Ti foil as the latter has a transmission-vs-wavelength curve that matches well with our Al foil absorption characteristics in the ≈2.8–4.8 keV range and the radiation spectrum produced by a 1 μm source size Mo wire X-pinches. If a different liner material is used, such as Cu, different filters must be used to better match the transmission wavelength range of the foil. Also note that one can change the source spectrum if needed by changing the X-pinch wire material.[2,3]

An important aspect of the radiography method described here is the combination of the Mo X-pinch with the specific filters. The X-pinch produces a small, 1-2 μm, source size for a

limited energy range only. Anything below or above that range has a larger source size, reaching 10–100 μm. If we look at a 12.5 μm Ti filter, for example, the transmission below 6 keV is substantial in the ≈2.8–4.8 keV window. This also happens to be the spectral region where the Mo X-pinch source size is near 1 μm.

In our experiments, we have used 1, 2, and 3 X-pinches in parallel in the COBRA return current circuit using Mo wires that were 17-40 μm in diameter, depending on the experiment. The magnification factor, determined by the relative distances between the detector, liner, and X-ray source for point-projection radiography, was 12-13 and was limited by the size of the experimental vacuum chamber rather than by X-pinch intensity or detector sensitivity.

B. Insulator considerations

One possibility for an insulating coating on a metal liner is a liquid dielectric which will flow over the whole liner, effectively covering the entire surface. This can be useful when used in conjunction with solid dielectrics placed outside the liquid as a solid insulator may provide better expansion inhibition compared to a liquid one, with the combination also providing good contact between the liner and solid insulator. Solid dielectrics alone should not be expected to fully contact the liner if one relies only on the liner's elasticity to expand against the insulator using the method described in Sec. II A. We have experimented with both liquid + solid and solid only insulators. However, the focus of this paper, when discussing insulated liners, will be on solid only insulators. We used 50 and 75 μm thick Kapton tubes, obtained from Precision Products Group, and 100 μm thick Mylar tubes, obtained from Euclid Spiral Paper Tube Corp.

Another method to reduce the problem of gaps between the liner and insulator is by "sandwiching" the liner between two layers of solid insulators, as shown in Fig. 4. To do this, we can take two flexible insulators whose gap between the outer surface of the inner insulator and the inner surface of the outer insulator is less than the thickness of the liner. As the insulators are plastic, they have some flexibility to stretch/compress to allow room for the foil. This sandwiching technique along with using thin liners is a simple, inexpensive method that enables radiography through the liner in experiments in which we inhibit the expansion of the metal. Note that this method is effective to reduce gaps down to the μm scale. Foils may have inherent structure below that scale that create gaps, such as ripples, that sandwiching would not eliminate.

Furthermore, we radiographed insulated liners using an insulator that only partially covered the liner axially. We could then simultaneously radiograph insulated and non-insulated portions of the Al liner to make a direct comparison on the same shot, while also observing the processes taking place at the boundary between the two regions.

III. RESULTS AND ANALYSIS

Choosing the right detector was critical to being able to observe the small scale features of interest here. We tried using both Carestream's DR50 film, which is advertised by the company as "an ultra-fine grain, very high contrast film," and Fujifilm's BAS-SR 2040 image plates, which are detectors commonly used in the medical field. The scanner used for the image plates was the Typhoon FLA 7000, scanning at 25 μm pixel size, a 650 nm wavelength and a photomultiplier tube (PMT) voltage setting of 500. The time between an experiment and scanning the image plate was no more than 10 min and exposure of the image plate to light in that period was practically nil. A result is shown in Fig. 5 for a 16 μm Al liner with a slit cut into it, as shown in Fig. 3(a). The experiment had an image plate positioned immediately behind the film. We can see a region where the X-rays are absorbed by a single layer (lighter) and regions where they are absorbed by two layers (darker) in both detectors. The image plate shows the small-scale structure through a single layer but, in spite of substantial software contrast enhancement to show the structure, not through two. On the other hand, the DR50 film clearly shows features in both regions. Similar behavior was observed with the image plate in numerous experiments, both behind the film or without any film in front of it. Placing no film in

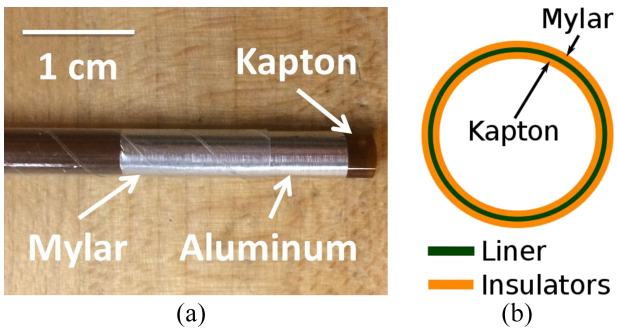

FIG. 4. (a) A photo of a liner "sandwiched" between two insulators. Here, the Kapton acts as the inner insulator and the Mylar as the outer insulator. In the picture, the Al foil has been axially extended from underneath the Mylar, and the Kapton from underneath the Al, to clearly show all three layers. (b) An axial cross-sectional schematic of the setup.

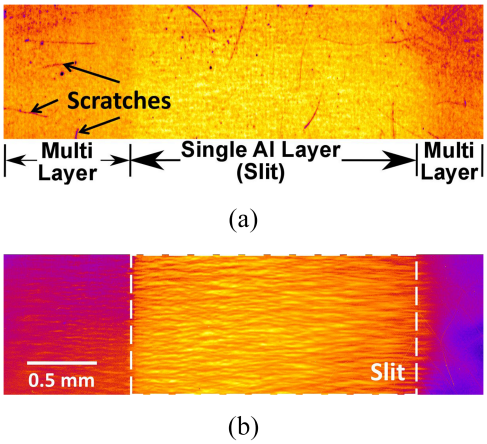

FIG. 5. X-pinch radiographs of an Al liner with a slit cut into it, as described in Sec. II A, on (a) an image plate and (b) a DR50 film. The radiographs were taken at 105 ns in a 140 ns rise time 1.1 MA peak current pulse. At that time, the current was 0.85 MA. The white dashed lines in (b) are delimiting the area of the slit.

TABLE I. Detector comparison-feature detection.

Material	Film-visible features	Image plate-visible features
Al (1 layer)	Yes	Yes
Al (2 layers)	Yes	No
Cu, Ni, Ti	Yes at 50% occurrence	No

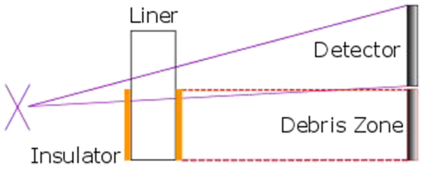

FIG. 7. Sketch depicting a method that prevents damage caused to the radiography detector from the liner debris.

front is important as the film otherwise absorbs a significant amount of 3–4 keV X-ray radiation that is responsible for the high resolution achieved with the X-pinch. For Cu, Ni, and Ti liners, out of 16 experiments, none showed any visible features using image plates with no film in front of them. Out of a similar number of experiments using the film, roughly half the experiments displayed features. Cu, Ni, and Ti tended to have smaller feature sizes and/or smaller contrast compared to Al, which we believe accounts for the reduced fraction of experiments with visible features.

Comparing detectors, these results show that using a film produces results with better resolution and contrast than using SR image plates. A summary of this comparison is shown in Table I. The smallest features observed on the film were roughly 5 μm at the object. Hence, we estimate the resolution from using a film with the magnification of 12-13 to be around 5 μm. We believe that the better results with the film in our experiments are due to the image plates being more sensitive to harder X-rays than the film. That matters because the source size of the X-pinch, as previously mentioned, increases for X-rays > 5 keV to 10-100 μm. As the features of interest are 10-25 μm in size, the larger source size will cause a blurring of the structure on the image plates.

There is an important benefit of using the image plate positioned behind the film. In combination with signals from photoconducting diodes monitoring the soft X-ray intensity, the image plate exposure gives a good indication of the intensity of the X-pinch(es) on a particular shot, thereby providing guidance on how long to develop the film in order not to cause overexposure or underexposure. In our experiments, we have changed development time by up to 50% based upon this cueing.

For experiments with insulators, we found it necessary to protect the detectors and other diagnostics in the experiment from debris. Figure 6(a) shows the typical damage from debris incurred by a protective window placed approximately 45 cm away from the load region. In one experiment out of about ten, the window shattered. To learn the state of matter of the debris, we used foam to catch it. Note that foam is critical here as a harder surface, e.g., glass, can cause a high-velocity solid to vaporize upon impact, not to mention shattering the glass. We caught solid black thin filaments, as shown in Figs. 6(b) and 6(c). Hence, at least a portion of the debris appears to be bits of a solid insulator. Evidently not all of the insulator vaporized. Instead, it was turned into a solid projectile by the foil explosion pressures propelling the insulator radially outward. Note that we estimate delivering about three orders of magnitude more energy to the load than would be needed to vaporize the insulator. While only a small fraction of the energy at the load will go into heating the insulator, the presence of the solid insulator might not be expected from this energy estimate comparison.

To protect the X-ray sensitive detectors from the debris, we found that using a 250 μm thick Mylar protector was not sufficient. The debris pierced straight through the protector and the Ti filter and lodged itself in the DR50 film. Finding that the debris moves nearly perpendicular to the axis, detector integrity in future experiments can be assured with reasonable confidence by angling the line-of-sight, as shown in Fig. 7.

Figure 8 shows results from an experiment with two outer solid insulator layers only partially covering the liner axially. We can clearly see the two layers of the insulator and their edges. There are vacuum gaps visible between insulators and between the insulator and liner. This shows that the liner's expansion is not inhibited by the insulator until ≈200–300 μm expansion occurs in this setup. However, the gap(s) can be filled by a liquid dielectric to inhibit expansion. Note that the blurry features at the edges of the insulator are a result of multiple bursts of the X-pinch in this experiment. The dark spot covering a large portion of the image is a consequence of the debris tearing through the Mylar and Ti filter, as explained

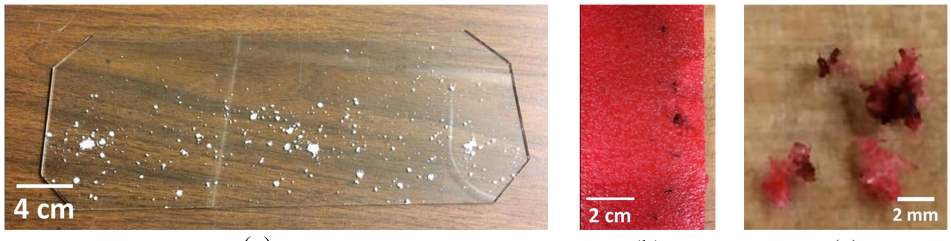

(a) (b) (c)

FIG. 6. (a) A post-experiment picture of a protective window placed roughly 45 cm away from an insulated liner. (b) A piece of foam that was used to capture the debris to prevent the latter's vaporization upon impact. (c) A zoomed in picture of the debris extracted from a few locations in the foam catcher shown in (b)—curled solid black thin filaments enveloped by the red foam.

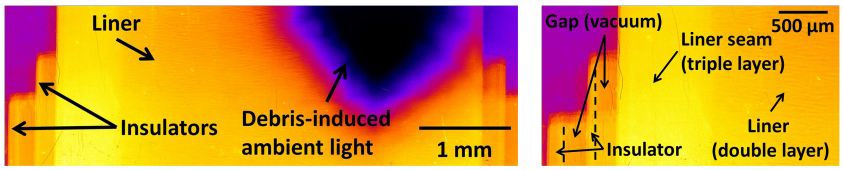

(a) (b)

FIG. 8. (a) Radiograph of an Al liner with 2 layers of the solid insulator surrounding it. The insulators are only partly covering the liner axially. (b) A zoomed-in view of the insulators. In the case shown, the vacuum gaps between solid insulators and between the inner insulator and the liner, which can easily be filled with a liquid dielectric, if desired, are pointed out. The blurry edges are due to two X-pinch soft X-ray bursts, one at 70 ns the other at 80 ns in a 110 ns rise time pulse, that create multiple images overlaying one another.

above, and exposing a portion of the film to the ambient light.

We have presented a method to effectively radiograph thin metallic liners with and without expansion inhibition using the X-pinch as the X-ray source. X-pinch radiation enables radiography through both insulated and non-insulated liners and may be very useful for better understanding the physics involved in the early stages of liner experiments. Experiments using this method are continuing in order to investigate the development of small scale features in metal liners thought to be caused by the electrothermal[4,5] and electrochoric[10] instabilities.

ACKNOWLEDGMENTS

This work was supported by the National Nuclear Security Administration Stewardship Sciences Academic Programs under Department of Energy Cooperative Agreement No. DE-NA0001836 as well as by the Department of Energy Grant No. DE-NA0002952. The authors would like to thank Harry Wilhelm, Todd Blanchard, and Daniel Hawkes for their excellent technical support.

[1]T. J. Awe, C. A. Jennings, R. D. McBride, M. E. Cuneo, D. C. Lamppa, M. R. Martin, D. C. Rovang, D. B. Sinars, S. A. Slutz, A. C. Owen, K. Tomlinson, M. R. Gomez, S. B. Hansen, M. C. Herrmann, M. C. Jones, J. L. McKenney, G. K. Robertson, G. A. Rochau, M. E. Savage, D. G. Schroen, and W. A. Stygar, Phys. Plasmas **21**, 056303 (2014).
[2]S. A. Pikuz, T. A. Shelkovenko, and D. A. Hammer, Plasma Phys. Rep. **41**, 291 (2015).
[3]S. A. Pikuz, T. A. Shelkovenko, and D. A. Hammer, Plasma Phys. Rep. **41**, 445 (2015).
[4]K. J. Peterson, D. B. Sinars, E. P. Yu, M. C. Herrmann, M. E. Cuneo, S. A. Slutz, I. C. Smith, B. W. Atherton, M. D. Knudson, and C. Nakhleh, Phys. Plasmas **19**, 092701 (2012).
[5]K. J. Peterson, E. P. Yu, D. B. Sinars, M. E. Cuneo, S. A. Slutz, J. M. Koning, M. M. Marinak, C. Nakhleh, and M. C. Herrmann, Phys. Plasmas **20**, 056305 (2013).
[6]T. J. Awe, K. J. Peterson, E. P. Yu, R. D. Mcbride, D. B. Sinars, M. R. Gomez, C. A. Jennings, M. R. Martin, S. E. Rosenthal, D. G. Schroen, A. B. Sefkow, S. A. Slutz, K. Tomlinson, and R. A. Vesey, Phys. Rev. Lett. **116**, 065001 (2016).
[7]J. B. Greenly, D. A. Hammer, B. R. Kusse, J. T. Blanchard, L. M. Maxson, R. D. Mcbride, H. Wilhelm, S. C. Glidden, S. Grasso, and H. D. Sanders, in *IEEE Pulsed Power Conference* (IEEE, 2005), pp. 273–276.
[8]D. A. Yager-Elorriaga, A. M. Steiner, S. G. Patel, N. M. Jordan, Y. Y. Lau, and R. M. Gilgenbach, Rev. Sci. Instrum. **86**, 113506 (2015).
[9]T. A. Shelkovenko, S. A. Pikuz, and D. A. Hammer, Plasma Phys. Rep. **42**, 226 (2016).
[10]J. D. Pecover and J. P. Chittenden, Phys. Plasmas **22**, 102701 (2015).

BIBLIOGRAPHY

[1] S. a. Slutz, M. C. Herrmann, R. a. Vesey, a. B. Sefkow, D. B. Sinars, D. C. Rovang, K. J. Peterson, and M. E. Cuneo. Pulsed-power-driven cylindrical liner implosions of laser preheated fuel magnetized with an axial field. *Physics of Plasmas*, 17(5):056303, 2010.

[2] S. A. Slutz, W. A. Stygar, M. R. Gomez, K. J. Peterson, A. B. Sefkow, D. B. Sinars, R. A. Vesey, E. M. Campbell, and R. Betti. Scaling magnetized liner inertial fusion on Z and future pulsed-power accelerators. *Physics of Plasmas*, 23(2):022702, 2016.

[3] E. Husain and R. S Nema. Analysis of Paschen Curves for air, N2 and SF6 Using the Townsend Breakdown Equation. *IEEE Transactions on Electrical Insulation*, EI-17(4):350–353, 1982.

[4] A D Cahill. *an Investigation of the Aluminum K-Edge By Spatially Resolved X-Ray Absorption Spectroscopy*. PhD thesis, 2016.

[5] Tatiana Shelkovenko, Sergey Pikuz, and David Hammer. X-Pinches as Broadband Sources of X-Rays for Radiography. *Journal of Biomedical Science and Engineering*, 08(11):747–755, 2015.

[6] J. D. Pecover and J. P. Chittenden. Instability growth for magnetized liner inertial fusion seeded by electro-thermal, electro-choric, and material strength effects. *Physics of Plasmas*, 22(10), 2015.

[7] Amasa S. Bishop. *Project Sherwood: The U.S. Program in Controlled Fusion*. Addison-Wesley Publishing Company, 1958.

[8] D D Ryutov. The physics of fast Z pinches. 72(1), 2000.

[9] M G Haines. A review of the dense Z -pinch. *Plasma Physics and Controlled Fusion*, 53(9):093001, sep 2011.

[10] Hansjoachim Bluhm and Pulsed Power Systems. *Pulsed Power Systems*. Power Systems. Springer-Verlag, Berlin/Heidelberg, 2006.

[11] J B Greenly, D A Hammer, B R Kusse, J T Blanchard, L M Maxson, R D Mcbride, H Wilhelm, S C Glidden, S Grasso, and H D Sanders. CAPABILITIES OF THE RECONFIGURED COBRA ACCELERATOR *. In *IEEE Pulsed Power Conference*, pages 273–276. IEEE, 2005.

[12] Michael Mazarakis, William Fowler, Alexander Kim, Vadim Sinebryukhov, Sonrisa Rogowski, Robin Sharpe, Dillon McDaniel, Craig Olson, John Porter, Kenneth Struve, William Stygar, and Joseph Woodworth. High current, 0.5-MA, fast, 100-ns, linear transformer driver experiments. *Physical Review Special Topics - Accelerators and Beams*, 12(5):050401, may 2009.

[13] W. a. Stygar, W. E. Fowler, K. R. LeChien, F. W. Long, M. G. Mazarakis, G. R. McKee, J. L. McKenney, J. L. Porter, M. E. Savage, B. S. Stoltzfus, D. M. Van De Valde, and J. R. Woodworth. Shaping the output pulse of a linear-transformer-driver module. *Physical Review Special Topics - Accelerators and Beams*, 12(3):030402, mar 2009.

[14] M. K. Matzen, B. W. Atherton, M. E. Cuneo, G. L. Donovan, C. a. Hall, M. Herrmann, M. L. Kiefer, R. J. Leeper, G. T. Leifeste, F. W. Long, G. R. Mckee, T. a. Mehlhorn, J. L. Porter, L. X. Schneider, K. W. Struve, W. a. Stygar, and E. a. Weinbrecht. The refurbished z facility: Capabilities and recent experiments. *Acta Physica Polonica A*, 115(6):956–958, 2009.

[15] M R Gomez, S A Slutz, A B Sefkow, D B Sinars, K D Hahn, S B Hansen, E C Harding, P F Knapp, M C Herrmann, M H Hess, O Johns, D C Lamppa, M R Martin, and R D Mcbride. Experimental Demonstration of Fusion-Relevant Conditions in Magnetized Liner Inertial Fusion. 155003(October):1–5, 2014.

[16] R. D. McBride, M. R. Martin, R. W. Lemke, J. B. Greenly, C. A. Jennings, D. C. Rovang, D. B. Sinars, M. E. Cuneo, M. C. Herrmann, S. A. Slutz, C. W. Nakhleh, D. D. Ryutov, J. P. Davis, D. G. Flicker, B. E. Blue, K. Tomlinson, D. Schroen, R. M. Stamm, G. E. Smith, J. K. Moore, T. J. Rogers, G. K. Robertson, R. J. Kamm, I. C. Smith, M. Savage, W. A. Stygar, G. A. Rochau, M. Jones, M. R. Lopez, J. L. Porter, and M. K. Matzen. Beryllium liner implosion experiments on the Z accelerator in preparation for magnetized liner inertial fusion. *Physics of Plasmas*, 20(5), 2013.

[17] J. C. Valenzuela, G. W. Collins IV, D. Mariscal, E. S. Wyndham, and F. N. Beg. Study of instability formation and EUV emission in thin liners driven with a compact 250 kA, 150 ns linear transformer driver. *Physics of Plasmas*, 21(3), 2014.

[18] D. A. Yager-Elorriaga, P. Zhang, A. M. Steiner, N. M. Jordan, P. C. Campbell, Y. Y. Lau, and R. M. Gilgenbach. Discrete helical modes in imploding and exploding cylindrical, magnetized liners. *Physics of Plasmas*, 23(12):124502, 2016.

[19] D. D. Ryutov, M. E. Cuneo, M. C. Herrmann, D. B. Sinars, and S. a. Slutz. Simulating the magnetized liner inertial fusion plasma confinement with smaller-scale experiments. *Physics of Plasmas*, 19(6):062706, jun 2012.

[20] S. a. Chaikovsky, V. I. Oreshkin, I. M. Datsko, N. a. Labetskaya, and N. a. Ratakhin. Skin explosion of double-layer conductors in fast-rising high magnetic fields. *Physics of Plasmas*, 21(4), 2014.

[21] G. C. Burdiak, S. V. Lebedev, F. Suzuki-Vidal, G. F. Swadling, S. N. Bland, N. Niasse, L. Suttle, M. Bennet, J. Hare, M. Weinwurm, R. Rodriguez, J. Gil, and G. Espinosa. Cylindrical liner Z-pinch experiments for fusion research and high-energy-density physics. *Journal of Plasma Physics*, 81:1–20, 2015.

[22] Irvin R. Lindemuth. The ignition design space of magnetized target fusion. *Physics of Plasmas*, 22(12):122712, 2015.

[23] E. G. Harris. Rayleigh-Taylor Instabilities of a Collapsing Cylindrical Shell in a Magnetic Field. *Physics of Fluids*, 5(9):1057, 1962.

[24] Aaron R. Miles. Nonlinear RayleighTaylor instabilities in fast Z pinches. *Physics of Plasmas*, 16(3):032702, 2009.

[25] J C Zier, R M Gilgenbach, D A Chalenski, Y Y Lau, D M French, M. R. Gomez, S. G. Patel, I. M. Rittersdorf, A. M. Steiner, M. Weis, P. Zhang, M. Mazarakis, M. E. Cuneo, and M. Lopez. Magneto-Rayleigh-Taylor experiments on a MegaAmpere linear transformer driver. *Physics of Plasmas*, 19(3):032701, mar 2012.

[26] M. R. Weis, P. Zhang, Y. Y. Lau, P. F. Schmit, K. J. Peterson, M. Hess, and R. M. Gilgenbach. Coupling of sausage, kink, and magneto-Rayleigh-Taylor instabilities in a cylindrical liner. *Physics of Plasmas*, 22(3), 2015.

[27] D. B. Sinars, S. a. Slutz, M. C. Herrmann, R. D. McBride, M. E. Cuneo, K. J. Peterson, R. a. Vesey, C. Nakhleh, B. E. Blue, K. Killebrew, D. Schroen, K. Tomlinson, a. D. Edens, M. R. Lopez, I. C. Smith, J. Shores, V. Bigman, G. R. Bennett, B. W. Atherton, M. Savage, W. a. Stygar, G. T. Leifeste, and J. L. Porter. Measurements of Magneto-Rayleigh-Taylor Instability Growth during the Implosion of Initially Solid Al Tubes Driven by the 20-MA, 100-ns Z Facility. *Physical Review Letters*, 105(18):185001, oct 2010.

[28] Ryan D. McBride and Stephen A. Slutz. A semi-analytic model of magnetized liner inertial fusion. *Physics of Plasmas*, 22(5):052708, 2015.

[29] S. A. Slutz, C. A. Jennings, T. J. Awe, G. A. Shipley, B. T. Hutsel, and D. C. Lamppa. Auto-magnetizing liners for magnetized inertial fusion. *Physics of Plasmas*, 24(1):012704, 2017.

[30] P. F. Schmit, A. L. Velikovich, R. D. McBride, and G. K. Robertson. Controlling rayleigh-taylor instabilities in magnetically driven solid metal shells by means of a dynamic screw pinch. *Physical Review Letters*, 117(20):1–6, 2016.

[31] A. J. Harvey-Thompson, A. B. Sefkow, T. N. Nagayama, M. S. Wei, E. M. Campbell, G. Fiksel, P.-Y. Chang, J. R. Davies, D. H. Barnak, V. Y. Glebov, P. Fitzsimmons, J. Fooks, and B. E. Blue. Diagnosing laser-preheated magnetized plasmas relevant to magnetized liner inertial fusion. *Physics of Plasmas*, 22(12):122708, 2015.

[32] S. B. Hansen, M. R. Gomez, A. B. Sefkow, S. A. Slutz, D. B. Sinars, K. D. Hahn, E. C. Harding, P. F. Knapp, P. F. Schmit, T. J. Awe, R. D. McBride, C. A. Jennings, M. Geissel, A. J. Harvey-Thompson, K. J. Peterson, D. C. Rovang, G. A. Chandler, G. W. Cooper, M. E. Cuneo, M. C. Herrmann, M. H. Hess, O. Johns, D. C. Lamppa, M. R. Martin, J. L. Porter, G. K. Robertson, G. A. Rochau, C. L. Ruiz, M. E. Savage, I. C. Smith, W. A. Stygar, R. A. Vesey, B. E. Blue, D. Ryutov, D. G. Schroen, and K. Tomlinson. Diagnosing magnetized liner inertial fusion experiments on Z. *Physics of Plasmas*, 22(5), 2015.

[33] Kyle J. Peterson, Daniel B. Sinars, Edmund P. Yu, Mark C. Herrmann, Michael E. Cuneo, Stephen a. Slutz, Ian C. Smith, Briggs W. Atherton, Marcus D. Knudson, and Charles Nakhleh. Electrothermal instability growth in magnetically driven pulsed power liners. *Physics of Plasmas*, 19(9):092701, 2012.

[34] Kyle J. Peterson, Edmund P. Yu, Daniel B. Sinars, Michael E. Cuneo, Stephen a. Slutz, Joseph M. Koning, Michael M. Marinak, Charles Nakhleh, and Mark C. Herrmann. Simulations of electrothermal instability growth in solid aluminum rods. *Physics of Plasmas*, 20(5), 2013.

[35] R. D. McBride, S. a. Slutz, C. a. Jennings, D. B. Sinars, M. E. Cuneo, M. C. Herrmann, R. W. Lemke, M. R. Martin, R. a. Vesey, K. J. Peterson, a. B. Sefkow, C. Nakhleh, B. E. Blue, K. Killebrew, D. Schroen, T. J. Rogers, a. Laspe, M. R. Lopez, I. C. Smith, B. W. Atherton, M. Savage, W. a. Stygar, and J. L. Porter. Penetrating radiography of imploding and stagnating beryllium liners on the Z accelerator. *Physical Review Letters*, 109(September):1–5, 2012.

[36] T. J. Awe, C. a. Jennings, R. D. McBride, M. E. Cuneo, D. C. Lamppa, M. R. Martin, D. C. Rovang, D. B. Sinars, S. a. Slutz, a. C. Owen, K. Tomlinson, M. R. Gomez, S. B. Hansen, M. C. Herrmann, M. C. Jones, J. L. McKenney, G. K. Robertson, G. a. Rochau, M. E. Savage, D. G. Schroen, and W. a. Stygar. Modified helix-like instability structure on imploding z-pinch liners that are pre-imposed with a uniform axial magnetic fielda). *Physics of Plasmas*, 21(5):056303, may 2014.

[37] Ian H. Hutchinson. *Principles of Plasma Diagnostics*. Cambridge University Press, 2002.

[38] Paul M. Bellan. *Fundamentals of Plasma Physics*. Cambridge University Press, 2006.

[39] D. D. Ryutov. Liner-on-plasma system near stagnation: Stabilizing effect of a magnetic cushion. *Physics of Plasmas*, 18(6):064509, 2011.

[40] Kate Suzanne Blesener. Spectroscopic Determinations of Magnetic Fields , Electron Temperatures , and Electron Densities in Single Wire Aluminum Plasmas. (August):152, 2012.

[41] S. a. Pikuz, T. a. Shelkovenko, and D. a. Hammer. X-pinch. Part I. *Plasma Physics Reports*, 41(4):291–342, 2015.

[42] S. a. Pikuz, T. a. Shelkovenko, and D. a. Hammer. X-pinch. Part II. *Plasma Physics Reports*, 41(6):445–491, 2015.

[43] T A Shelkovenko, S A Pikuz, C L Hoyt, A D Cahill, L Atoyan, D A Hammer, I N Tilikin, A R Mingaleev, V M Romanova, A V Agafonov, T A Shelkovenko, S A Pikuz, C L Hoyt, A D Cahill, L Atoyan, and D A Hammer. A source of hard X-ray radiation based on hybrid X pinches A source of hard X-ray radiation based on hybrid X pinches. *Physics of Plasmas*, 23(2016), 2016.

[44] Isaac Curtis Blesener. Initiation, Ablation, Precursor Formation, and Instability Analysis of Thin Foil Liner Z-pinches. (August), 2012.

[45] G. C. Burdiak, S. V. Lebedev, R. P. Drake, a. J. Harvey-Thompson, G. F. Swadling, F. Suzuki-Vidal, J. Skidmore, L. Suttle, E. Khoory, L. Pickworth, P. de Grouchy, G. N. Hall, S. N. Bland, M. Weinwurm, and J. P. Chittenden. The production and evolution of multiple converging radiative shock waves in gas-filled cylindrical liner z-pinch experiments. *High Energy Density Physics*, 9(1):52–62, 2013.

[46] G. C. Burdiak, S. V. Lebedev, a. J. Harvey-Thompson, G. F. Swadling, F. Suzuki-Vidal, G. N. Hall, E. Khoory, L. Pickworth, S. N. Bland, P. De Grouchy, J. Skidmore, L. Suttle, M. Bennett, N. P L Niasse, R. J R Williams, K. Blesener, L. Atoyan, a. Cahill, C. Hoyt, W. Potter, E. Rosenberg, P. Schrafel, and B. Kusse. Radiative precursors driven by converging blast waves in noble gases. *Physics of Plasmas*, 21, 2014.

[47] Juan J. Valencia and Peter N. Quested. Thermophysical Properties. *ASM Hadbook, Volume 15: Casting*, 15(1981):468–481, 2011.

[48] Iaea. Thermophysical Properties of Materials for Nuclear Engineering: A Tutorial and Collection of Data. *Atomic Energy*, page 200, 2008.

[49] Gordon T. Dyos and Trevor Farrell. *Electrical resistivity handbook*. Peter Peregrinus Ltd., 1992.

[50] V. I. Oreshkin. Thermal instability during an electrical wire explosion. *Physics of Plasmas*, 15(9), 2008.

[51] T J Awe, E P Yu, K C Yates, W G Yelton, B S Bauer, T M Hutchinson, S Fuelling, and B B Mckenzie. On the Evolution From Micrometer-Scale Inhomogeneity to Global Overheated Structure During the Intense Joule Heating of a z-Pinch Rod. *IEEE Transactions on Plasma Science*, 45(4):584–589, apr 2017.

[52] a. G. Rousskikh, V. I. Oreshkin, S. a. Chaikovsky, N. a. Labetskaya, a. V. Shishlov, I. I. Beilis, and R. B. Baksht. Study of the strata formation during the explosion of a wire in vacuum. *Physics of Plasmas*, 15(10):102706, 2008.

[53] D. a. Yager-Elorriaga, a. M. Steiner, S. G. Patel, N. M. Jordan, Y. Y. Lau, and R. M. Gilgenbach. Technique for fabrication of ultrathin foils in cylindrical geometry for liner-plasma implosion experiments with sub-megaampere currents. *Review of Scientific Instruments*, 86(11):113506, 2015.

[54] Kyle J. Peterson, Thomas J. Awe, Edmund P. Yu, Daniel B. Sinars, Ella S. Field, Michael E. Cuneo, Mark C. Herrmann, Mark Savage, Diana Schroen, Kurt Tomlinson, and Charles Nakhleh. Electrothermal Instability Mitigation by Using Thick Dielectric Coatings on Magnetically Imploded Conductors. *Physical Review Letters*, 112(13):135002, apr 2014.

[55] T J Awe, K J Peterson, E P Yu, R D Mcbride, D B Sinars, M R Gomez, C A Jennings, M R Martin, S E Rosenthal, D G Schroen, A B Sefkow, S A Slutz,

K Tomlinson, and R A Vesey. Experimental Demonstration of the Stabilizing Effect of Dielectric Coatings on Magnetically Accelerated Imploding Metallic Liners. *Physical Review Letters*, 065001(February):1–5, 2016.

[56] R. B. Baksht, a. G. Rousskikh, a. S. Zhigalin, V. I. Oreshkin, and a. P. Artyomov. Stratification in Al and Cu foils exploded in vacuum. *Physics of Plasmas*, 22(10):103521, 2015.

[57] Xuan Zhao, Yang Yang, and Charles E. Seyler. A positivity-preserving semi-implicit discontinuous Galerkin scheme for solving extended magnetohydrodynamics equations. *Journal of Computational Physics*, 278:400–415, 2014.

[58] C. E. Seyler and M. R. Martin. Relaxation model for extended magnetohydrodynamics: Comparison to magnetohydrodynamics for dense Z-pinches. *Physics of Plasmas*, 18(1), 2011.

[59] L Atoyan, T A Shelkovenko, S A Pikuz, D A Hammer, T Byvank, J B Greenly, and W M Potter. Technique for insulated and non-insulated metal liner X-pinch radiography on a 1 MA pulsed power machine. *Review of Scientific Instruments*, 88(11):113502, nov 2017.

[60] V. Morel, A. Bultel, and B. G. Chéron. The critical temperature of aluminum. *International Journal of Thermophysics*, 30(6):1853–1863, 2009.

[61] Aaron J. Ward. *Investigation of Aluminum Equation of State Generation*. PhD thesis, 2011.

[62] M. P. Desjarlais, J. D. Kress, and L. A. Collins. Electrical conductivity for warm, dense aluminum plasmas and liquids. *Physical Review E - Statistical, Nonlinear, and Soft Matter Physics*, 66(2):2–5, 2002.

[63] Mike Desjarlais. QMD Simulations of Warm Dense Matter in support of High Energy Density Physics Experiments on the Z Machine Sandia ' s Z Machine is used for several HEDP experimental campaigns. Technical report, 2006.

[64] Heinz E. Knoepfel. *Magnetic fields : A comprehensive theoretical treatise for practical use*. John Wiley and Sons, Inc, 2000.

[65] T. Awe, R. McBride, C. Jennings, D. Lamppa, M. Martin, D. Rovang, S. Slutz, M. Cuneo, a. Owen, D. Sinars, K. Tomlinson, M. Gomez,

S. Hansen, M. Herrmann, J. McKenney, C. Nakhleh, G. Robertson, G. Rochau, M. Savage, D. Schroen, and W. Stygar. Observations of Modified Three-Dimensional Instability Structure for Imploding z-Pinch Liners that are Premagnetized with an Axial Field. *Physical Review Letters*, 111(23):235005, dec 2013.

[66] P.-a. Gourdain, R.J. Concepcion, M.T. Evans, J.B. Greenly, D.a. Hammer, C.L. Hoyt, E. Kroupp, B.R. Kusse, Y. Maron, a.S. Novick, S.a. Pikuz, N. Qi, G. Rondeau, E. Rosenberg, P.C. Schrafel, C.E. Seyler, and T.C. Shelkovenko. Initial magnetic field compression studies using gas-puff Z -pinches and thin liners on COBRA. *Nuclear Fusion*, 53(8):083006, aug 2013.

[67] S. C. Bott-Suzuki, S. W. Cordaro, L. S. Caballero Bendixsen, L. Atoyan, T. Byvank, W. Potter, B. R. Kusse, J. B. Greenly, and D. A. Hammer. Study of the time-resolved, 3-dimensional current density distribution in solid metallic liners at 1 MA. *Physics of Plasmas*, 23(9):092711, 2016.

[68] S. C. Bott-Suzuki, S. W. Cordaro, L. S. Caballero Bendixsen, I. C. Blesener, L. Atoyan, T. Byvank, W. Potter, K. S. Bell, B. R. Kusse, J. B. Greenly, and D. a. Hammer. Investigation of the effect of a power feed vacuum gap in solid liner experiments at 1 MA. *Physics of Plasmas*, 22(9):094501, 2015.

[69] D. A. Yager-Elorriaga, P. Zhang, A. M. Steiner, N. M. Jordan, Y. Y. Lau, and R. M. Gilgenbach. Seeded and unseeded helical modes in magnetized, non-imploding cylindrical liner-plasmas. *Physics of Plasmas*, 23(10):101205, 2016.

[70] B V Oliver and T C Genoni. The unstable spectrum of m = 0 perturbations to Bennett equilibria for a visco-resistive Hall-MHD plasma column. Technical report.

[71] V.I. Sotnikov, L. Wanex, B.S. Bauer, I Paraschiv, J.N. Leboeuf, P. Hellinger, P. Travnicek, and V. Fiala. Linear analysis and 3D hybrid simulation study of Z-pinch instabilities in the presence of non - ideal MHD effects. In *Digest of Technical Papers. PPC-2003. 14th IEEE International Pulsed Power Conference (IEEE Cat. No.03CH37472)*, volume 1, pages 66–69. IEEE, 2003.

[72] J. Loverich and U. Shumlak. Nonlinear full two-fluid study of m=0 sausage instabilities in an axisymmetric Z pinch. *Physics of Plasmas*, 13(8), 2006.

[73] Edward Liverts and Michael Mond. The Hall instability in accelerated plasma channels. *Physics of Plasmas*, 11(1):55–61, 2004.